



**Development of Laplace Approach and RC-Model for Spheroid in
Travelling Wave Electric Field**

Sakshin Bunthawin

**A Thesis Submitted in Fulfillment of the Requirements for the Degree of
Doctor of Philosophy in Physics
Prince of Songkla University
2008**

Copyright of Prince of Songkla University

Thesis Title Development of Laplace Approach and RC-Model for Spheroid
 in Travelling Wave Electric Field
Author Mr. Sakshin Bunthawin
Major Program Physics

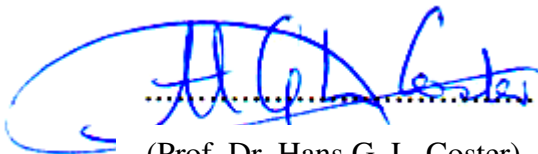
Major Advisor:

.....
(Assoc. Prof. Dr. Pikul Wanichapichart)


Examining Committee:

.....Chairperson
(Assoc. Prof. Dr. Tepakorn Pengpan)

Co-advisor:


.....
(Prof. Dr. Hans G. L. Coster)

.....
(Assoc. Prof. Dr. Pikul Wanichapichart)


.....
(Dr. Adisorn Tuantranont)

.....
(Assoc. Prof. Dr. Vittaya Amornkitbamrung)

.....
(Assist. Prof. Dr. Pruittikorn Smithmaitrie)

The Graduate School, Prince of Songkla University, has approved this thesis as partial fulfillment of the requirements for the Doctor of Philosophy Degree in Physics

.....
(Assoc. Prof. Dr. Kerkchai Thongnoo)
Dean of Graduate School

Thesis Title	Development of Laplace Approach and RC-Model for Spheroid in Travelling Wave Electric Field
Author	Mr.Sakshin Bunthawin
Major Program	Physics
Academic Year	2008

ABSTRACT

This thesis proposes theoretical approaches for forces acting on a spheroid in traveling wave electric field. The field was generated by an octa-pair interdigitated electrode array, made of gold depositing on a glass slide, and the fed signals were from a variable phase shift unit. Magnitude of the force was represented by means of velocity which is frequency dependent. Previous Laplace approach and RC-model have been extended and compared for a simpler method to reveal dielectric properties of a spheroid. Both methods showed force/velocity relationships, which were explained by real and imagination part of the Clausius-Mossotti Factor (CMF), to reveal dielectric values of cell membrane and its interior. Verifications of these theoretical approaches were made using yeast cells (*Saccharomyces cervisiata* TISTR 5088) and later phytoplankton, *Tetraselmis* sp. after pretreatment with several arsenic levels.

Velocity spectrum of a spheroid was obtained by measuring cell velocity during its moving towards the electrode tip, under various field frequencies. Lower critical frequency (f_λ), where the spheroid was repelled (i.e. negative force) from the tip after being attracted, was recorded against the conductivity of cell suspension medium (σ_s). It was observed that as the σ_s was increased the f_λ was shifted towards a higher frequency value. It should be noted that cell velocity spectra were reduced significantly under greater σ_s value. According to the new approaches, when the increased σ_s reached a critical value the attractive force became negligible, implying an equivalence to the cytoplasmic conductivity. Yeast cells of $1.15 \times 10^5 \text{ m}\lambda^{-1}$ displayed positive dielectrophoretic force over a frequency ranged between 50

kHz and 30 MHz, when increasing σ_s from 0.01 to 0.30 S.m⁻¹. The velocity spectrum was affected by σ_s of which the cells were suspending during the experimentation. An abrupt change in the velocity pattern explained non homogeneous phase, cell membrane and cytoplasm, only if the σ_s was small. Decreasing σ_s , there was a slightly shift of the prominent peak of the velocity spectrum towards a lower frequency value. By curve-fitting method, it was proved that dielectric values of yeast were similar to what were reported using other methods. The cytoplasmic and the membrane conductivity for yeast cells were 0.25 S.m⁻¹ and 0.1 μ S.m⁻¹, respectively.

When σ_s was less than 0.30 S.m⁻¹, *Tetraselmis* sp. experienced the positive dielectrophoretic force where the lower critical frequency (f_λ) remained unchanged at 50 kHz. However, when the σ_s reached 0.30 S.m⁻¹ and beyond until 0.10 S.m⁻¹, the f_λ was shifted from 200 to 500 kHz. Comparing cell density between 10⁵ and 10⁷ m λ ⁻¹, there was no difference in the velocity spectra, indicating that cell movement was solely affected by the external field during experimentation and the density was in an acceptable range for this verification. It should be noted that increasing the electric field strength only affected the force magnitude. In all experiments, the higher critical frequency (f_h) was not found. When the imaginary part of the CMF was plotted using the appropriate dielectric values estimated from the real part, the f_h was about 50 MHz. This explained why there was no evidence revealing the f_h from these approaches. Doubts were brought towards electrode spacing, creating a weak electric field. Cells were induced in the electric field strengths of 14 kV.m⁻¹, 28 kV.m⁻¹, 57 kV.m⁻¹ and 143 kV.m⁻¹, by increasing the applied voltage from the lower to the upper limit of the generator used for the present study i.e. 1, 2, 4 and 10 Vpp, respectively. Evidence confirming this explanation was that the cells were not repelled from the electrodes, resulting in no cells being collected in the middle of the electrode array. Hence, the imagination part developed in this study was remained for a future work. Under 28 kV.m⁻¹ field strength and σ_s of 0.01 S.m⁻¹, the velocity spectrum showed the prominent peak at 9.4 μ m.s⁻¹ (v_{cDEP}) under 200 kHz. Between 0.03 and 0.10 S.m⁻¹, the spectra were transformed to a bell

shape with the plateaus (i.e. a gradually changing in cell velocity) reduced from 5.2 to 3.5 $\mu\text{m.s}^{-1}$, respectively. The frequency dependences of these plateaus occupied the range between 500 kHz and 10 MHz. Under the low σ_s , increasing the field strengths from 28 to 143 kV.m^{-1} enhanced the velocity to as much as 29 $\mu\text{m.s}^{-1}$, and the maximum dielectrophoretic DEP force (DEP force) was estimated to be 6.09×10^{-14} N (or 6.09×10^{-2} pN). Increasing the σ_s stepwise from 0.03 to 0.06 and 0.10 S.m^{-1} , the magnitudes of v_{cDEP}^p spectra were decreased significantly from 0.65 to 0.58 and 0.44 $\mu\text{m.s}^{-1}$, respectively. At 28 kV.m^{-1} and 0.01 S.m^{-1} ; maximum value of v_{cDEP}^p was found to be 9.6 $\mu\text{m.s}^{-1}$ at 300 kHz which correspond with DEP force 1.93×10^{-14} N (or 1.93×10^{-2} pN). By curve fitting, the cytoplasm and the membrane conductivity for *Tetraselmis* sp. were 0.37 S.m^{-1} and 1.7 $\mu\text{S.m}^{-1}$, respectively. In addition, this study also showed that with the manufactured tool it was possible to distinguish viable from non-viable cells if these were mixed in the same solution.

On the effects of arsenic absorption, the DEP velocity (v_{cDEP}^p) spectra and the lower critical frequency of *Tetraselmis* sp. were investigated for a comparison, over the frequency range from 1 kHz to 30 MHz. It occurred that under 28-143 kV.m^{-1} field strengths the cells exhibited positive DEP only if the medium conductivity σ_s was ranged from 0.01 to 0.30 S.m^{-1} . Increasing arsenic level from 1 to 150 ppm reduced the magnitude of v_{cDEP}^p and shifts the f_λ to a lower value. When the control and the arsenic contaminated cells were combined in between the electrode array, one can distinguish the control from the arsenic pretreated cells if the conditions used were the same. However, the f_λ shift was small comparing with the 150 ppm contamination. Theoretically, lower f_λ indicates an increase in membrane permittivity. From our previous study, arsenic accumulated increased the cell membrane conductance without affecting cell growth, only if arsenic level was not greater than 100 ppm. With the increased arsenic level, the relative permittivity of the cell membrane was changed from 10 to 32. The electrical conductivity of the cytoplasm and the cell membrane was 0.03 S.m^{-1} and 3.0 $\mu\text{S.m}^{-1}$, respectively.

In conclusion, the specific capacitance (C_m) and conductance (G_m) of the membrane in all cases were calculated. The results showed that C_m and G_m of living and dead yeast cells were 11.06 mF.m⁻², 8.33 S.m⁻² and 18.44 mF.m⁻², 33.33×10³ S.m⁻², respectively. The values of C_m and G_m of the controlled *Tetraselmis* sp. were 5.45 mF.m⁻² and 13.08 S.m⁻², respectively, which were smaller than that of the arsenic pretreated cells. For 1, 5, 10, 50, and 150 ppm pretreated cells, C_m were 6.81, 8.17, 10.89, 14.30 and 21.79, respectively. It was interesting that while the C_m values of the arsenic pretreated cells were increased, the value of G_m remained constant and the conductivity of cell membrane (σ_m) was 23.08 S.m⁻².

CONTENTS

	Page
Contents	viii
List of Tables	xii
List of Figures	xiii
List of Symbols	xxii
Chapter	
1.Introduction	1
1.1 An Overview of the Present Study	1
1.2 The Conventional Dielectrophoresis (cDEP)	2
1.3 Techniques for Estimation of Cell Dielectric Properties via DEP	3
1.4 Ellipsoidal Shell Model	7
1.5 Traveling Wave Dielectrophoresis (twDEP)	8
1.6 Motivation and the Highlight of This Study	10
1.7 Aims of the present study	12
References	12
2.Theoretical Approaches for Determining Critical Frequencies for a Spheroidal Model	18
2.1 Introduction	18
2.2 The Critical frequencies: Laplace approach	19
2.2.1 The Geometry of the Spheroidal Model	19
2.2.2 An Effective Complex Relative Permittivity	24
2.2.3 Depolarization Factors	27
2.2.4 The Clausius-Mossotti Factor [CMF]	35
2.2.5 Two Critical Frequencies	48
2.3 An Impedance Approach (RC model)	52
2.3.1 The Clausius-Mossotti Factor [CMF]	52
2.3.2 Two Critical Frequencies	58
2.3.3 The Critical Conductivity	61
2.4 Discussions and Conclusions	61

CONTENTS (CONTINUED)

	Page
3. Theoretical Approach for Dielectrophoretic Velocity and Force Relation	68
3.1 Introduction	68
3.2 Co-Relation between the Conventional DEP and twDEP Forces	70
3.3 Dielectrophoretic Velocity	74
3.4 Discussions and Conclusions	77
References	78
4. Materials and Methods	80
4.1 Cell Preparations	80
4.1.1 Yeast Cells	80
4.1.2 <i>Tetraselmis</i> sp.	82
4.2 Electrode Fabrications	83
4.2.1 Preliminary Micro-channel TPI Electrode	83
4.2.2 Micro Electrode Array	86
4.3 Electrical Set-Up and Data Collection	88
4.4 Calculations of Electric field Strengths	92
References	93
5. Cell Dielectrics Using Laplace Approach	94
5.1 Introduction	94
5.2 Materials and Methods	95
5.3 Dielectrophoretic velocity	96
5.3.1 <i>S.cervisiata</i>	96
5.3.1.1 Effect of cell densities	96
5.3.1.2 Effect of electric field strengths (E)	96
5.3.1.3 Effect of the Conductivity of the Suspending Medium	97
5.3.2 <i>Tetraselmis</i>	97
5.3.2.1 Effect of cell densities	98
5.3.2.2 Effect of electric field strengths (E)	98
5.3.2.3 Effect of the Conductivity of the Suspending Medium	98

CONTENTS (CONTINUED)

	Page
5.4 Data Fittings	99
5.5 Discussions and Conclusions	100
References	102
6. Cell Dielectrics Using the Impedance, RC-Model, Approach	126
6.1 Introduction	126
6.2 Cell Preparation and Density	127
6.3 Critical Frequencies	127
6.3.1 <i>S. cervisiata</i>	127
6.3.1.1 Effect of electric field strengths and cell densities	127
6.3.2 <i>Tetraselmis</i> sp.	127
6.3.2.1 Effect of electric field strengths and cell densities	127
6.4 Data Fittings	128
6.5 Discussions and Conclusions	128
References	129
7. Characterization of Dead and Arsenic Pretreated Cells	144
7.1 Introduction	144
7.2 Cell Preparations	145
7.3 Dielectrophoretic velocity and Critical frequency	145
7.3.1 <i>S. cervisiata</i>	145
7.3.2 <i>Tetraselmis</i>	146
7.4 Data Fittings	147
7.5 Discussions and Conclusions	147
References	149
8. Proof of Imaginary Function	160
8.1 Introduction	160
8.2 Methods to Investigate v_{twDEP}^p	161
8.3 Results	161

CONTENTS (CONTINUED)

	Page
8.4 Changes in Dielectric Parameters and σ_s	162
8.5 Discussion and Conclusions	163
References	163
9. Suggestions for Future Works	171
References	172
Vitae	173

LIST OF TABLES

Table	Page
2.1 Summary of the key equations derived in the present study for the computations.	65
5.1 Summary of the conductivities and dielectric constants of the cytoplasm, the cell membrane, and the suspending medium for <i>Tetraselmis</i> and <i>S. cervisiata</i> .	123
5.2 Comparison of dielectric parameters of the normal <i>S. cervisiata</i> and <i>Tetraselmis</i> with the literature. The conductance of the membrane (G_m) and the capacitance (C_m) were calculated from σ_m/δ and $\epsilon_0\epsilon_m/\delta$, where δ is the thickness of the cell boundary.	124
6.1 Summary of the dielectric parameters of the cytoplasm, the cell membrane, and the suspending medium for the control <i>Tetraselmis</i> and <i>S.cervisiata</i> .	143
7.1 Summary of the conductivities and dielectric constants of the cytoplasm, the cell membrane, and the suspending medium for the control, arsenic pretreated and heated cells.	158
7.2 Dielectric parameters of <i>S.cervisiata</i> and <i>Tetraselmis</i> under different treatment. All data was averaged from 3 separate experiments. The G_m and C_m was calculated from σ_m/δ and $\epsilon_0\epsilon_m/\delta$, where δ is the thickness of the cell boundary.	159

LIST OF FIGURES

Figure		Page
1.1	Ellipsoidal single shell models in (a) isometric and (b) top views which reveals the non-uniform shell thickness whereof two poles are smaller than that at equatorial area ($d_a, < d_b$).	6
1.2	Top view of the interdigitated electrode illustrated with two orthogonal forces acting on the spheroid. The \vec{F}_{cDEP} and \vec{F}_{twDEP} pushes the spheroid in $\pm x$ and $\pm y$ directions, respectively. A quadrature phases of $\phi_4 = \frac{3}{2}\pi$, $\phi_3 = \pi$, $\phi_2 = \frac{\pi}{2}$, $\phi_1 = 0$ (in radian) were addressed to the electrode.	9
2.1	A model of single shelled spheroid in the external AC electric field (\vec{E}) presented in (a) Isometric view shows its three semi-axes along x - y plane in which $a > b = c$ is condition. (b) Cross-sectional view shows all the dielectric parameters of cell compartments with a constant shell thickness δ (averaged value). All axes are measured from the center to the outer surface along their axis. The longest length (x axis) of the model aligns parallel to the vector field \vec{E} . The radial vector \vec{r} is measured from the center of the spheroid to point of interest located far away outside the spheroid.	20
2.2	A plot of a shelled spheroid from Eqs. (2.5) and (2.7) in x - y plane using Maple software version 9.01 (MapleSoft) where c was measured perpendicular to x - y plane. The following parameters were assumed for this plot: $a=10, b=c=6, u=15$ (u was calculated from Eq. 2.2) and $a_o = \sqrt{10^2 - 15} = \sqrt{85}$, $b_o = \sqrt{6^2 - 15} = \sqrt{21}$.	23
2.3	Theoretical plots of the real and the imaginary parts of the effective complex relative permittivity of a spheroid.	34
2.4	The complex plane plot (the Cole-Cole plot) of the effective complex relative permittivity obtained from the Laplace approach.	35

LIST OF FIGURES (CONTINUED)

Figure		Page
2.5	<p>Re[CMF] and Im[CMF] were plotted as a function of electric field frequency. Three field frequency ranges indicate the frequency regions where positive and negative DEP occur. The following parameters were employed for these plots:</p> $\sigma_c = 0.5\text{S.m}^{-1}, \sigma_m = 0.1\mu\text{S.m}^{-1}, \sigma_s = 0.01\text{S.m}^{-1},$ $\varepsilon_c = 60, \varepsilon_m = 10, \varepsilon_s = 78, \delta = 15\text{ nm and } L_x = 0.276.$	38
2.6	<p>The spectra of the real part of the Clausius-Mossotti factor [CMF] are affected by changing electrical parameters as described in the model. All solid lines were plotted using the parameters as shown in Fig. 2.5.</p>	43
2.7	<p>The spectra of the imaginary part of the Clausius-Mossotti factor [CMF] are affected by changing electrical parameters as described in the model. The solid lines were plotted using the parameters as shown in Fig. 2.5.</p>	47
2.8	<p>Theoretical plot of two critical frequencies, predicted from the Laplace approach. The f_λ and f_h were plotted by using the parameters as shown in Fig. 2.5.</p>	51
2.9	<p>The equivalent RC-model consists of 2 branches of the parallel of resistor-capacitor pairs.</p>	53
2.10	<p>Simplifications of two critical frequencies of the spheroidal model. Schemes for (a) a lower and (b) higher frequencies.</p>	57
2.11	<p>Theoretical plots of two critical frequencies for the lower (f_λ) and the higher (f_h) as a function of depolarizations factor (L_k). After adjusting the L_k value properly, the tips of two curves are jointed together. The following parameters were employed for these plots:</p> $\sigma_c = 0.5\text{S.m}^{-1}, \sigma_m = 0.1\mu\text{S.m}^{-1}, \sigma_s = 0.01\text{S.m}^{-1},$ $\varepsilon_c = 60, \varepsilon_m = 10, \varepsilon_s = 78 \text{ and } \delta = 15\text{ nm}.$	59

LIST OF FIGURES (CONTINUED)

Figure		Page
2.12	Theoretical plots show the lower (f_λ) and the higher (f_h) critical frequency as a function of medium conductivity (σ_s). Effects of changes in $\sigma_c, \sigma_m, \epsilon_c$ and ϵ_m is shown in (a) (b) (c) and (d), respectively.	60
3.1	Two orthogonal forces acting on the cells are presented in (a) top view (x - y plane) and (b) side view. The \vec{F}_{cDEP} directs the cell toward or repelled from the tip where the electric field strengths are larger or smaller. The \vec{F}_{twDEP} directs the cell toward the regions where the electrical phase is smaller (3) or larger (4).	69
3.2	Electric field strengths generated from the interdigitated electrode were calculated from the <i>Quick Field</i> TM program. The contour was plotted using the signal amplitude of 2.83 V (rms), the electric field frequency $f = 1\text{MHz}$, the conductivity of the suspending medium $\sigma_s = 0.01\text{S.m}^{-1}$. The maximum value of electric field gradient $\nabla E^2 = 3.3 \times 10^9 \text{V}^2.\text{m}^{-3}$ locates near the tip of the electrode.	72
3.3	Plots of dielectrophoretic and travelling wave dielectrophoretic forces acting on a spheroid. The following parameters were employed for these plots: $\sigma_c = 0.37\text{S.m}^{-1}, \sigma_m = 0.17\mu\text{S.m}^{-1}, \sigma_s = 0.01\text{S.m}^{-1}$, $\epsilon_c = 480, \epsilon_m = 8, \epsilon_s = 78 \delta = 13\text{nm}$ and $L_x = 0.276$.	73
3.4	Theoretical plots of the dielectrophoretic velocity of spheroid as a function of electric field frequencies during dielectrophoresis (solid line). The parameters used for these plots are the same as for Fig. 3.2.	76

LIST OF FIGURES (CONTINUED)

Figure		Page
3.5	Theoretical plots of dielectrophoretic velocity as transformed from the spheroidal model (Eq. 3.9) to a sphere by choosing three equal semi-axes ($a = b = c$) (see Fig. 2.1a also). The parameters used for these plots are the same as for Fig. 3.2.	76
4.1	<i>S.cervisiata</i> (TISTR 5088) were suspended in 0.5 M sorbitol.	81
4.2	<i>Tetraselmis</i> sp. suspended in the 0.5 M sorbitol medium.	81
4.3	Drop of cells suspension on the electrode was illustrated in (a) Side view and (b) Top view. The volume (V) of hemisphere of radius (r) was estimated from $\frac{4}{6}\pi r^3$ to be sure that $r \geq 4(d_1 + d_2)$.	84
4.4	The previous microchannel-TPI electrode. (a) Simulation of the microchannel of the electrode by using Coventor Ware TM and (b) the electrode connecting with microtube was mounted on the electrode's base.	85
4.5	One tip of the TPI electrode was damaged while the suspension was being feed through the microchannel.	86
4.6	A configuration of the TPI electrode and the quadrature phase sequence as shown in (a) three dimensional view (not to scale) and (b) diagram of electrical set up with an adjustable phase shift unit (PSU) connecting with an interjunction unit (IJU).	87
4.7	Pictures of (a) the adjustable Phase Shifted Unit (PSU) connected with (b) the Inter-Junction Unit (IJU).	89
4.8	Four output AC signals with zero time-delay measured from oscilloscope (100 MHz oscilloscope 2245A).	90
4.9	The "PSU" generated the quadrature phases with time-delay of 200 ms. When instantaneous states of four signals driven through cable A, B, C and D changed from state 1 to state 4 (a), the signals shifted to the right (b), or to the left (c) depending on operating knobs.	91

LIST OF FIGURES (CONTINUED)

Figure		Page
5.1	Comparison of v_{DEP}^p spectra of <i>S.cervisiata</i> when $\sigma_s = 0.01 \text{ S.m}^{-1}$ and electric field strengths were varied as (a) 28 kV.m^{-1} , (b) 57 kV.m^{-1} , and (c) 143 kV.m^{-1} .	104
5.2	Comparison of v_{DEP}^p spectra of <i>S.cervisiata</i> when $\sigma_s = 0.03 \text{ S.m}^{-1}$ and electric field strengths were varied as (a) 28 kV.m^{-1} , (b) 57 kV.m^{-1} , and (c) 143 kV.m^{-1} .	106
5.3	Comparisons of v_{DEP}^p spectra of <i>S.cervisiata</i> with difference of electric field strengths (E-field strength) when $\sigma_s = 0.01 \text{ S.m}^{-1}$ and cells density was varied as (a) $1.15 \times 10^5 \text{ cells.ml}^{-1}$ and (b) $5.75 \times 10^4 \text{ cells.ml}^{-1}$.	107
5.4	Comparisons of v_{DEP}^p spectra of <i>S.cervisiata</i> with difference of electric field strengths (E-field strength) when $\sigma_s = 0.03 \text{ S.m}^{-1}$ and cells density was varied as (a) $1.15 \times 10^5 \text{ cells.ml}^{-1}$ and (b) $5.75 \times 10^4 \text{ cells.ml}^{-1}$.	108
5.5	Comparisons of v_{DEP}^p spectra of <i>S.cervisiata</i> with difference of electric field strengths (E-field strength) when $\sigma_s = 0.06 \text{ S.m}^{-1}$ and cells density was varied as (a) $1.15 \times 10^5 \text{ cells.ml}^{-1}$ and (b) $5.75 \times 10^4 \text{ cells.ml}^{-1}$.	109
5.6	Comparisons of v_{DEP}^p spectra of <i>S.cervisiata</i> with difference of electric field strengths (E-field strength) when $\sigma_s = 0.10 \text{ S.m}^{-1}$ and cells density was varied as (a) $1.15 \times 10^5 \text{ cells.ml}^{-1}$ and (b) $5.75 \times 10^4 \text{ cells.ml}^{-1}$.	110
5.7	Comparison of v_{DEP}^p spectra of <i>Tetraselmis</i> when $\sigma_s = 0.01 \text{ S.m}^{-1}$ and	

LIST OF FIGURES (CONTINUED)

Figure		Page
	- electric field strengths were varied as (a) 28 kV.m ⁻¹ , (b) 57 kV.m ⁻¹ , and (c) 143 kV.m ⁻¹ , respectively.	112
5.8	Plots of v_{DEP}^p spectra of <i>Tetraselmis</i> when σ_s were varied as (a) $\sigma_s=0.03$ S.m ⁻¹ , (b) 0.06 S.m ⁻¹ and (c) 0.10 S.m ⁻¹ . Electric field strength was 28 kV.m ⁻¹ .	114
5.9	Comparisons of v_{DEP}^p spectra of <i>Tetraselmis</i> with difference of electric field strengths (E-field strength) when $\sigma_s = 0.01$ S.m ⁻¹ and cells density was varied as (a) 9.2×10^6 cells.ml ⁻¹ and (b) 4.0×10^5 cells.ml ⁻¹ .	115
5.10	Comparisons of v_{DEP}^p spectra of <i>Tetraselmis</i> with difference of electric field strengths (E-field strength) when $\sigma_s = 0.03$ S.m ⁻¹ and cells density was varied as (a) 9.2×10^6 cells.ml ⁻¹ and (b) 4.0×10^5 cells.ml ⁻¹ .	116
5.11	Comparisons of v_{DEP}^p spectra of <i>Tetraselmis</i> with difference of electric field strengths (E-field strength) when $\sigma_s = 0.06$ S.m ⁻¹ and cells density was varied as (a) 9.2×10^6 cells.ml ⁻¹ and (b) 4.0×10^5 cells.ml ⁻¹ .	117
5.12	Comparisons of v_{DEP}^p spectra of <i>Tetraselmis</i> with difference of electric field strengths (E-field strength) when $\sigma_s = 0.10$ S.m ⁻¹ and cells density was varied as (a) 9.2×10^6 cells.ml ⁻¹ and (b) 4.0×10^5 cells.ml ⁻¹ .	118

LIST OF FIGURES (CONTINUED)

Figure		Page
5.13	Curves fittings between experimental and theoretical data of cell translational speeds for <i>S.cervisiata</i> as a function of the electric field frequency. At 28 kV.m ⁻¹ when (a) $\sigma_s = 0.01 \text{ S.m}^{-1}$ and (b) $\sigma_s = 0.04 \text{ S.m}^{-1}$, experimental data were fitted with the theory using the dielectric parameters as shown in Table. 5.1. The χ value was calculated from Eq. 5.1.	120
5.14	The dielectrophoretic spectrum of <i>Tetraselmis</i> are affected by (a) the conductivities of the suspending medium (b) the electric field strengths while it is not clearly for (c) cell densities. Theoretical curves (the solid lines) were plotted by using the dielectric parameters as shown in Table 5.1.	122
5.15	Cell-to-Cell interaction calculated from the superposition of energy method. Total work to bring two polarizable spheroids to the center-to-center separation of r was plotted against the ration of r/R . Theoretical curve was plotted by using the following parameters: $a=10\mu\text{m}, b=8\mu\text{m}, c=8\mu\text{m}(R\approx 5\mu\text{m}), \delta=13\text{nm}, \epsilon_c=48, \epsilon_m=8, \epsilon_s=78,$ $\sigma_c=0.37\text{S.m}^{-1}, \sigma_m=0.17\mu\text{S.m}^{-1}, \sigma_s=0.01\text{S.m}^{-1}, \text{Re}[CMF]=1.0,$ $E^2 \cong 1 \times 10^{10} \text{ V}^2.\text{m}^{-2}.$	125
6.1	Comparisons of critical frequencies between 1.15×10^5 and $5.75 \times 10^4 \text{ cell.m}\lambda^{-1}$ yeast cells when the electric field strengths were increased from (a) 28 kV.m ⁻¹ , (b) 57 kV.m ⁻¹ and (c) 143 kV.m ⁻¹ , respectively.	133
6.2	A comparison of experimental critical frequencies of yeast cells for (a) $1.15 \times 10^5 \text{ cell.m}\lambda^{-1}$ and (b) $5.75 \times 10^4 \text{ cell.m}\lambda^{-1}$ when the electric field strengths were changed.	135
6.3	Experimental critical frequencies of <i>Tetraselmis</i> for 9.2×10^6 and $4.0 \times 10^5 \text{ cell.m}\lambda^{-1}$ were plotted when electric field strengths were increased from 28 kV.m ⁻¹ to 143 kV.m ⁻¹ , respectively.	138

LIST OF FIGURES (CONTINUED)

Figure		Page
6.4	A comparison of experimental critical frequencies of <i>Tetraselmis</i> for (a) $9.2 \times 10^6 \text{ cell.m}\lambda^{-1}$ and (b) $4.0 \times 10^5 \text{ cell.m}\lambda^{-1}$ when the electric field strengths were changed.	140
6.5	Data fitting of the lower critical frequencies for <i>S.cervisiatae</i> . The theoretical curve was plotted by using the parameters as shown in Table 6.1.	141
6.6	Data fitting of the lower critical frequencies for <i>Tetraselmis</i> . The theoretical curve was plotted by using the parameters as shown in Table 6.1.	142
7.1	Comparisons of dielectrophoretic velocity spectra of the control and heated <i>S. cervisiatae</i> when (a) $\sigma_s = 0.01 \text{ S.m}^{-1}$ and (b) $\sigma_s = 0.04 \text{ S.m}^{-1}$. Cell density was $1.15 \times 10^5 \text{ cells.ml}^{-1}$ and electric field strength was 28 kV.m^{-1} . Curve-fitting were drawn as the solid line to obtain cells dielectric parameters as shown in Table 7.1.	152
7.2	Comparison of f_λ of the controlled and heated <i>S. cervisiatae</i> (a). The curve-fitting of heated cell below 0.04 S.m^{-1} is extended in (b). The solid line is theoretical curves plotted by using the parameters as shown in Table 7.1.	153
7.3	Dielectrophoretic velocity spectra of <i>Tetraselmis</i> suspended in 0.01 S.m^{-1} when electric field strength (E) was 28 kV.m^{-1} . The theoretical lines were drawn by using the following parameters: $\sigma_s = 0.01 \text{ S.m}^{-1}$, $\sigma_m = 3 \times 10^{-6} \text{ S.m}^{-1}$, $\sigma_c = 0.37 \text{ S.m}^{-1}$, $\epsilon_c = 48$, $\epsilon_s = 78$, $a = 10$, $b = c = 8 \mu\text{m}$ and $\delta = 13 \text{ nm}$.	154
7.4	Effect of concentrations of arsenic solution on the lower critical frequency spectra of the arsenic pretreated <i>Tetraselmis</i> compared with the controlled cells. Experimental data (dots) were obtained from the experimentation which used the electric field strength $E = 28 \text{ kV.m}^{-1}$ and $\sigma_s = 0.01 \text{ S/m}$.	155

LIST OF FIGURES (CONTINUED)

Figure		Page
7.5	Plot of the dielectrophoretic spectrum of the heated <i>Tetraselmis</i> as compared with the control cells. Theoretical curves (the solid) was plotted by using the dielectric parameters as shown in Table 7.1.	156
7.6	Plots of Re[CMF] and Im[CMF] of the controlled and the heated <i>S.cervisiata</i> by using the dielectric parameters as shown in Table 7.1. Three frequency ranges were indicated at the lower, intermediate and the higher frequency which relate with \hat{F}_{cDEP} and \hat{F}_{twDEP} , where f_λ and f_h are the critical frequencies of \hat{F}_{cDEP} at the lower and the higher, respectively.	157
8.1	Top view of the cell being repelled from the electrode tip showed the resultant force \hat{F}_R (a) acting on the cell where the strong propagating field area was shown in side view (b).	165
8.2	Plot of magnitude of travelling wave dielectrophoretic velocity (\hat{v}_{twDEP}) of the controlled yeast cells by using the dielectric parameters shown in Table 6.1.	166
8.3	Plot of magnitude of travelling wave dielectrophoretic velocity (\hat{v}_{twDEP}) of the controlled <i>Tetraselmis</i> by using the dielectric parameters shown in Table 6.1.	167
8.4	Plots of Re[CMF] and Im[CMF] of the controlled and the boiled yeast cells by using the dielectric parameters as shown in Table 7.1. Three frequency ranges were indicated at the lower, intermediate and the higher frequency which relate with $\pm \hat{F}_{cDEP}$ and $\pm \hat{F}_{twDEP}$ at the lower and the higher, respectively.	168
8.5	Comparisons of Re[CMF] and Im[CMF] of (a) the controlled and the 1 ppm arsenic pretreated <i>Tetraselmis</i> sp. cells and several of (b) 5, 10, 50, 150 ppm arsenic concentrations. All curves were plotted by using the dielectric parameters as shown in Table 7.1.	170

LIST OF SYMBOLS

- ε' : Permittivity (F.m⁻¹)
 ε_o : Vacuum permittivity (= 8.85x10⁻¹² F.m⁻¹)
 ε : Relative permittivity , $\varepsilon = \varepsilon'\varepsilon_o^{-1}$ (dimensionless)
 ε_{ij} : Relative permittivity of ij phase (dimensionless)
 ε^* : Complex relative permittivity(dimensionless)
 σ : Electrical conductivity
 ω : Angular electric field frequency
 f_λ : Lower critical frequency
 f_h : Higher critical frequency
DEP: Dielectrophoresis
cDEP: Conventional dielectrophoresis
twDEP: Travelling wave dielectrophoresis
TPI: Two parallel interdigitated electrode
[CMF]: Clausius-Mossotti factor
Re[CMF]: Real part of [CMF]
Im[CMF]: Imaginary part of [CMF]
 ε_{eff}^* : Effective complex relative permittivity of the whole cell
 L_k : Depolarization factor
 V : Cell volume
 σ_{ct} : Critical conductivity of a medium
 $\overset{\nu}{F}_{cDEP}$: Conventional dielectrophoretic force
 $\overset{\mathcal{P}}{F}_{DEP}$: Net time-average DEP force
 $\overset{\nu}{F}_{twDEP}$: Travelling wave dielectrophoretic force (twDEP force)
 $\overset{\mathcal{P}}{F}_{twDEP}$: Net time-average twDEP force
 $\nabla\phi_i$: Phase non-uniformity factor of i component
 Z_{eff}^* : Effective complex impedance

LIST OF SYMBOLS (CONTINUED)

a, b, c	Three semi-axes of spheroid
$\overset{\rho}{E}$	Electric field
δ	Shell thickness
ψ	Electrical potentials
$\overset{\rho}{\mu}_{eff}$	Effective dipole moment
η	Viscosity
$\overset{\rho}{F}_g$	Gravitational force
$\overset{\rho}{F}_D$	Drag force
K'	Shape factor
$\overset{\rho}{v}_{cDEP}$	Conventional dielectrophoretic velocity
$\overset{\rho}{v}_{twDEP}$	Travelling wave dielectrophoretic velocity
C_m	Specific capacitance of a membrane
G_m	Specific conductance of a membrane
U	Total work
r	Radial distance
$v_{exp.(i)}$	Magnitudes of experimental dielectrophoretic velocity
$v_{theory(i)}$	Magnitudes of theoretical dielectrophoretic velocity
N	Number of data points

CHAPTER 1

INTRODUCTION

1.1 An Overview of the Present Study

Traveling wave dielectrophoresis (twDEP), closely related to the conventional dielectrophoresis (cDEP), has shown potential applications in medical diagnostics, drug delivery and biological cell therapeutics in terms of selectivity, isolation, concentration, purification and separation of bio-particles mixtures (Talarly *et al.*, 1996; Pethig *et al.*, 2003). In principle, twDEP is the phenomenon resulting from interactions between traveling electric field and the induced electric dipole moment of cell or dielectric particle suspended in such field (Hagedorn *et al.* 1992; Huges, 2000). Normally, traveling electric field could be generated by using multi-bar electrode with different electric phase such as interdigitated electrode. Previously, twDEP studies were reported using a planar linear interdigitated electrode of one array (Masuda *et al.*, 1988; Huges, 2000; Jones, 2003; Pethig *et al.*, 2003) and then two parallel arrays (Fuhr *et al.*, 1991; Hagedorn *et al.* 1992; Wang *et al.*, 1995; Talarly *et al.*, 1996; Fu *et al.*, 2004). The driven electric field was generated by sinusoidal quadrature-phase voltages. A phase sequence addressed to the electrodes had been described in details elsewhere (Fuhr *et al.*, 1991; Wang *et al.*, 1995; Huges, 2000; Jones, 2003; Pethig *et al.*, 2003; Fu *et al.*, 2004).

For two parallel interdigitated electrode (TPI) arrays, the Clausius - Mossotti factor [CMF], the factor concerning the dipole moment of the cell, composed of real (Re[CMF]) and imaginary (Im[CMF]) functions determined by the complex conductivity and permittivity of the cell in combination with the cell medium. These functions are frequency dependent and hence might affect the cell by either collecting it at the TPI or pushing it through electrode central channel, respectively. The negative value of Re[CMF] results in the negative cDEP force and the cell being repelled from the electrode, represented by a negative velocity, and vice

versa. The mathematical model for the frequency dependence of cDEP force including the traveling force in the middle of the central channel, for a sphere in traveling wave, was firstly derived by Wang *et al.* (1995). These two forces are each orthogonal. This allows, in principle, cells with different properties to be separated by choice of an appropriate frequency range.

The present study is the first time to determine forces acting on a spheroid (one kind of an ellipsoid whose any two semi-axes is equal) in travelling electric field. The mathematical model has further extended from the spherical model (Wang *et al.*, 1995) to the spheroid by using the Laplace method to explain cell velocities in travelling electric field in term of cell dielectric properties. Also, impedance (RC model) approach proposed by Gimsa and Wachner (1998) was developed to express two boundary frequencies for positive DEP at lower (f_λ) and higher (f_h) frequency, the so called “critical frequency”. Yeast cells, *Saccharomyces cervisiata*, and phytoplankton, *Tetraselmis* sp., were used as the spheroidal model. Also, comparison studies between living and dead cells of *S.cervisiata* including arsenic pretreated *Tetraselmis* were made and cell dielectric properties of these cells were determined through the functions of the cell velocity and two critical frequencies.

1.2 The Conventional Dielectrophoresis (cDEP)

The phenomenon of the conventional dielectrophoresis (cDEP) is the translational motion of dielectric particles and biological cells in a non-uniform electric field due to polarization effects. When a cell is polarized, the dipole moment ($\vec{\mu}$) of the cell interior interacts with the electric field gradient (∇E^2). Interaction between the dipole and the electric field leads to a net translational force, the so called “dielectrophoretic force” (DEP force). The net (time-average) DEP force (\overline{F}_{DEP}) (Pohl, 1978) was defined as

$$\overline{F}_{DEP} = (\overline{\mu \cdot \nabla}) E^2 \quad (1.1)$$

where $\vec{\mu} = \varepsilon_0 \varepsilon_s^* V [\text{CMF}] \vec{E}$, and ε_0 , ε_s^* and V represent permittivity of vacuum ($8.85 \times 10^{-12} \text{ F.m}^{-1}$), the complex relative permittivity of the suspending medium and cell volume, respectively. The \vec{F}_{DEP} causes cell translation in which its magnitude determines the cell speed. The direction of the translation is either towards or away from a region of the stronger electric field, depending on whether the relative permittivity and the conductivity of the cell is greater or less than that of a suspending medium, respectively. As reported previously by Landau and Lifschitz (1985) and later by Jones (1995), and Gimsa and Wachner (1999), a comparison between the two dielectric properties was deduced in terms of a frequency-dependent complex function known as the Clausius-Mossotti factor ([CMF]), which is,

$$[\text{CMF}] = \frac{\varepsilon_{eff}^* - \varepsilon_s^*}{\varepsilon_s^* + (\varepsilon_{eff}^* - \varepsilon_s^*) L_k}, \quad (1.2)$$

where ε_{eff}^* and L_k is the effective complex relative permittivity of the whole cell and a depolarization factor, respectively. The [CMF] description is based on the knowledge of the electrical cell model in which ε_{eff}^* describes dielectric properties of the cell.

For the present study, ε_{eff}^* was extended for a spheroid and clarified in term of a (relative) permittivity and conductivity of a cell membrane and cytoplasm.

1.3 Techniques for Estimation of Cell Dielectric Properties via DEP

Cell electro-mechanics are non-invasive techniques which can be employed to study cell behaviors such as dielectrophoresis and electro-rotation. Many researchers (Pohl, 1978; Pohl and Crane, 1971; Gimsa *et al*, 1991; Jones, 1995; Zhou

et al. 1995 and 1996; Mahaworasilpa *et al.*, 1994 and 1996; Radu *et al.*, 1996; Wanichapichart *et al.*, 2002) have explained these behaviors and formulated equations to estimate cell properties in measurable terms such as critical and characteristic frequencies, cell velocity, and angular velocity. In all cases, experimental data was collected and plotted so that the equations could be verified by curve fittings. Such experiments were conducted using small organisms, of a few micron such as yeast cells (*S. cervisiata*) (Raicu *et al.*, 1996), *Chlorella* sp. and *Tetraselmis* sp. (Wanichapichart *et al.*, 2002a) to cells of around a hundred micron such as *Lilium longiflorum* or even larger cell like *Dendrobium* protoplast (Wanichapichart *et al.*, 2002b). All of these cells are too small for a direct dielectric measurement and dielectrophoresis provides a tool to determine these dielectric parameters and gain an estimate of the membrane thickness.

Cell electro-mechanics techniques, however, have advantages and drawbacks. The technique is suitable for a single cell and requires high intensity electric field (kilovolt/meter) to induce cell translation or rotation. Also, the electric fields at the lower frequency may cause Joule-heating - rather harmful to the cell. Another method is dielectric spectroscopy, for characterization of cell suspensions under low intensity electric field (less than kilovolt/meter). The latter method, as proposed by Asami *et al.* (1996), requires an impedance analyzer connected to dielectric probes which are immersed directly in the cell suspensions. Although, it consumes less time than the former method, Bunthawin and Boonlamp (2005) suggested that it might be costly and hence not suitable for preliminary studies. In this respect, the electro-mechanics was chosen for this study, since it relies on some measurable experimental data such as velocity of the cell translation (v_{cDEP}^p) (Mahaworasilpa *et al.*, 1994). Previously, a single cell was carefully selected and cell velocity was recorded at a corresponding field frequency. The real part of [CMF] was plotted against field frequency and curve fitting was made so that dielectric parameters could be estimated (Mahaworasilpa *et al.*, 1994; Wanichapichart *et al.*, 2002a). The method was, however, rather tedious and time consuming. The accuracy of the velocities obtained in such method was also questionable, since the uniform velocity required for the measurement could be achieved only in a short period, leading to some uncertainties in the data collected.

Some workers reported an alternative method by recording two critical frequencies (f_λ, f_h) of DEP instead (Gimsa *et al.*, 1991). Gimsa and his colleagues proposed that two critical frequencies lead to estimations of dielectric values of spherical and ellipsoidal cells. Theoretically, the two frequencies were expressed in term of the angular frequency ($\omega = 2\pi f$) through the Laplace approach which relates directly to the $\text{Re}[\text{CMF}]$, and becomes zero. The data fitting results in estimations of the cell's electrical properties such as conductivities and dielectric constants, depending on the geometric structure of the assumed model for the cell.

In 1998, Gimsa and Wachner proposed that applying the Laplace approach to an ellipsoid raised “the confocal shell problem”. They believed that the Laplace description of biological cells or evenly coated dielectric particles by the common confocal spheroidal models may lead to large errors in the case of extreme axis ratios. These errors, arising from an ill-defined layer thickness, will be found for the general ellipsoidal case.

Actually, the previous theoretical study done by Asami *et al.* (1980) had encountered the confocal shell problem resulting from the nonuniform of shell thickness (see Fig. 1.1). Based on his model, the effective complex relative permittivity ε_{eff}^* of a shelled ellipsoid was assumed to be anisotropic. This means that dielectric properties of ellipsoid as determined from x , y and z axes are different.

Watanabe *et al.* (1991) attempted to correct the ambiguities of the confocal problem by using the average of shell thickness. According to his calculation through the Laplace approach, the thickness was assumed not to exceed 1% of the length of either semi-axis of the ellipsoid. As the result, the average thickness was about 0.85 fold of the shell thickness at equatorial. Similarly, Miller and Jones (1993) suggested that if the shell thickness is very thin (less than 10 nm), the confocal shell problem may be neglected.

To circumvent the confocal shell problem, Gimsa and his colleagues proposed the RC-model which unifies the theory of a resistor-capacitor model in term of specific impedances. For his derivation, cells of prismatic geometry embedded in elementary cubes formed by the external solution were assumed. All geometry structures of the model were described by parallel circuits of a resistor and a capacitor.

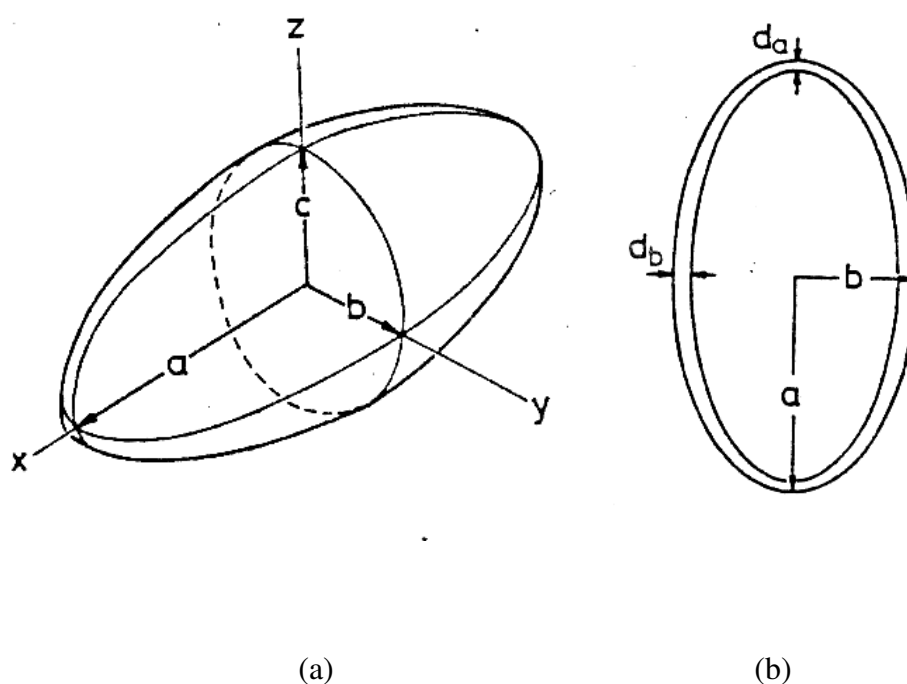


Fig. 1.1. Ellipsoidal single shell models in (a) isometric and (b) top views which reveals the non-uniform shell thickness whereof two poles are smaller than that at equatorial area ($d_a < d_b$).

The impedance of the cell suspension is given by a meshwork of elementary cubes. Each elementary cube was modeled by two branches describing the current flow through and around the cell. It is interesting that this work derived the Clausius-Mossotti factor ([CMF]) in term of the impedance, instead of permittivity. Also, the RC-model predicts the potential at the ellipsoid's surface leading to the calculation of an induced dipole moment. This approach provided equations for $\text{Re}[\text{CMF}]$ and two critical frequencies, the frequencies corresponding with the positive dielectrophoresis at the lower (f_λ) and the higher (f_h).

Following Gimsa's approach, this study thus extends the RC-model to explain the critical conductivity of the medium (σ_{ct}) in term of cell dielectric parameters and to examine dielectric properties of a spheroidal cell in travelling wave.

1.4 Ellipsoidal Shell Model

Based on the Laplace approach, various types of a spherical model had been developed from time to time (Scher, 1968; Pohl, 1978; Schwan, 1988; Kaler and Jones, 1990 Gimsa *et al.*, 1991; Irimajiri *et al.*, 1978; Irimajiri *et al.*, 1979; Asami and Irimajiri, 1984). For non-spherical models, Saito *et al.* (1966) were the first to propose an ellipsoidal model without shell and was then extended by many investigations such as Asami *et al.*, (1980), Paul and Otwinowski, (1991), Watanabe *et al.* (1991), Miller and Jones (1993) and Zhou *et al.* (1996), respectively. These models were derived on the basis of an energy method to calculate the potential energy stored inside and outside of the ellipsoid and from which the effective complex relative permittivity \mathcal{E}_{eff}^* was obtained.

In 1996, Zhou *et al.* investigated the dielectric properties of the pretreated yeast cells (*Saccharomyces cerevisiae*) by using a double-shelled ellipsoidal model. He demonstrated the effect of the biocide Cosmocil (polyhexxannide), before and after treatment, at different concentrations on yeasts by using the electro-rotation technique. Experimentations were carried out over the field frequency range from 1 kHz to 10 MHz. Estimations of cell dielectric properties were made through a curve-fitting method. The results showed that the conductivity of the cell membrane (σ_m) and of the cytoplasm (σ_c) were $0.25 \pm 0.10 \mu\text{S.m}^{-1}$ and $0.20 \pm 0.05 \text{S.m}^{-1}$, and for pretreated yeast were $5.5 \pm 0.3 \mu\text{S.m}^{-1}$ and $0.01 \pm 0.02 \text{S.m}^{-1}$, respectively. In the same year, Radu *et al.* employed the electro-rotation method to estimate the values of σ_m and σ_c of the normal and beta-mercaptoethanol pretreated yeast cells. The results for the normal were $0.40 \pm 0.12 \mu\text{S.m}^{-1}$ and $0.11 \pm 0.03 \text{S.m}^{-1}$ and for the pretreated cells were $25 \pm 8 \mu\text{S.m}^{-1}$ and $0.01 \pm 0.02 \text{S.m}^{-1}$, respectively.

Two year later, Raicu *et al.* observed effects of cetyltrimethylammonium bromide (CTAB) surfactant on the dielectric properties of yeast cells (Baker's yeast). The results from dielectric spectroscopy measurements on cell suspensions showed that the conductivities of vacuole interior decreased drastically as

CTAB was increased. The specific capacitance of the vacuole membrane and the conductivity of the inner vacuole were estimated to be $0.650 \mu\text{F}\cdot\text{cm}^{-2}$ and $3.1 \text{S}\cdot\text{m}^{-1}$ and for the pretreated cells were $0.718 \mu\text{F}\cdot\text{cm}^{-2}$ and $1.5 \text{S}\cdot\text{m}^{-1}$, respectively.

1.5 Traveling Wave Dielectrophoresis (twDEP)

For two parallel interdigitated electrode (TPI) arrays (Fig. 1.2), Masuda *et al.* (1988) were the first to demonstrate that travelling electric field of very low frequency (around 100 Hz) could be used to induce the controlled translation and circular motions of biological cells. Later Fuhr *et al.* (1991) found cells translation along the track of much higher frequencies (10 kHz-39MHz). Theoretical analysis of twDEP force acting on a sphere was clearly made by Huang *et al.* (1992) and Hagedorn *et al.* (1992). It is evident that twDEP force is obviously proportional to the imposed electric field strength (E), cell size (r) and the imaginary part of the Clausius-Mossotti factor, $\text{Im}[\text{CMF}]$, whereas cDEP translation is related to the real part, $\text{Re}[\text{CMF}]$. In case of a scalar form of the time-averaged twDEP force in the central region of the track was shown to be given by:

$$\bar{F}_{\text{twDEP}} = \frac{-4\pi^2 r^3 \varepsilon_0 \varepsilon_s \text{Im}[\text{CMF}] E^2}{\lambda}, \quad (1.3)$$

where λ is a periodic distance between electrode bars of the same phase and it is constant for the quadrature case since an interdigitated structure is symmetric.

Wang and his co-worker (1995) developed the mathematical functions to describe both of the cDEP and twDEP forces acting on a sphere as a generalized form (gDEP) based on the Laplace approach. The time-averaged gDEP force is given by

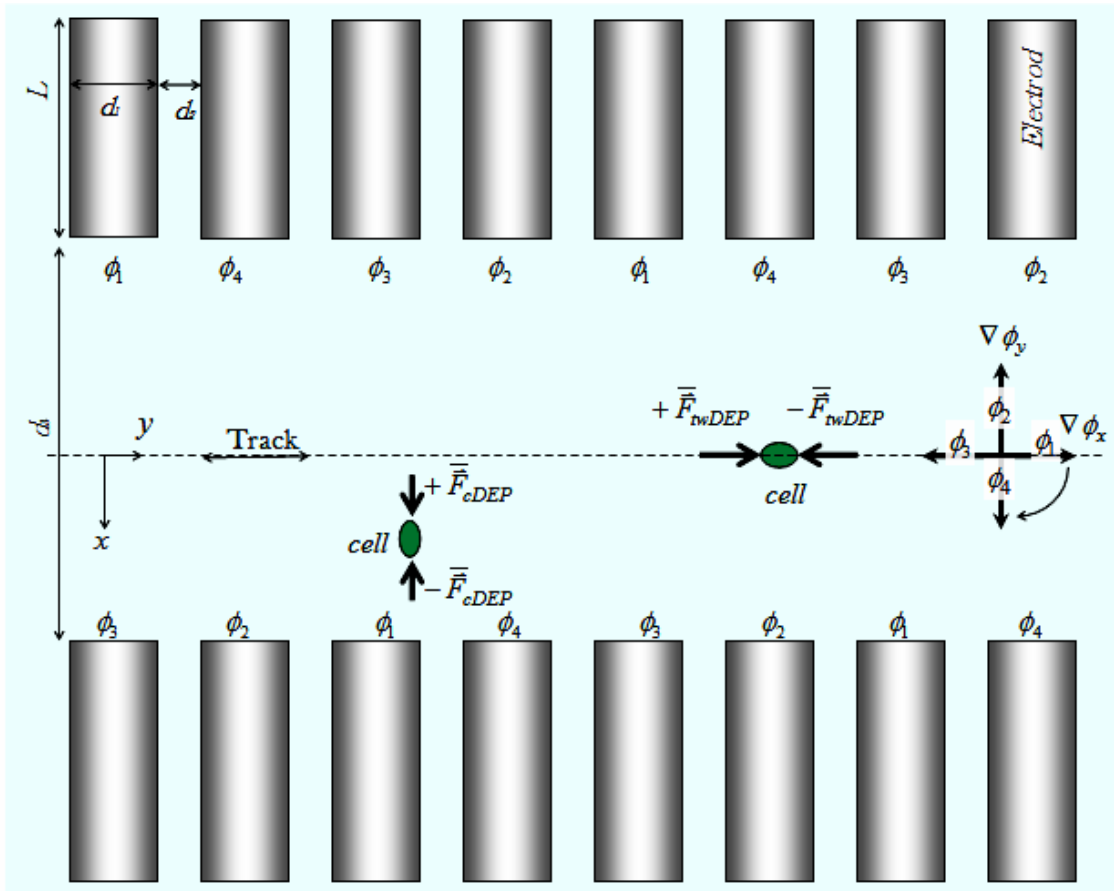


Fig. 1.2 Top view of the interdigitated electrode illustrated with two orthogonal forces acting on the spheroid. The \vec{F}_{cDEP} and \vec{F}_{twDEP} pushes the spheroid in $\pm x$ and $\pm y$ directions, respectively. A quadrature phases of $\phi_4 = \frac{3}{2}\pi$, $\phi_3 = \pi$, $\phi_2 = \frac{\pi}{2}$, $\phi_1 = 0$ (in radian) were addressed to the electrode.

$$\vec{F}_{gDEP} = 2\pi r^3 \varepsilon_0 \varepsilon_s \left[\text{Re}[\text{CMF}] \vec{\nabla} E^2 + \text{Im}[\text{CMF}] \left(\sum_{i=x,y,z} E_i^2 \vec{\nabla} \phi_i \right) \right], \quad (1.4)$$

where $\vec{\nabla} \phi_i$ is the phase non-uniformity factor of i component corresponding to a phase difference of E_i . $\vec{\nabla} E^2$ represents the gradient term of the non-uniform spatial distribution of the imposed field. The first and the second terms in the bracket reveal a conventional dielectrophoresis force ($\vec{F}_{cDEP} = 2\pi r^3 \varepsilon_0 \varepsilon_s \text{Re}[\text{CMF}] \vec{\nabla} E^2$) and a travelling wave dielectrophoresis ($\vec{F}_{twDEP} = 2\pi r^3 \varepsilon_0 \varepsilon_s \text{Im}[\text{CMF}] \sum_{i=x,y,z} E_i^2 \vec{\nabla} \phi_i$), respectively. These forces direct cells in perpendicular vectors which has advantages for cells manipulation.

1.6 Motivation and the Highlight of This Study

A study of cell electro-mechanics is a method to observe cell behaviors in an intense electric field (Pohl, 1978). The benefit obtained from such study was to obtain cell dielectric properties. Previously, determination of cell dielectric properties was made through a curve-fitting which requires measurements of a single cell translational velocity during dielectrophoresis and the experiments were carried out in animal and plant cells by using two cylindrical parallel electrodes (Mahaworasilpa *et al.*, 1994; Wanichapichart *et al.*, 2002). A single cell was carefully selected and the cell velocity was recorded at specified field frequencies. The real part of frequency dependent complex function ($\text{Re}[\text{CMF}]$) was plotted against field frequency and curve fitting was used to estimate the dielectric parameters. The method was, however, rather tedious and time consuming. The accuracy of the velocities obtained in such method was also questionable, since the uniform velocity required for during the measurement could be achieved only in a short period. Also, in case of ellipsoidal cell (including a spheroid), the confocal shell problem of “the thicker membrane at the two

poles than the equatorial area” (Asami *et al.* 1980; Watanabe *et al.*, 1991; Gimsa *et al.*, 1998 and 1999) brought about questions of the validity of the method. Calculation of two critical frequencies (f_λ, f_h) of the spheroid through the Laplace approach, concerning with the computation of ϵ_{eff}^* (Assmi *et al.* 1980; Watanabe *et al.*, 1991), was rather mathematically complicated. Another approach has been developed by Gimsa and his colleges (1998 and 1999) using impedance (RC model) approach to correct the ambiguous about the membrane thickness.

Recently, our previous work (Bunthawin *et al.*, 2007) has combined two critical frequencies with cell dielectrophoretic velocity measurements in order to determine cell dielectric properties through a curve-fitting method from both Laplace and impedance approaches. However, for cells of *S.cervisiata*, it was observed that the simplified impedance model did not fit well with the experimental data, particularly at the lower frequency region due to the model approximations. Also, the critical frequency obtained from the real part of the Clausius-Mossotti factor (Re[CMF]) through the Laplace approach was rather mathematically complicate. One aspect of the present study was aimed at clarifying the extended impedance approach to examine dielectric properties for a spheroidal cell such as *S.cervisiata* and *Tetraselmis*.

For cell separation works, it is important to know dielectric properties of cells in suspension in order to calculate the precise frequency for the separation in AC electric fields. The former study done by Wanichapichart and her colleges (Sudsiri *et al.*, 1999) reported AC electric field frequencies for isolating five marine phytoplanktons. The experiments which were carried out by using two parallel cylindrical electrodes were achieved in laboratory scale experiments with static fluidics and corresponding cell separations using microfluidic flow were not investigated. Later, a planar linear interdigitated electrode of one array and traveling wave dielectrophoresis (twDEP) technique was employed by Thongnuaeha (2005). The advantages of TPI electrode was already known in detail elsewhere (Pethig *et al.*, 2003; Tararly *et al.*, 1996) and hence to extend the separation work from the previous studies, a two parallel interdigitated electrode (TPI) was employed for the present study. For spheroid suspensions, the time-averaged gDEP force (Eq. 1.4) was adapted for use with a spheroidal model and the twDEP force acting on the spheroid was

calculated to obtain the optimization of microfluidic flow rate. Living and dead cells of *S.cervisiata* and *Tetraselmis* were used as a model and the results were compared with those obtained from our electro-rotation technique (Wanichapichart *et al.*, 2007). Since arsenic contamination in surface water has been evidenced in South Thailand, it was interesting to investigate how cell changes in the dielectric properties after arsenic absorption. Experimental results together with those from the reported literature were compared to validate the developed spheroidal model.

1.7 Aims of the present study

1. To extend the theoretical analysis for the travelling wave dielectrophoretic force of a spherical particle to that of a spheroid via the Laplace and impedance (RC model) approaches.
2. To evaluate cell dielectric properties from measurements of the velocity and two critical frequencies of cells undergoing DEP.

References

1. Asami K. and Irimajiri A. 1984. Dielectric analysis of mitochondria isolated from rat liver II. Intact mitochondria as simulated by a double shell model. *Biochim Biophys Acta* 778: 570-578.
2. Asami K., Hanai T. and Koizumi N. 1980. Dielectric approach to suspensions of ellipsoidal particles covered with a shell in particular reference to biological cells. *Jpn J. Appl Phys* 19: 359-365.

3. Asami K., Yonezawa T., Wakamatsu H. and Koyanagi N. 1996. Dielectric spectroscopy of biological cell. *Bioelectrochem Bioenerg* 40:141-145.
4. Asami K. 2002. Characterization of biological cells by dielectric spectroscopy. *Non-Crystal Solids* 305: 268-277.
5. Bunthawin S., Butrat P. and Boonlamp M. 2003. Development of a computer program to investigate electrical properties of Phuket pineapple leaf single cells by using dielectrophoresis. *Songklanakarinn J Sci Technol* 25: 227-237.
6. Bunthawin S. and Boonlamp M. 2005. Development of a single cells spherical shell model for an investigation of electrical properties with computing program. *Songklanakarinn J Sci Technol* 27: 393-416.
7. Cen, E.G., Dalton, C., Li, Y., Adamia, S., Pilarski, L.M. and Kaler, K.V.I.S. 2004. A combined dielectrophoresis, traveling wave dielectrophoresis and electrorotation – microchip for the manipulation and characterization of human malignant cells. *J.Microbio.Method*, 58:387-401.
8. Fuhr, G. and Kuzmin P.I. 1986. Behaviour of cells in rotating electric fields with account to surface charges and cell structures. *J. Biophysics* 50: 789- 795.
9. Fu, L.M., Lee, G.B., Lin, Y.H. and Yang, R.J. 2004. Manipulation of microparticles using new modes of traveling –wave-Dielectrophoretic Force: Numerical simulation and experiments. *J.IEEE/ASME Trans.Mechatronics.*, 9(2):377-383.
10. Gheorghiu G. 1996. Measuring living cells using dielectric spectroscopy. *BioelectroBioenerg* 40: 387-401.
11. Gimsa J., Graser R. and Fuhr G. 1988. Remarks on the field distribution in four electrode chambers for electrorotational measurements. *Studia biophysica*. 125: 71-76.

12. Gimsa J., Marszalek P., Loewe U. and Tsong T. 1991. Dielectrophoresis and electrorotation of neurospora slime and murine myeloma cells. *Biophys J* 60:749-760.
13. Gimsa J., Muller T., Schnelle T. and Fuhr G. 1996. Dielectric spectroscopy of single human Erythrocytes at physiological ionic strength: Dispersion of the cytoplasm. *Biophys J* .71:495-506.
14. Gimsa J. and Wachner D. 1998. A unified resistor-capacitor model for impedance, dielectrophoresis, electrorotation and induced transmembrane potential. *Biophysical J*. **75**: 1107-1116.
15. Gimsa J. and Wachner D. 1999. A polarization model overcoming the geometric restrictions of the Laplace solution for spheroidal cells: Obtaining new equations for field-induced forces and transmembrane potential. *Biophysical J* **77**: 1316-1326.
16. Green, N.G., Romos, A. and Morgan, H. 2002. Numerical solution of the dielectrophoretic and traveling wave forces for interdigitated electrode array using the finite element method. *J.Electrostatics*, 56:235-254.
17. Hagedorn, R., Fuhr, G., Muller, T., and Gimsa, J. 1992. Traveling-wave dielectrophoresis of microparticles. *Electrophoresis*, 13:49-54.
18. Hughes, M.P. 1999. AC electrokinetics: Applications for nanotechnology. Draft paper for the Seventh Foresight Conference on Molecular Nanotechnology.
19. Irimajiri A., Doida Y., Hanai T. and Inouye A. 1978. *J.Membrane.Biol.* 38:209-232
20. Irimajiri A., Hanai T. and Inouye A. 1979. *J.Theor.Biol.* 78: 251-269
21. Jones T. B. 1995. *Electromechanics of Particles*. Cambridge University Press, Cambridge, pp. 2.

22. Kaler K. V. I. S. and Jones T. B. 1990. Dielectrophoretic spectra of single cells determined by feedback-controlled levitation. *Biophys J.* **57**:173-182.
23. Lippert S. and Gimsa J. 2002. High resolution measurements of dielectric cell properties by a combination of AC-electrokinetic effects. In: *2nd International Workshop on Biological effects of EMFs at Rhodes Greece. 7-11 October 2000*, pp. 830-836.
24. Li, W.H., Du, H., Chen, D.F., and Chu, C. 2004. Analysis of dielectrophoretic electrode arrays for nanoparticles manipulation. *J. Comp. Materials. Sci.*, 30:320-325.
25. Mahaworasilpa T., Coster H.G.L. and George E.P. 1994. Force on biological cells due to Applied (AC) electric fields. I. Dielectrophoresis. *Biochim Biophys Acta* 1193: 118-126.
26. Mahaworasilpa T., Coster H. G. L. and George E. P. 1996. Force on biological cells due to applied (AC) electric fields. II. Electro-rotation. *Biochim. Biophys Acta* 1281: 5-14.
27. Marszalek P., Zienlinsky J. J., Fikus M. and Tian Y. T. 1991. Determination of electric parameters of cell membranes by a dielectrophoresis method. *Biophys J* 59: 982-987.
28. Mark, G. H. and Davey, C. L. 1999. The dielectric properties of biological cells at radiofrequencies: Applications in biotechnology. *Enzyme and microbial technol.* 25: 161-171.
29. Maxwell, J. C. 1891. A Treatise on Electricity and Magnetism, 3rd. ed., Vol.1, Ch.IX, Clarendon Press, Oxford.
30. Pant, K., Feng, J., Wang, G., Krishnamoorthy, S. and Sundaram, S. 2003. Separation of bioparticulate matter using traveling wave dielectrophoresis. 7th

International conference on Miniaturized Chemical Analysis Systems October 5-9, Squaw Valley, California USA.

31. Pauly H. and Schwan H. P. 1959. *Naturforsch.* 14b: 125.

32. Pethig R. and Markx M. H. 1997. Applications of dielectrophoresis in biotechnology. *Trends and Biotechnol.* 15: 426-432.

33. Pohl H. A. 1978. Dielectrophoresis: The Behaviour of Neutral Matter in Non-Uniform Electric Fields. Cambridge University Press, Cambridge.

34. Pohl H. A. and Crane J.S. 1971. Dielectrophoresis of cells. *Biophys J* 11: 711-727.

35. Radu M, Petcu I, Sommer A. and Avram D (1996) Change in membrane electrical parameters of yeast following chemical treatment for protoplast isolation. *J Bioelectrochem Bioenerg* 40: 159-166.

36. Raicu V., Raicu G. and Turcu G. 1996. Dielectric properties of yeast cells as simulated by the two-shell model. *Biochim. Biophys. Acta*, 1274:143-148.

37. Raicu V., Gusbeth C., Anghel D. F. and Turcu G. 1998. Effect of cetyltrimethylammonium bromide (CTAB) surfactant upon the dielectric properties of yeast cells. *Biochim. Biophys. Acta*. 1379:7-15.

38. Scher L.D. 1968. Dielectrophoresis in lossy dielectric media. *Nature* 220: 695-696.

39. Schwan H.P. 1988. Dielectric spectroscopy and electro-rotation of biological cells. *J Ferroelectrics* 86: 205-223.

40. Saito M., Schwan H.P. and Schwarz G. 1966. Response of nonspherical biological particles to alternating electric fields. *Biophys J.* 6: 313-327.

41. Sudsiri J., Wanichapichart P., Mahaworasilpa T. and Coster H.G.L. 1999. AC electric field frequencies for isolating five marine phytoplanktons. *Songklanakarin J Sci Technol* 21(2): 213-219.
42. Thongnuaeha, S. Traveling wave dielectrophoresis for viable and non-viable *Tetrasemis* sp. in solution. Project submitted to Department of Physics, Prince of Songkla University, 2005.
43. Wagner, K. W. 1914. *Archiv. Elektrotechnik* 2, S.371-389.
44. Wanichapichart P., Boontawin, S., Kaewpiboon, A., and Kanchanapoom, K. 2002a. Determination of dielectric properties of single cells by dielectrophoretic method. *Science Asia* 28(2): 113-119.
45. Wanichapichart P., Maswiwat, K., and Kanchanapoom, K. 2002b. Elastic constant of *Dendrobium* protoplasts in AC electric field. *Songklanakarin J Sci Technol* 24(Suppl.): 799-806.
46. Wanichapichart P., Wongluksanapan, T., and Khooburat, L. 2007. Electrorotation: Diagnostic tool for abnormality of marine phytoplankton cells. The 2nd IEEE International Conference on Nano/Micro Engineering and Molecular Systems., 1115-1120.
47. Watanabe M., Toshinobu S. and Irimajiri A. 1991. Dielectric behavior of the frog lens in the 100Hz to 500 MHz range: Simulation with an allocated ellipsoidal-shells model. *Biophys J* 59:139-149.
48. Zimmermann U. and Vienken J. 1982. Electric field-induced cell-to-cell fusion. *J Membrane Biol* 67: 165-182.

CHAPTER 2

THEORETICAL APPROACHES FOR DETERMINING CRITICAL FREQUENCIES FOR A SPHEROIDAL MODEL

2.1 Introduction

As mentioned in chapter 1 (section 1.2), the spheroidal model derived through the Laplace approach introduces problems related to the confocal shell viz. the thicker membrane at the two poles compared with the thickness at the equatorial area. The extended impedance approach is provided in this chapter to overcome the confocal problem and compared with the Laplace approach to examine dielectric properties for *S.cervisiata* and *Tetraselmis*. It is the first time clarifying mathematical expressions of two critical frequencies for a spheroidal model (f_λ, f_h). Both the Laplace and impedance approaches are used. The analyses were made based on the condition of zero dielectrophoretic force (F_{cDEP}) as first suggested by Pohl (1978). For the Laplace approach, the zero force also relates with the value of the zero $\text{Re}[\text{CMF}]$ in which the effective complex permittivity of the spheroid ε_{eff}^* is equal to that of the suspending medium ε_s^* (see Eq. 1.2 in chapter 1). Two critical frequencies were then solved by using the frequency dependence of $\text{Re}[\text{CMF}]$ as a polynomial function of an angular frequency ($\omega = 2\pi f$). Dielectric dispersion of cell compartments at lower and higher frequency range were taken into account to extract two values of f_λ and f_h from the electric field frequencies (f) appearing in $\text{Re}[\text{CMF}]$, derived in this chapter. For the impedance approach, the effective complex impedance (Z_{eff}^*) replaced by ε_{eff}^* of the Laplace approach to derive the value of $\text{Re}[\text{CMF}]$. Calculations of f_λ and f_h from both approaches were given in the following sections.

2.2 The Critical frequencies: Laplace approach

To calculate two critical frequencies for a spheroid, one needs to know the geometry of the model so that calculations of spheroidal volume, ε_{eff}^* , [CMF] and $\text{Re}[\text{CMF}]$ can be evaluated term by term. Theoretical analyses of these functions provided in this chapter were the identity of the present study.

2.2.1 The Geometry of the Spheroidal Model

A spheroid is an ellipsoid whose any two semi-axes are equal, as shown in Fig. 2.1a where three semi-axes are defined as $a > b = c$ and $b = c$. The spheroid is suspended in the external solution (s) with the external electric field (\vec{E}). The single shell and the outer closed compartment of the model (Fig. 2.1b) represent the cell membrane (m) and the cytoplasm (c), respectively. For a lossy, complex and heterogeneous spheroid (Jones, 1995), the dielectric properties of the spheroid can be expressed in term of real and imaginary parts i.e. $\varepsilon_{eff}^* = \text{Re}[\varepsilon_{eff}^*] + j \text{Im}[\varepsilon_{eff}^*]$, where $j = \sqrt{-1}$.

The conductive (σ) and capacitive (ε) properties of the membrane (σ_m, ε_m), the cytoplasm (σ_c, ε_c) and the suspending solution (σ_s, ε_s) are identified as shown in Fig. 2.1b.

Using the Maple software (version 9.01), a two-dimensional spheroid in x - y plane, as shown in Fig. 2.2, was used for the simulations. The values of a_o, b_o, c_o measured from the center to the inner surface of the spheroid are assumed to identify three inner lengths along x , y and z , respectively (the c value was measured in perpendicular direction from x - y plane).

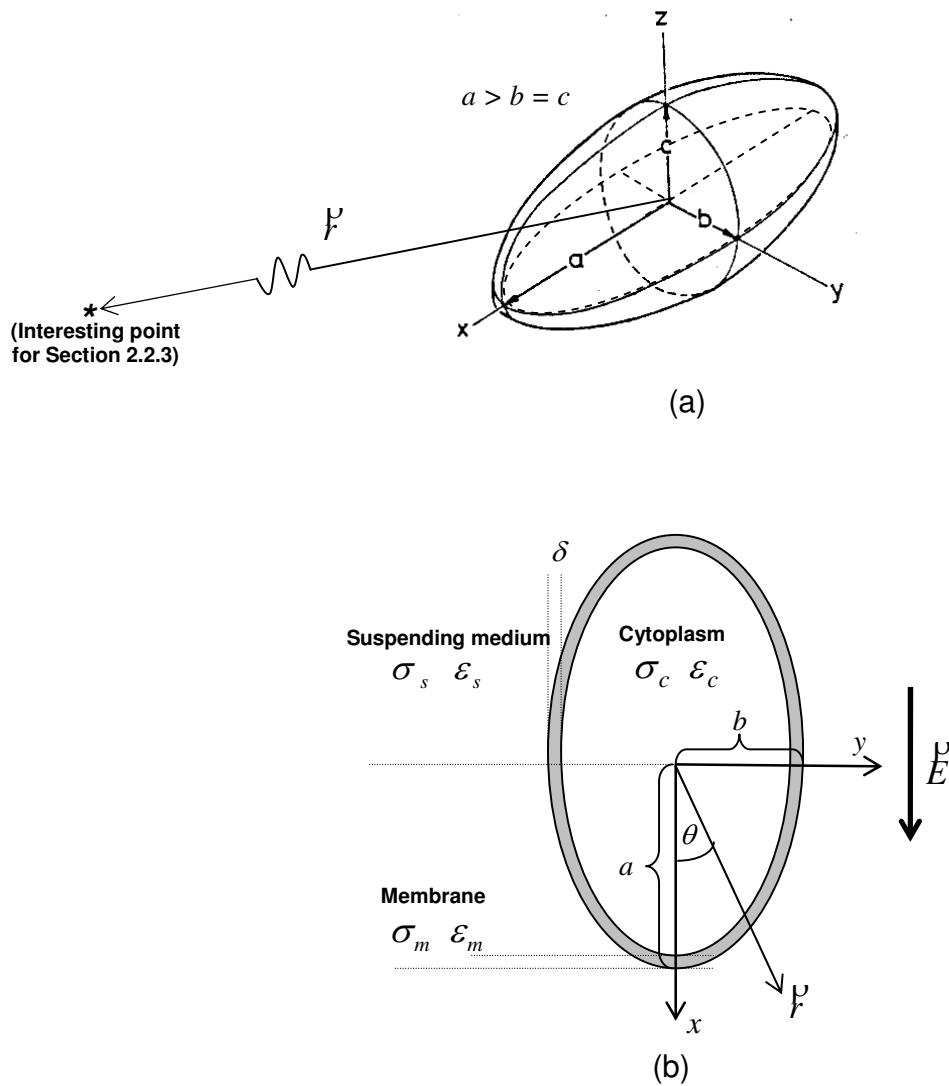


Fig. 2.1 A model of a single shelled spheroid in an external AC electric field (\vec{E}). Views of (a) isometric represents its three semi-axes along x - y plane where $a > b = c$ and (b) cross-section shows all the dielectric parameters of cell compartments with a constant shell thickness δ (an averaged value). All axes are measured from the center to the outer surface along their axis. The longest length (x axis) parallels the vector field of \vec{E} . The radial vector \vec{r} is measured from the center of the spheroid to the interesting point locating far away outside the spheroid.

The space between the inner and the outer surfaces presents the shell thickness (δ). As seen from Fig. 2.2, this approach and definition of the spheroidal particle introduces a nonuniform of shell thickness, the so called “confocal shell problem”. The coordinate employed for Fig 2.2 is expressed as

$$\frac{x^2}{a^2 + \xi} + \frac{y^2}{b^2 + \xi} + \frac{z^2}{c^2 + \xi} = 1, \quad (2.1)$$

where ξ is a parameter representing a family of confocal ellipsoids and $\xi > -c^2$. $\xi = 0$ and $\xi = -u$ represents the boundaries of the outer and the inner surface, respectively. The inner lengths of a_o, b_o, c_o are given by:

$$a_o = \sqrt{a^2 - u}, \quad b_o = \sqrt{b^2 - u}, \quad c_o = \sqrt{c^2 - u}, \quad (2.2)$$

or

$$u = a^2 - a_o^2, \quad u = b^2 - b_o^2, \quad u = c^2 - c_o^2. \quad (2.3)$$

With a focus on the outer surface ($\xi = 0$), Eq. (2.2) becomes

$$\frac{x^2}{a^2} + \frac{y^2}{b^2} + \frac{z^2}{c^2} = 1. \quad (2.4)$$

For a two-dimension plot in the x - y plane, Eq. (2.4) reduces to $\frac{x^2}{a^2} + \frac{y^2}{b^2} = 1$ which can be rearranged as

$$y(x) = \pm b \sqrt{1 - \frac{x^2}{a^2}}. \quad (2.5)$$

Similarly, Eq. (2.1) can be extended for the inner surface where $\xi = -u$,

$$\frac{x^2}{a^2 - u} + \frac{y^2}{b^2 - u} + \frac{z^2}{c^2 - u} = 1. \quad (2.6)$$

In case of two-dimensional plot, Eq. (2.6) is reduced to $\frac{x^2}{a^2 - u} + \frac{y^2}{b^2 - u} = 1$, leading to

$$y(x) = \pm \sqrt{(b^2 - u) \left(1 - \frac{x^2}{a^2 - u} \right)}. \quad (2.7)$$

Plots of the outer and the inner surface of the spheroid (Fig. 2.2) are based on Eqs. (2.5) and (2.7), respectively, where $a = 10, b = c = 6, u = 15$, $a_o = \sqrt{10^2 - 15} = \sqrt{85}$, $a_o = \sqrt{10^2 - 15} = \sqrt{85}$, $b_o = \sqrt{6^2 - 15} = \sqrt{21}$. These parameters were defined by Stratton (1941) and can be expanded to yield the following:

$$\text{spheroid:} \quad \frac{x^2}{a^2 + \xi} + \frac{y^2}{b^2 + \xi} + \frac{z^2}{b^2 + \xi} = 1, \quad (\xi > -b^2) \quad (2.8)$$

$$\text{hyperboloid of one sheet:} \quad \frac{x^2}{a^2 + \eta} + \frac{y^2}{b^2 + \eta} + \frac{z^2}{c^2 + \eta} = 1, \quad (-c^2 > \eta > -b^2) \quad (2.9)$$

$$\text{hyperboloid of two sheets:} \quad \frac{x^2}{a^2 + \zeta} + \frac{y^2}{b^2 + \zeta} + \frac{z^2}{c^2 + \zeta} = 1, \quad (-b^2 > \zeta > -a^2) \quad (2.10)$$

where ξ, η, ζ represents a family of confocal spheroids in three-dimensions i.e. in x, y , and z (Stratton, 1941, pp. 52-59). These three parameters will be employed in derivation of the effective complex permittivity in the next section. However, here mathematical -

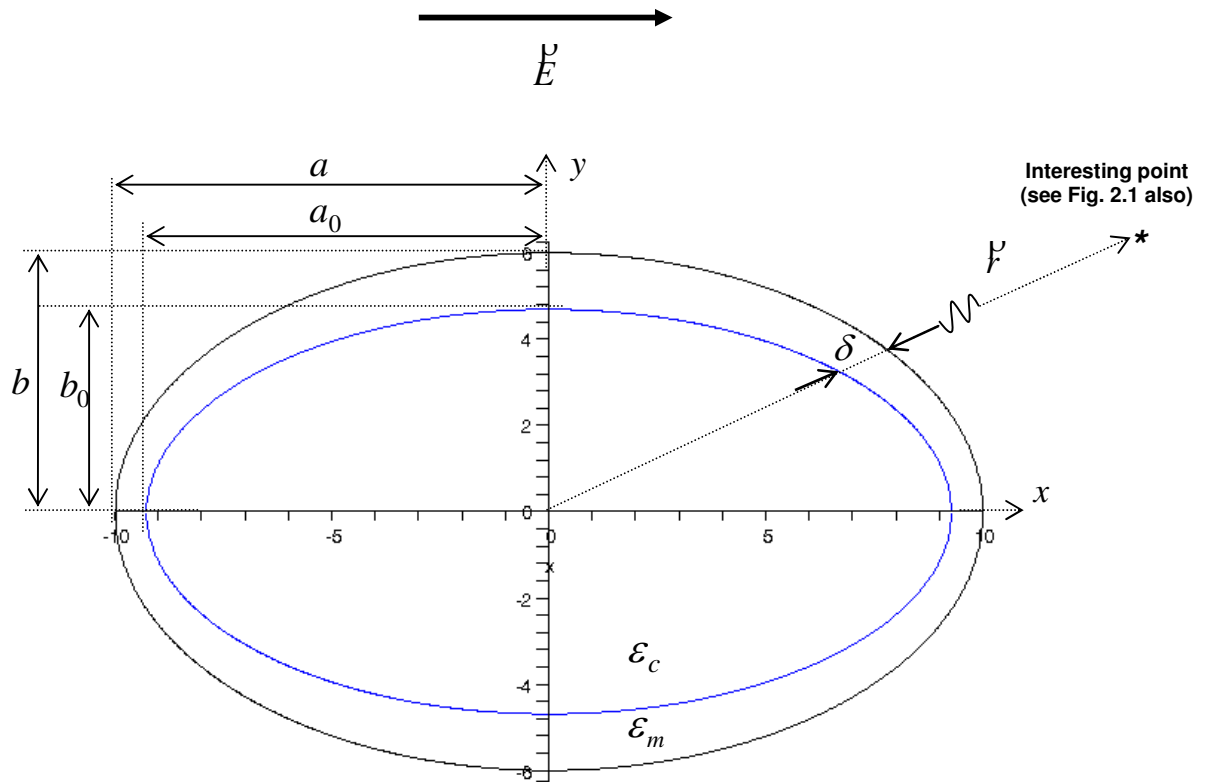


Fig. 2.2 A plot of a shelled spheroid from Eqs. (2.5) and (2.7) in x - y plane using Maple software version 9.01 (MapleSoft) where c was measured perpendicular to x - y plane.

The following parameters were assumed for this plot: $a = 10, b = c = 6, u = 15$ (u was

calculated from Eq. 2.2) and $a_0 = \sqrt{10^2 - 15} = \sqrt{85}, b_0 = \sqrt{6^2 - 15} = \sqrt{21}$.

tractibility, the shell thickness (δ) is considered as an averaged value (see Fig. 2.1b) so that the membrane capacitance is constant over the shell.

2.2.2 An Effective Complex Relative Permittivity

As shown in Fig. 2.1, the spheroid possesses two different dielectric compartments. To depict the dielectric properties, the effective permittivity of the whole spheroid becomes a complex function (ϵ_{eff}^*) as suggested by Pohl (1978) and Jones (1995). In AC electric field (\vec{E}), the ϵ_{eff}^* is also frequency dependent.

In order to solving for ϵ_{eff}^* , Laplace's equation is employed to analyze the electrical potentials (ψ). The spheroid is placed in external homogeneous field $\vec{E}(E_x, E_y, E_z)$. The potential is then given by a solution of Laplace's equation,

$$\vec{\nabla} \cdot \vec{\nabla} \psi = 0, \quad (2.11)$$

or

$$\vec{\nabla}^2 \psi = 0, \quad (2.12)$$

Applying Eq. 2.8, Stratton (1941) showed that Laplace's equation can be written in form

$$\vec{\nabla}^2 \psi = \frac{4}{(\xi - \eta)(\xi - \zeta)(\eta - \zeta)} \left[\begin{array}{l} (\eta - \zeta)R_\zeta \frac{\partial}{\partial \xi} \left(R_\zeta \frac{\partial \psi}{\partial \xi} \right) + (\zeta - \xi)R_\eta \frac{\partial}{\partial \eta} \left(R_\eta \frac{\partial \psi}{\partial \eta} \right) + \\ (\xi - \eta)R_\zeta \frac{\partial}{\partial \zeta} \left(R_\zeta \frac{\partial \psi}{\partial \zeta} \right) \end{array} \right], \quad (2.13)$$

The ξ , η and ζ in this equation will be represented as S . Then R_ξ , R_η and R_ζ can be re-written as R_s , hence $R_s = \sqrt{(s+a^2)(s+b^2)(s+c^2)}$. To satisfy equation (2.13), the potential ψ must fulfill the following conditions:

- (a) be regular at infinity, and
- (b) be constant over the given spheroid

The variables η and ζ are the parameters of confocal hyperboloids and serve to measure position on any spheroid with $\xi = \text{constant}$ (see explanations of Eqs. 2.1). On the surface $\xi = 0$, ψ must be independent of η and ζ . If one can find a function depending only on ξ which satisfies those conditions, it can be adjusted to represent the potential correctly at any point outside the spheroid at $\xi = 0$. It is evident that $\psi = \psi(\xi)$ and the Laplace's equation reduces to

$$\nabla^2 \psi = \frac{\partial}{\partial \xi} \left(R_\xi \frac{\partial \psi}{\partial \xi} \right) = 0, \quad (2.14)$$

where $R_\xi = \sqrt{(\xi + a^2)(\xi + b^2)(\xi + c^2)}$.

It should be noted that the condition of $a > b = c$ was kept through this study for the "prolate" spheroid (for "an oblate", if $a < b = c$). If $\xi = 0$ and $\xi = -u$, these represent the outer and the inner surface of the shelled spheroid, respectively (see Fig. 2.2 also).

Integration of Eq. (2.14) over the volume from ξ to infinity yields $\psi(\xi) = c \int_\xi^\infty \frac{d\xi}{R_\xi}$, where

c is an arbitrary constant which can be obtained by using the method described by Stratton (1941).

The electrical potential at a point which is infinitely remote from the spheroid (ψ_o) relates directly to that of the original field, i.e.

$$\text{At } \xi \rightarrow \infty, \quad -\psi_o = xE_x + yE_y + zE_z. \quad (2.15)$$

From the continuity principle, the electric potential along the normal component (n), as considered through the shell, from the inner to the outer surface can be expressed as

$$\text{For } \xi = 0: \quad \psi_o = \psi_m \text{ and } \varepsilon_o^* \frac{\partial \psi_o}{\partial n} = \varepsilon_m^* \frac{\partial \psi_m}{\partial n}. \quad (2.16)$$

$$\text{For } \xi = -u: \quad \psi_m = \psi_c \text{ and } \varepsilon_m^* \frac{\partial \psi_m}{\partial n} = \varepsilon_c^* \frac{\partial \psi_c}{\partial n}, \quad (2.17)$$

where the asterisks represents the complex, the subscripts c and m indicate the cytoplasm and the membrane regions, respectively. Stratton (1941) showed that the potentials at the inner and the outer of the spheroid can be expressed as a function of the effective complex relative permittivity ($\varepsilon_{eff}^*(k)$) in three-dimension, i.e.

$$\psi_c = - \left[\frac{E_x x}{1 + \frac{(\varepsilon_{eff}^*(x) - \varepsilon_s^*)}{\varepsilon_s^*} L_x} + \frac{E_y y}{1 + \frac{(\varepsilon_{eff}^*(y) - \varepsilon_s^*)}{\varepsilon_s^*} L_y} + \frac{E_z z}{1 + \frac{(\varepsilon_{eff}^*(z) - \varepsilon_s^*)}{\varepsilon_s^*} L_z} \right], \quad (2.18)$$

and

$$\begin{aligned} \psi_o = & -E_x x \left\{ 1 - \frac{\varepsilon_{eff}^*(x) - \varepsilon_s^*}{\varepsilon_s^* + (\varepsilon_{eff}^*(x) - \varepsilon_s^*)L_{ax}} L'_{ax} \right\} - E_y y \left\{ 1 - \frac{\varepsilon_{eff}^*(y) - \varepsilon_s^*}{\varepsilon_s^* + (\varepsilon_{eff}^*(y) - \varepsilon_s^*)L_{by}} L'_{by} \right\} - \\ & E_z z \left\{ 1 - \frac{\varepsilon_{eff}^*(z) - \varepsilon_s^*}{\varepsilon_s^* + (\varepsilon_{eff}^*(z) - \varepsilon_s^*)L_{cz}} L'_{cz} \right\}, \end{aligned} \quad (2.19)$$

where

$$\varepsilon_{eff}^*(k) = \varepsilon_m^* \left[\frac{\varepsilon_m^* + (\varepsilon_c^* - \varepsilon_m^*)L_{jk} + v(\varepsilon_c^* - \varepsilon_m^*)(1 - L_{ik})}{\varepsilon_m^* + (\varepsilon_c^* - \varepsilon_m^*)L_{jk} - v(\varepsilon_c^* - \varepsilon_m^*)L_{ik}} \right], \quad (2.20)$$

and $k=x, y, z$. It should be noted that $\varepsilon_m^* = \varepsilon_m - j \frac{\sigma_m}{\omega \varepsilon_0}$, $\varepsilon_c^* = \varepsilon_c - j \frac{\sigma_c}{\omega \varepsilon_0}$ and v represents the fractional volume of the spheroid. The L_{ik} and L_{jk} are the depolarization factors depending on the value of a, b and c (the geometry of the spheroid). Explanations of L_{ik} and L_{jk} are given in the next section.

2.2.3 Depolarization Factors

Asami *et al.* (1980) defined the depolarization factors along k axis as L_{ik} (the outer surface) and the L_{jk} (the inner surface) as the function of

$$L_{ik} = \frac{abc}{2} \int_0^\infty \frac{ds}{(s + R_{ik}^2)R_{is}} \quad \text{and} \quad L_{jk} = \frac{abc}{2} \int_0^\infty \frac{ds}{(s + R_{jk}^2)R_{js}}, \quad \text{respectively.}$$

R_{ik} and R_{jk} are the semiaxes of the outer and the inner surface along k -axis, respectively,

$$R_{is} = \sqrt{(R_{ix}^2 + s)(R_{iy}^2 + s)(R_{iz}^2 + s)} \quad \text{and} \quad R_{jk}^2 = R_{jk}^2 - s \quad \text{where } s = \xi, \eta, \zeta \text{ is the parameter representing}$$

a family of the confocal surface (Eqs. 2.8 to 2.10). For the spheroid where $s = \xi$ and $b=c$

(see the geometry of the model in section 2.2.1), the following equations are the expansions of the depolarization factors along x , y and z of the outer and the inner surface.

The outer surface $L_{ik}, i = a, b, c$ The inner surface $L_{jk}, j = a_o, b_o, c_o$

$$L_{ax} = \frac{abc}{2} \int_0^\infty \frac{d\xi}{(\xi + a^2)R_{ax}}, \quad L_{a_o x} = \frac{a_o b_o c_o}{2} \int_0^\infty \frac{d\xi}{(\xi + a_o^2)R_{a_o x}},$$

$$L_{by} = \frac{abc}{2} \int_0^\infty \frac{d\xi}{(\xi + b^2)R_{by}}, \quad L_{b_o y} = \frac{a_o b_o c_o}{2} \int_0^\infty \frac{d\xi}{(\xi + b_o^2)R_{b_o y}},$$

$$L_{cz} = L_{by}, \quad L_{c_o z} = L_{b_o y},$$

where $L_{ax} + L_{by} + L_{cz} = 1$ and $L_{a_o x} + L_{b_o y} + L_{c_o z} = 1$.

Analytical solutions of these equations are not simple. However, approximations of the depolarization factors can be made. Consider a point of interest located far away outside the spheroid (see Fig. 2.1), at a distance r from the center which is much greater than the length of each semi-axes, that is $r \gg a_o, b_o, c_o$ (see Fig. 2.2). Then Eq. (2.1) can be reduced to

$$\frac{x^2}{\xi} + \frac{y^2}{\xi} + \frac{z^2}{\xi} = 1, \quad (2.21)$$

where $\xi \cong r^2$. Under the assumed location, L'_{ik} is reduced to the following forms,

$$L_{ik} = \frac{abc}{2} \int_\xi^\infty \frac{d\xi}{(\xi + i^2)R_{is}} \approx \frac{abc}{2} \int_\xi^\infty \xi^{-5/2} d\xi = \frac{abc}{2} \frac{2}{3} \xi^{-3/2} \approx \frac{abc}{3} \frac{1}{r^3}, \quad (2.22)$$

$$\text{with } L'_{ax} = L'_{by} = L'_{cz} \approx \frac{abc}{3} \frac{1}{r^3}, \quad (2.23)$$

In case of the prolate spheroid ($a > b = c$), the function R_{ik} may be written in forms

$$R_{ax} = R_{by} = R_{cz} = \sqrt{(\xi + a^2)(\xi + b^2)^2} = R_{ik}. \quad (2.24)$$

Then Eq. (2.22) can be simplified to the form

$$L_k = \frac{abc}{2} \int_0^\infty \frac{d\xi}{(\xi + k^2)R_{ik}} = \frac{ab^2}{2} \int_0^\infty \frac{d\xi}{(\xi + a^2)(\xi + a^2)^{1/2}(\xi + b^2)} = \frac{ab^2}{2} \int_0^\infty \frac{d\xi}{(\xi + a^2)^{3/2}(\xi + b^2)},$$

$$L_k = \frac{ab^2 \tan^{-1}\left(\frac{\sqrt{\xi + a^2}}{\sqrt{-\xi + b^2}}\right)}{(a^2 - b^2)\sqrt{-a^2 + b^2}} + \frac{ab^2}{(a^2 - b^2)\sqrt{\xi + a^2}}. \quad (2.25)$$

Substituting $\xi = 0$ and $q = \frac{a}{b}$ in Eq. (2.25), a family of depolarization factors can be obtain by using Maple software (version 9.01). These are,

For a prolate spheroid ($a > b = c$),

$$L_x = \left(\frac{-1}{q^2 - 1}\right) + \left(\frac{q}{(q^2 - 1)^{3/2}}\right) \ln(q + (q^2 - 1)^{1/2}), \quad (2.26)$$

$$L_y = L_z = \frac{1 - L_x}{2}, \quad (2.27)$$

$$q = \frac{a}{b} > 1. \quad (2.28)$$

It should be noted that if $c = 0$, the spheroid degenerates into a circular disk, such as the frog lens (Watanabe *et al.*, 1991).

For an oblate spheroid ($a = b > c$),

$$L_x = \left(\frac{1}{1-q^2} \right) - \left(\frac{q}{(1-q^2)^{3/2}} \right) \cos^{-1} q, \quad (2.29)$$

$$L_y = L_z = \frac{1-L_x}{2}, \quad (2.30)$$

$$q = \frac{a}{b} < 1. \quad (2.31)$$

For a sphere, then

$$L_k = \frac{1}{3} \text{ and } q = 1. \quad (2.32)$$

Further simplification of L_{ik} and L_{jk} can be made. Considering that the membrane is very thin with thickness of about 6 nm (of *C. corallina*) (Coster and Chilcott, 2002). In this case the membrane thickness is negligible compared to a , b and c . Examples of a spheroid are yeast cells and *Tetraselmis* sp. The longest axes (a) are ranged from 8 to 10 μm . As a consequence, the axial ratio for the outer surface of the shell (q_{outer}) is nearly equal to that of the inner (q_{inner}) that is

$$q_{outer} = \frac{a}{b} \approx q_{inner} = \frac{a_o}{b_o}. \quad (2.33)$$

Hence, the depolarization factor of the outer spheroid is equal to that of the inner spheroid i.e. $L_{ik} = L_{jk}$, then the Eq. (2.20) becomes

$$\mathcal{E}_{eff(k)}^* = \mathcal{E}_m^* \left(\frac{\mathcal{E}_m^* + (\mathcal{E}_c^* - \mathcal{E}_m^*)(L_k + \nu(1-L_k))}{\mathcal{E}_m^* + (\mathcal{E}_c^* - \mathcal{E}_m^*)(L_k + (1-\nu))} \right), \quad (2.34)$$

where ν was directly obtained by using some algebra and $\nu = \left(1 - \frac{\delta}{a}\right) \left(1 - \frac{\delta}{b}\right)^2$. Since Eq.

(2.34) can be resolved along three orthogonal axes, it can be written in a matrix form as

$$\mathcal{E}_{eff(k)}^* = \begin{pmatrix} \mathcal{E}_{eff(xx)}^* & 0 & 0 \\ 0 & \mathcal{E}_{eff(yy)}^* & 0 \\ 0 & 0 & \mathcal{E}_{eff(zz)}^* \end{pmatrix} = \begin{pmatrix} \mathcal{E}_{eff(x)}^* \\ \mathcal{E}_{eff(y)}^* \\ \mathcal{E}_{eff(z)}^* \end{pmatrix}. \quad (2.35)$$

Such expression is known in mathematic term as biaxial in which each component is expressed as

$$\mathcal{E}_{eff(x)}^* = \mathcal{E}_m^* \left[\frac{\mathcal{E}_m^* + (\mathcal{E}_c^* - \mathcal{E}_m^*)L_x + \nu(\mathcal{E}_c^* - \mathcal{E}_m^*)(1-L_x)}{\mathcal{E}_m^* + (\mathcal{E}_c^* - \mathcal{E}_m^*)L_x - \nu(\mathcal{E}_c^* - \mathcal{E}_m^*)L_x} \right], \quad (2.36)$$

$$\mathcal{E}_{eff(y)}^* = \mathcal{E}_m^* \left[\frac{\mathcal{E}_m^* + (\mathcal{E}_c^* - \mathcal{E}_m^*)L_y + \nu(\mathcal{E}_c^* - \mathcal{E}_m^*)(1-L_y)}{\mathcal{E}_m^* + (\mathcal{E}_c^* - \mathcal{E}_m^*)L_y - \nu(\mathcal{E}_c^* - \mathcal{E}_m^*)L_y} \right], \quad (2.37)$$

$$\mathcal{E}_{eff(z)}^* = \mathcal{E}_m^* \left[\frac{\mathcal{E}_m^* + (\mathcal{E}_c^* - \mathcal{E}_m^*)L_z + \nu(\mathcal{E}_c^* - \mathcal{E}_m^*)(1-L_z)}{\mathcal{E}_m^* + (\mathcal{E}_c^* - \mathcal{E}_m^*)L_z - \nu(\mathcal{E}_c^* - \mathcal{E}_m^*)L_z} \right]. \quad (2.38)$$

For the homogeneous dielectric, these three components are equal, i.e.

$$\mathcal{E}_{eff(x)}^* = \mathcal{E}_{eff(y)}^* = \mathcal{E}_{eff(z)}^*, \quad (2.39)$$

These can be rewritten in terms of a complex relative permittivity as

$$\varepsilon_{eff}^* = \text{Re}[\varepsilon_{eff}^*] + j \text{Im}[\varepsilon_{eff}^*] = \varepsilon_{eff} + j \frac{\sigma_{eff}}{\omega \varepsilon_o}, \quad (2.40)$$

or rewritten in terms of a conductance form as

$$\sigma_{eff}^* = \text{Re}[\sigma_{eff}^*] + j \text{Im}[\sigma_{eff}^*] = \sigma_{eff} + j \omega \varepsilon_{eff} \varepsilon_o, \quad (2.41)$$

The imaginary term ($\text{Im}[\dots]$) is known as “the loss factor” and the ration of $\frac{\text{Im}[\varepsilon_{eff}^*]}{\text{Re}[\varepsilon_{eff}^*]}$ is called “the loss tangent” (for more details see Cheng, 1991). The latter represents the power loss of the spheroid in the suspending medium. Both σ_{eff} and ε_{eff} represent the DC conductivity (S/m) and the dielectric constant of the spheroid, respectively. The ε_o is the dielectric constant of vacuum ($=8.85 \times 10^{-12} \text{ F.m}^{-1}$). A circular frequency is defined as $\omega = 2\pi f$, where f is the field frequency in Hertz and $j = \sqrt{-1}$.

According to Eqs. (2.40) and (2.41), the expressions for dielectric properties of the cytoplasm (c), membrane (m) and suspending medium (s) for the spheroidal model are given by the following:

$$\varepsilon_c^* = \varepsilon_c - j \frac{\sigma_c}{\omega \varepsilon_o} \quad \text{and} \quad \sigma_c^* = \sigma_c + j \omega \varepsilon_c \varepsilon_o, \quad (2.42)$$

$$\varepsilon_m^* = \varepsilon_m - j \frac{\sigma_m}{\omega \varepsilon_o} \quad \text{and} \quad \sigma_m^* = \sigma_m + j \omega \varepsilon_m \varepsilon_o, \quad (2.43)$$

$$\varepsilon_s^* = \varepsilon_s - j \frac{\sigma_s}{\omega \varepsilon_o} \quad \text{and} \quad \sigma_s^* = \sigma_s + j \omega \varepsilon_s \varepsilon_o. \quad (2.44)$$

Substituting Eqs. (2.42) and (2.43) into Eq. (2.34) yields

$$\varepsilon_{eff}^* = (\varepsilon_m - j \frac{\sigma_m}{\omega \varepsilon_0}) \left(\frac{(\varepsilon_m - j \frac{\sigma_m}{\omega \varepsilon_0}) + (\varepsilon_c - \varepsilon_m + j \frac{\sigma_c - \sigma_m}{\omega \varepsilon_0})(L_k + v(1-L_k))}{(\varepsilon_m - j \frac{\sigma_m}{\omega \varepsilon_0}) + (\varepsilon_c - \varepsilon_m + j \frac{\sigma_c - \sigma_m}{\omega \varepsilon_0})(L_k + (1-v))} \right), \quad (2.45)$$

where the real and imaginary parts of Eq. (2.45) are

$$\text{Re}[\varepsilon_{eff}^*] = \frac{1}{\omega \varepsilon_0} \left(\frac{(\omega^2 \varepsilon_0^2 \varepsilon_m A + \sigma_m B)(\omega \varepsilon_0 C) + \omega \varepsilon_0 D(\varepsilon_m B - \sigma_m A)}{(\omega \varepsilon_0 C)^2 + D^2} \right), \quad (2.46)$$

$$\text{Im}[\varepsilon_{eff}^*] = \frac{1}{\omega \varepsilon_0} \left(\frac{\omega^2 \varepsilon_0^2 C(\varepsilon_m B - \sigma_m A) - D(\omega^2 \varepsilon_0^2 \varepsilon_m A + \sigma_m B)}{(\omega \varepsilon_0 C)^2 + D^2} \right). \quad (2.47)$$

The constants A , B , C and D are

$$A = \varepsilon_m + \alpha (\varepsilon_c - \varepsilon_m),$$

$$B = \alpha (\sigma_m - \sigma_c) - \sigma_m,$$

$$C = \varepsilon_m + \beta b (\varepsilon_c - \varepsilon_m),$$

$$D = \beta (\sigma_m - \sigma_c) - \sigma_m,$$

and $\alpha = L_k + v(1 - L_k)$, $\beta = L_k(1 - v)$.

Plots of $\text{Re}[\varepsilon_{eff}^*]$ (Eq. 2.46) and $\text{Im}[\varepsilon_{eff}^*]$ (Eq. 2.47) as functions of electric field frequency were shown in Fig. 2.3. As described by Cheng (1991), the loss factor

calculated from $\frac{\text{Im}[\varepsilon_{eff}^*]}{\text{Re}[\varepsilon_{eff}^*]}$ was also presented in Fig. 2.3, where the peak of the loss factor is

nearly equal to the point of intersection between curves of $\text{Re}[\varepsilon_{eff}^*]$ and $\text{Im}[\varepsilon_{eff}^*]$. The

complex plane plot between $\text{Re}[\varepsilon_{eff}^*]$ and $\text{Im}[\varepsilon_{eff}^*]$, the so called “Cole-Cole plot” is shown in Fig. 2.4. Interpretations of the loss factor and the Cole-Cole plot were given in details elsewhere (Asami *et al.* 1980; Gimsa and Wachner, 1998; Asami, 2002).

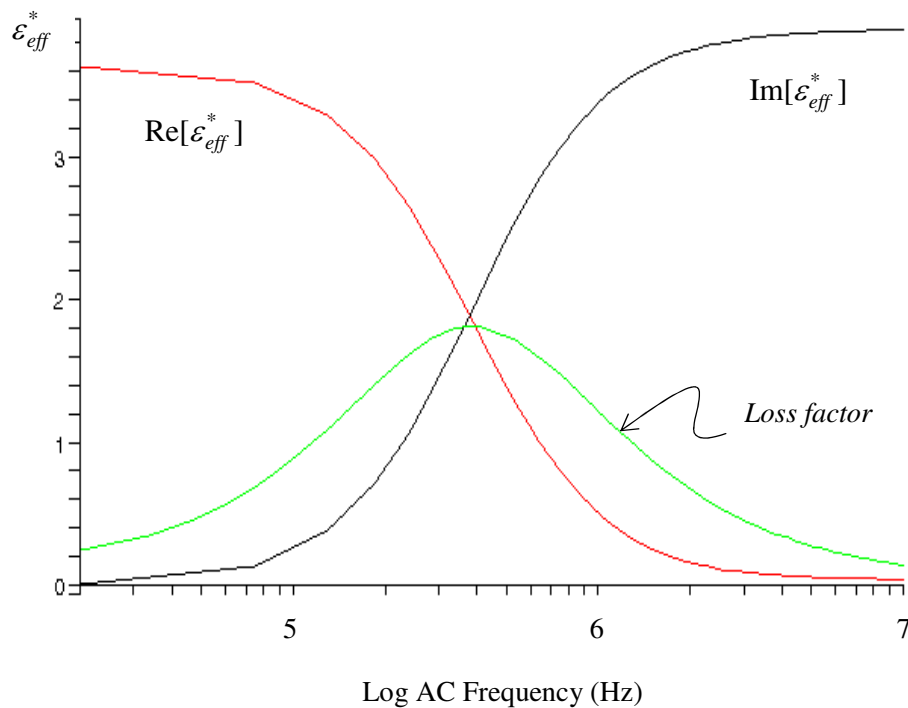


Fig. 2.3 Theoretical plots of the real and the imaginary parts of the effective complex relative permittivity of a spheroid.

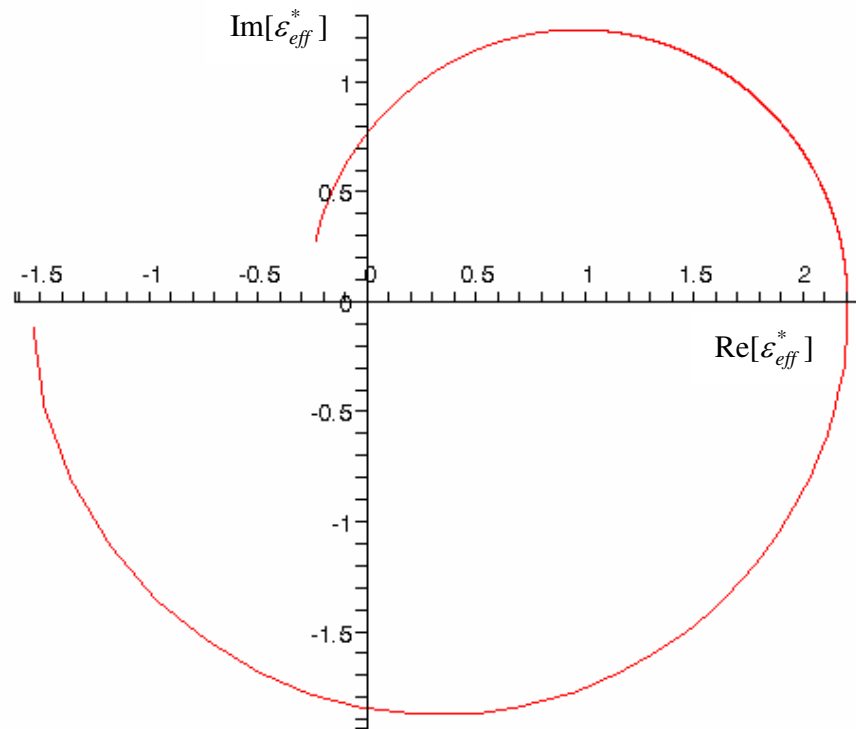


Fig. 2.4 The complex plane plot (the Cole-Cole plot) of the effective complex relative permittivity obtained from the Laplace approach.

2.2.4 The Clausius-Mossotti Factor [CMF]

In this section, the above $\text{Re}[\varepsilon_{eff}^*]$ and $\text{Im}[\varepsilon_{eff}^*]$ as in Eqs. (2.46) and (2.47) will be substituted in ε_{eff}^* (Eq. 2.40). The aim was to calculate the critical frequencies at which the DEP force (\vec{F}_{DEP}) (Eq. 1.1 in chapter 1), is zero. The DEP force is given by the

real part of the Clausius-Mossotti (Re[CMF]). Details of the calculations for [CMF] and then for Re[CMF] are as followed.

As described in Eq. 1.1 (chapter 1), Landua and Lifschitz (1985) defined [CMF] = $\frac{\varepsilon_{eff}^* - \varepsilon_s^*}{\varepsilon_s^* + (\varepsilon_{eff}^* - \varepsilon_s^*)L_k}$. For a spheroid with the volume of $V = \frac{4}{3}\pi ab^2$ (Fig. 2.1a), the value of the depolarization factor L_k when $k = x$ and y were calculated from Eqs. (2.26) and (2.27), respectively. It should be noted that the value of L_k reflects the shape of the spheroid. For example, if $q = \frac{a}{b} > 1$, the spheroid is prolate and $L_x < 1$ (calculated from Eq. 2.26). When $L_k = 1/3$, the spheroid is transformed to a sphere with radius of $a=b=c$ and the [CMF] reduces to the familiar expression of $\frac{3(\varepsilon_{eff}^* - \varepsilon_s^*)}{(\varepsilon_{eff}^* + 2\varepsilon_s^*)}$ proposed by Sauer (1985) and

Kaler and Jones (1990). Substituting the values of ε_{eff}^* (Eq. 2.45), ε_s^* (Eq. 2.44) and L_k (Eq. 2.26) into Eq. 1.1 (chapter 1). The real and the imaginary parts of the [CMF] are then expressed as

$$\text{Re[CMF]} = \left[\left(\frac{A_1 A_3 + A_2 A_4}{A_3^2 + A_4^2} \right) \right], \quad (2.48)$$

$$\text{Im[CMF]} = \left[\left(\frac{A_1 A_3 - A_2 A_4}{A_3^2 + A_4^2} \right) \right], \quad (2.49)$$

where

$$\begin{aligned} A_1 &= \text{Re}[\varepsilon_{eff}^*] - \omega\varepsilon_0\varepsilon_s, \\ A_2 &= \text{Im}[\varepsilon_{eff}^*] - \sigma_s, \\ A_3 &= \omega\varepsilon_0\varepsilon_s(1 - L_k) + \text{Re}[\varepsilon_{eff}^*]L_k, \\ A_4 &= \text{Im}[\varepsilon_{eff}^*]L_k - \sigma_s(L_k + 1), \end{aligned}$$

where $\varepsilon_0 = 8.85 \times 10^{-12} \text{ F.m}^{-1}$, $\omega = 2\pi f$ (rad.s⁻¹), f in Hertz and $\text{Re}[\varepsilon_{eff}^*]$ and the $\text{Im}[\varepsilon_{eff}^*]$ are from Eqs. (2.46) and (2.47), respectively.

Plots of both $\text{Re}[\text{CMF}]$ (Eq. 2.48) and $\text{Im}[\text{CMF}]$ (Eq. 2.49) as a function of electric field frequency are shown in Fig. 2.5. When using dielectric parameters for yeast cells (*Saccharomyces cerevisiate*) as reported by Zhou *et al.* (1996), the spectra of the real and imaginary parts of [CMF] showed the positive and negative regions of the [CMF]. Two critical values, f_λ and f_h , appear lower and higher frequency range. It is interesting that the $\text{Re}[\text{CMF}]$ does not show a plateau at the middle frequency range as appeared a spherical shell model (Mahaworasilpa *et al.* 1994; Jones 1995).

Figure 2.6 and 2.7 show the spectra of $\text{Re}[\text{CMF}]$ and $\text{Im}[\text{CMF}]$ under variations of cell geometry (a and δ) (Figs. 2.6a, 2.6b, 2.7a and 2.7b) and dielectric parameters of the cytoplasm (ε_c, σ_c) (Figs. 2.6c, 2.6d, 2.7c and 2.7d), the membrane (ε_m, σ_m) (Figs. 2.6e, 2.6f, 2.7e and 2.7f), the suspending medium (ε_s, σ_s) (Figs. 2.6g, 2.6h, 2.7g and 2.7h). As is seen from Figs. 2.6a, increasing a shifts f_λ to lower values and the peak magnitude of $\text{Re}[\text{CMF}]$ decreases. In contrast, in Fig. 2.6b, increasing δ shifts f_λ to higher values and the peak magnitude of $\text{Re}[\text{CMF}]$ increases. Figure 2.6c shows that decreasing ε_c only affects the negative $\text{Re}[\text{CMF}]$ at higher frequency range. The peak of $\text{Re}[\text{CMF}]$ shown in Fig. 2.6d is diminished when σ_c is decreased to 0.1 S.m^{-1} . Decreasing σ_c to 0.01 S.m^{-1} gives the same result as for the case of $\sigma_c = 0.1 \text{ S.m}^{-1}$ which is the optimized value to obtain the plateau spectra. It should be noted that the variation of σ_c used for Fig. 2.6d is based on reported by Zhou *et al.* (1996). In case of change in ε_m and σ_m as shown in Figs. 2.6e and 2.6f, f_λ is shifted to higher values and the peak magnitude of $\text{Re}[\text{CMF}]$ is decreased when ε_m and σ_m are reduced. The negative $\text{Re}[\text{CMF}]$ at higher frequency range as shown in Fig. 2.6g is only affected by change of ε_s which is similar to that of Fig. 2.6c, but the shifts go in opposite direction for both cases.

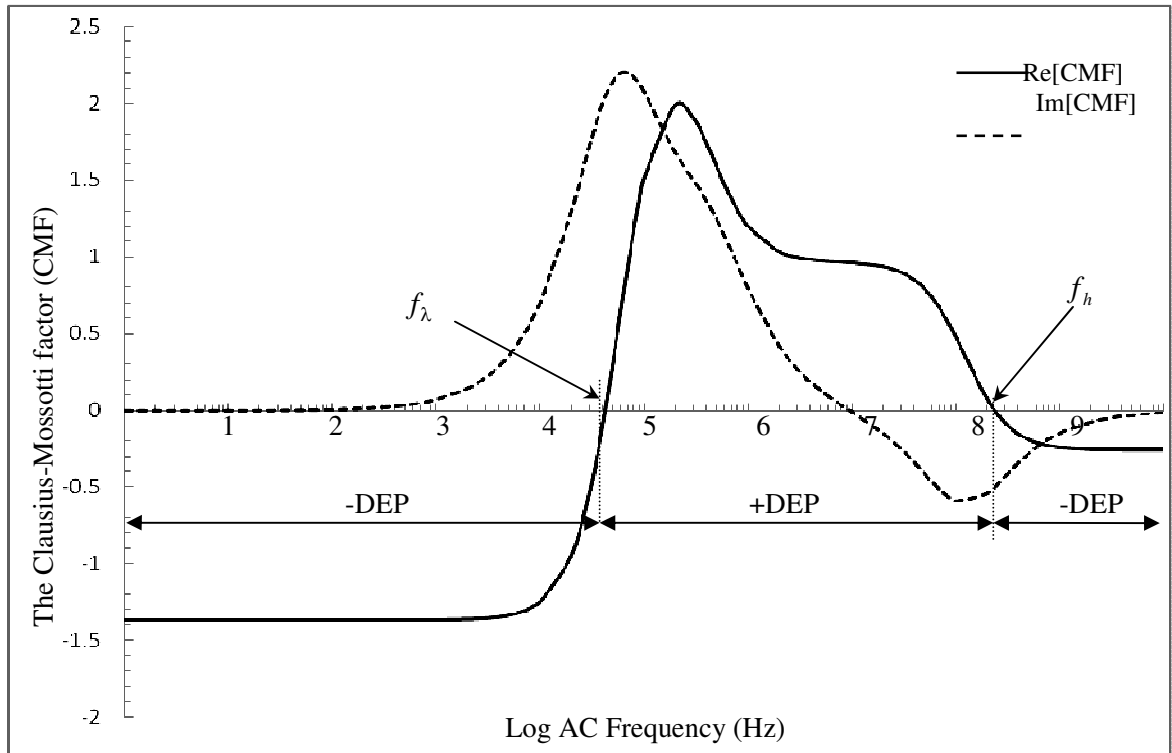
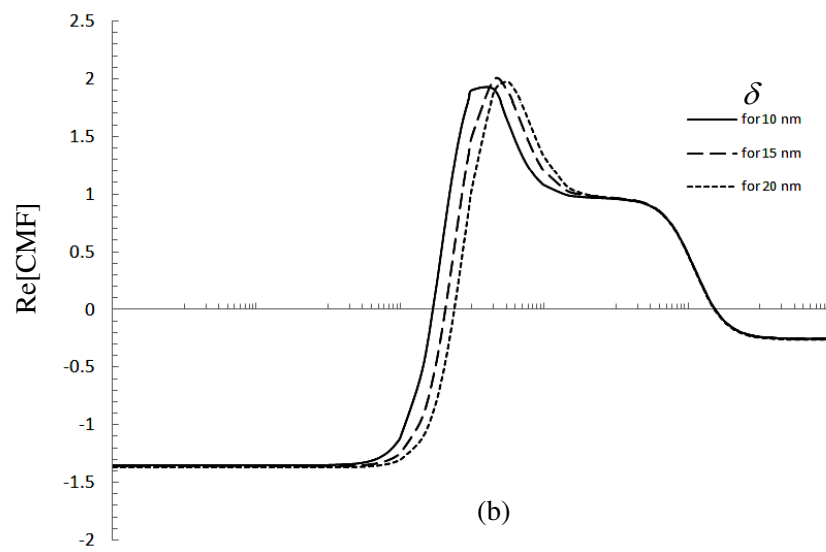
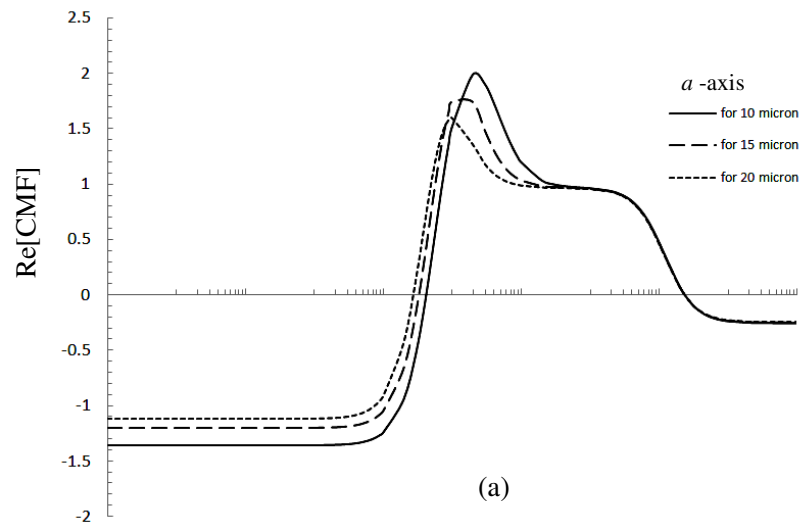


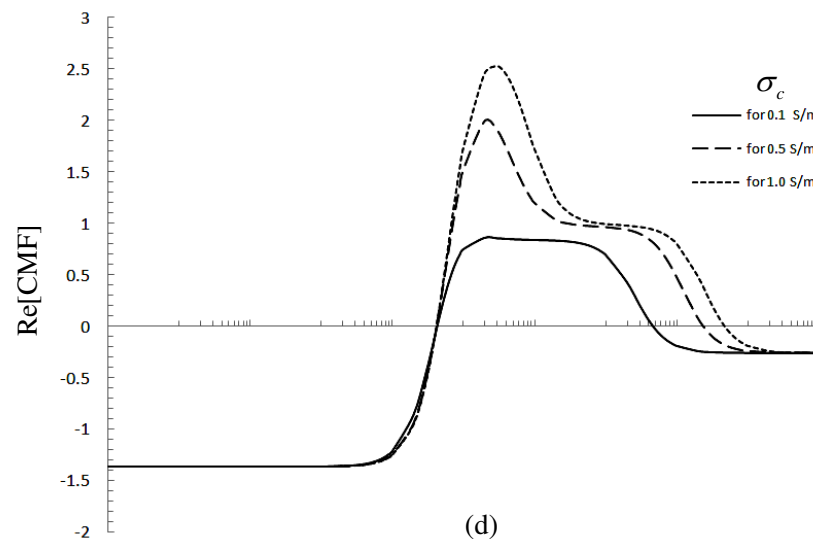
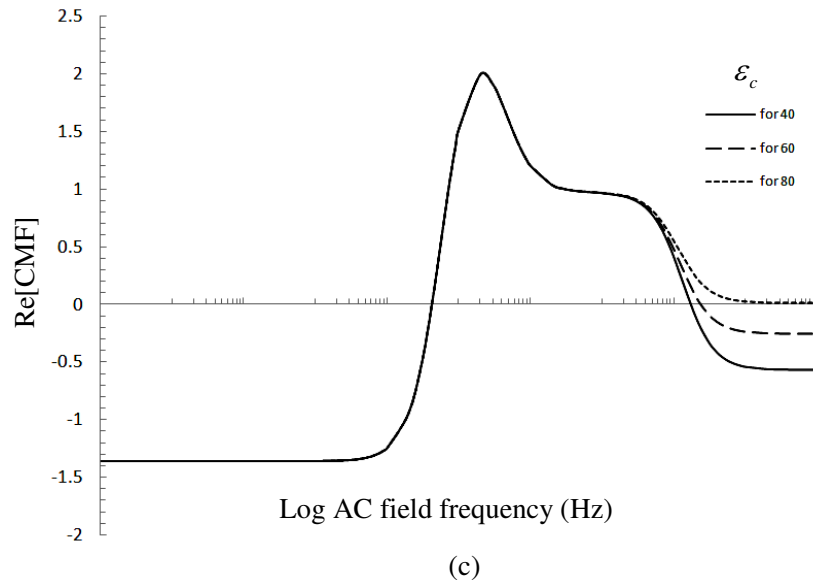
Fig. 2.5. Re[CMF] and Im[CMF] were plotted as a function of electric field frequency. Three field frequency ranges indicate the frequency regions where positive and negative DEP occur. The following parameters were employed for these plots:

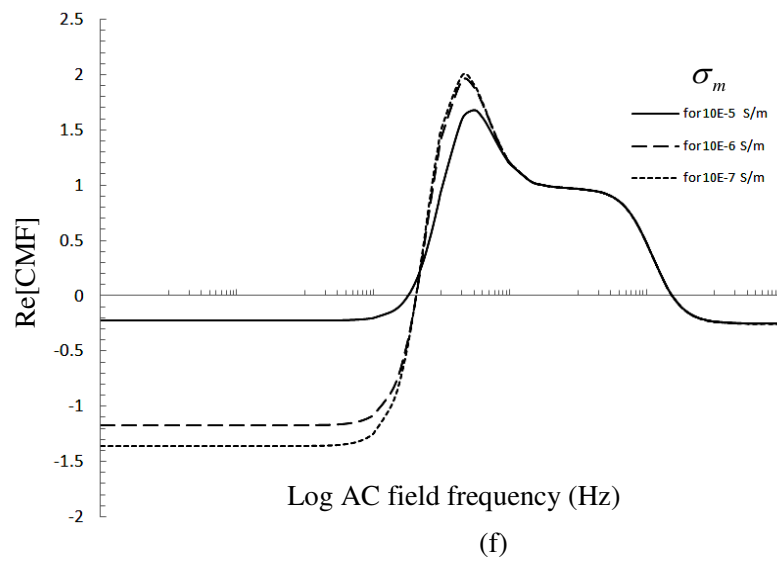
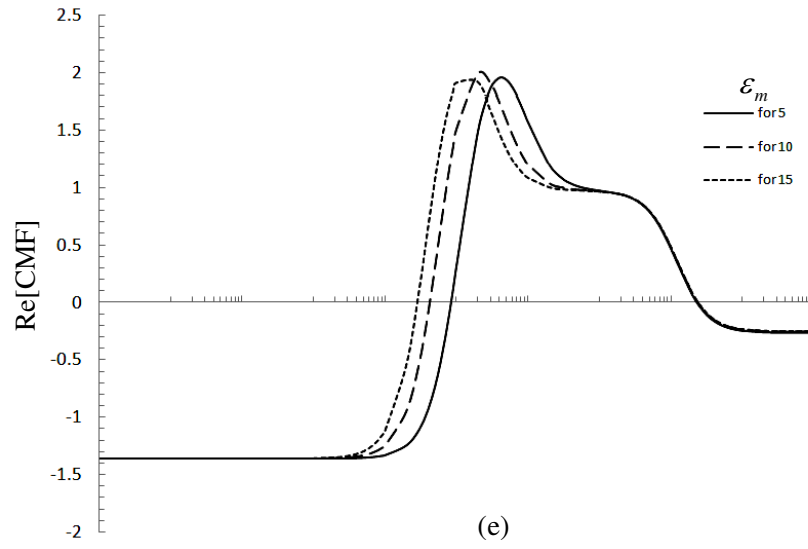
$$\sigma_c = 0.5 \text{ S.m}^{-1}, \sigma_m = 0.1 \mu\text{S.m}^{-1}, \sigma_s = 0.01 \text{ S.m}^{-1}, \varepsilon_c = 60, \varepsilon_m = 10, \varepsilon_s = 78,$$

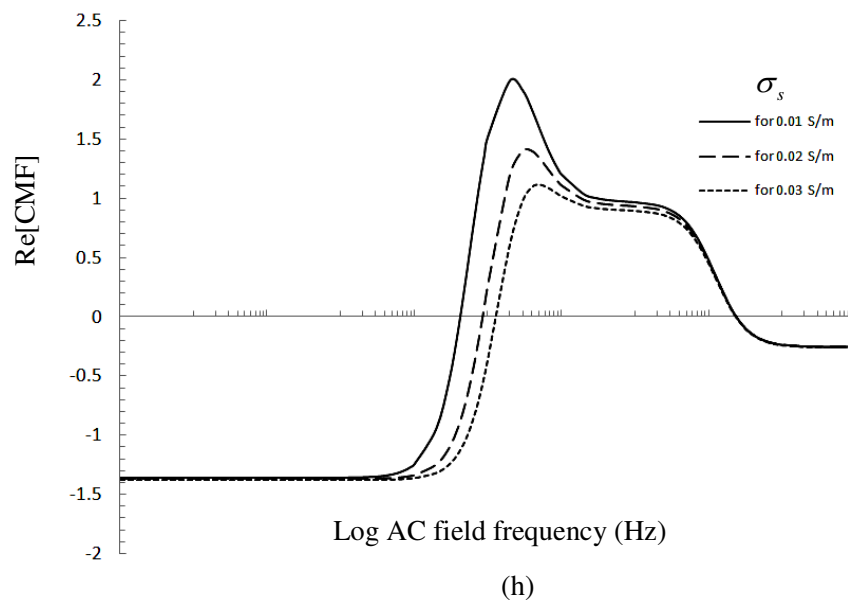
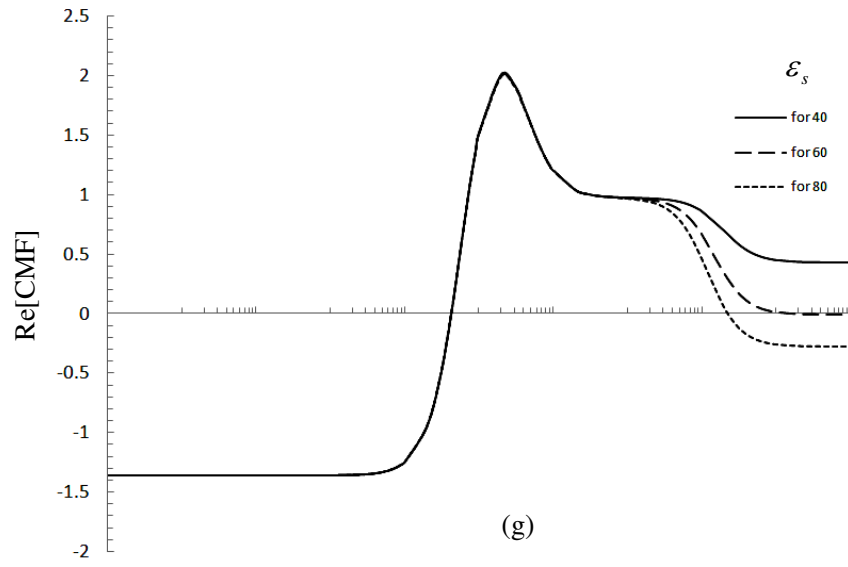
$$\delta = 15 \text{ nm and } L_x = 0.276.$$

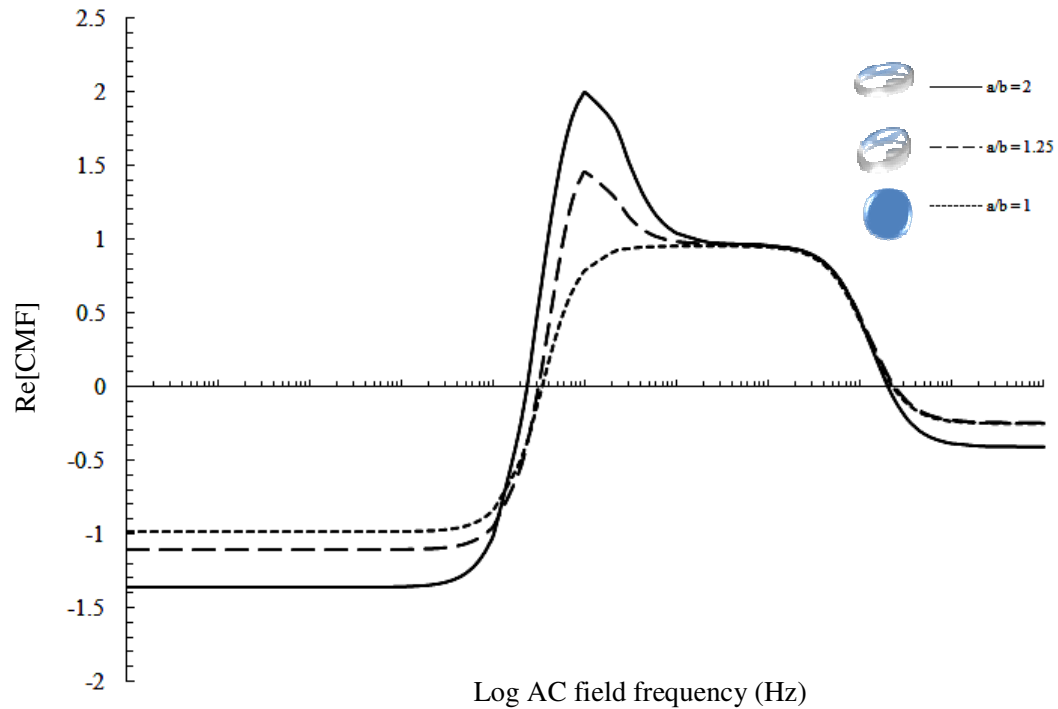
For change of σ_s shown Fig. 2.6h, the reduced peak of Re[CMF] results from increasing σ_s from 0.01 to 0.03 S.m^{-1} . It is interesting that when a spheroid is transformed into a sphere by choosing three equal semi-axes (the ratio of $a/b = 1$) (Fig. 2.6i), the peak of Re[CMF] is diminished and the curve is similar to that of a sphere (Pohl, 1978; Mahaworasilpa *et al.* 1994; Jones 1995). Plot of depolarization factor (L_k) (Eq. 2.26) as a function of a/b was shown in Fig. 2.6j.



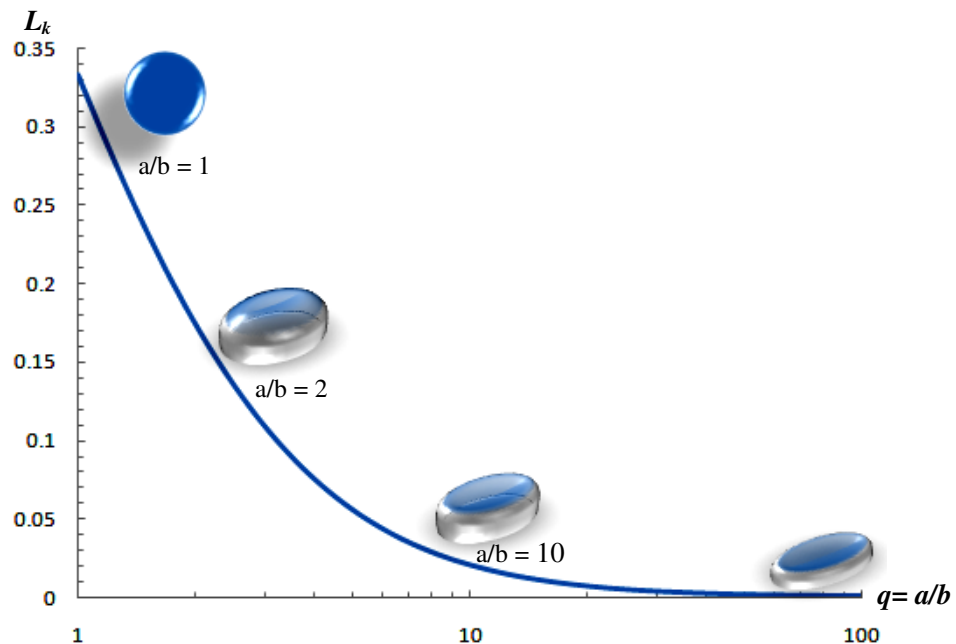






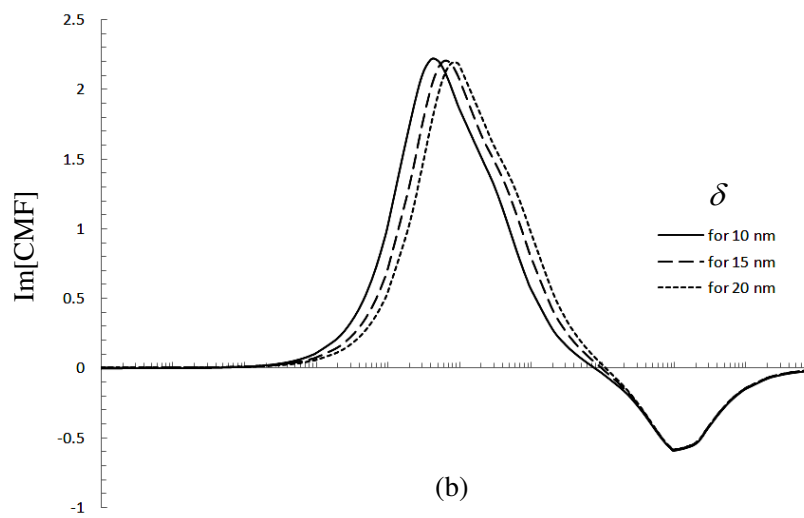
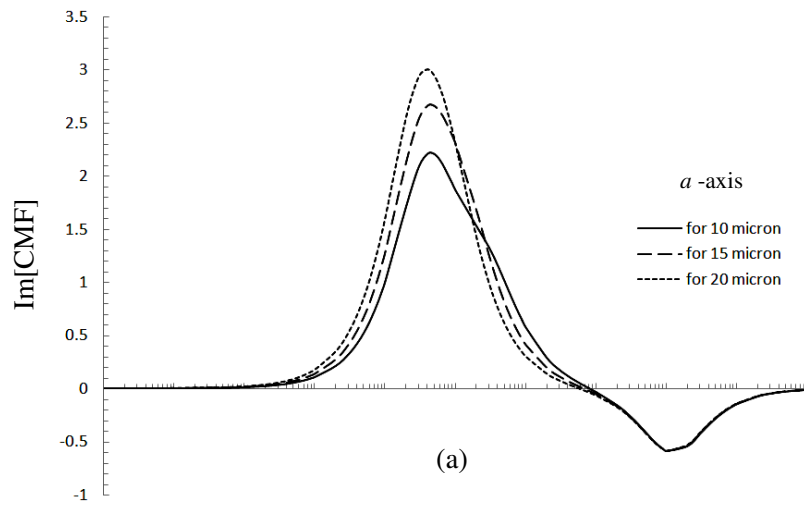


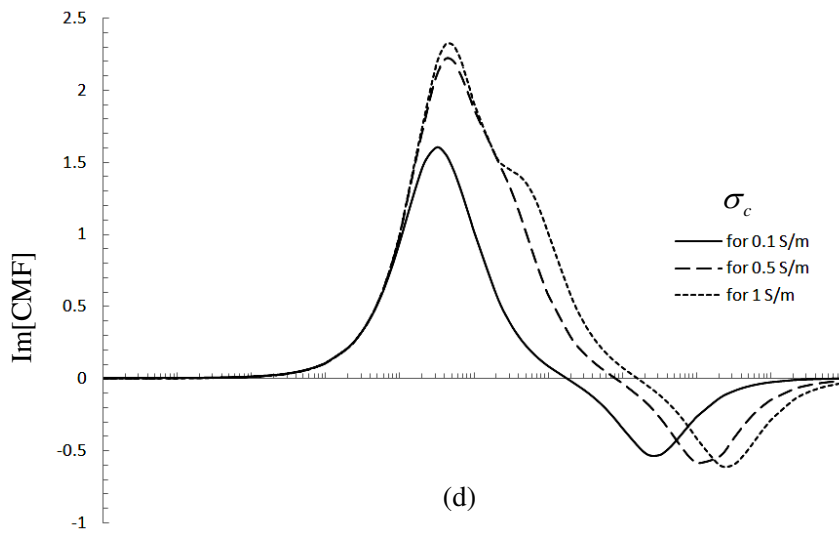
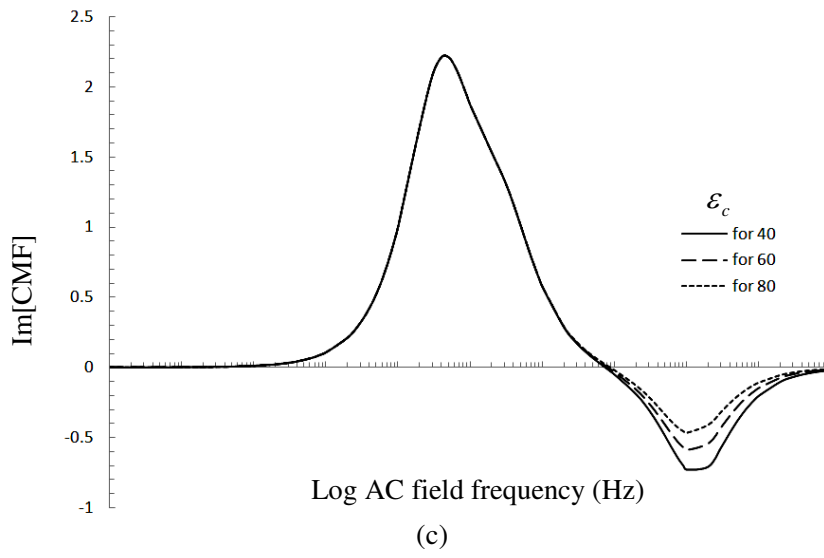
(i)

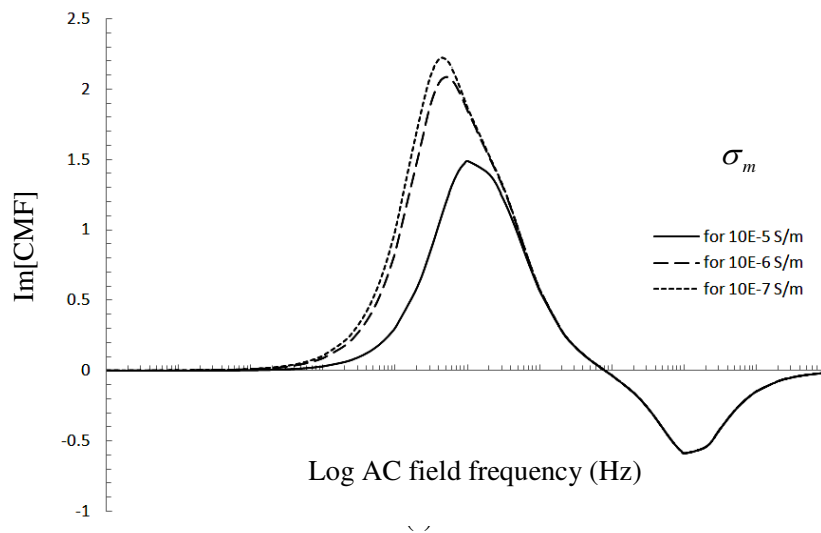
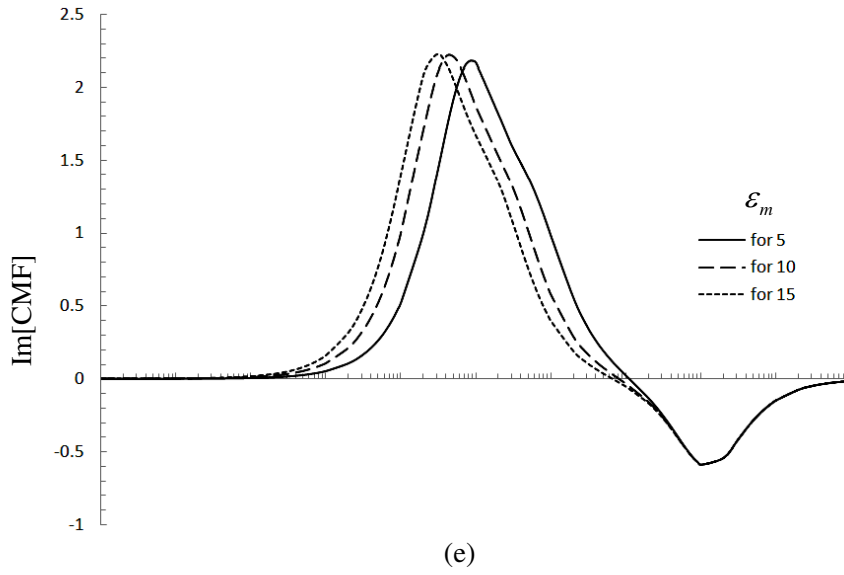


(j)

Fig.2.6 The spectra of the real part of the Clausius-Mossotti factor [CMF] are affected by changing electrical parameters as described in the model. All solid lines were plotted using the parameters as shown in Fig. 2.5.







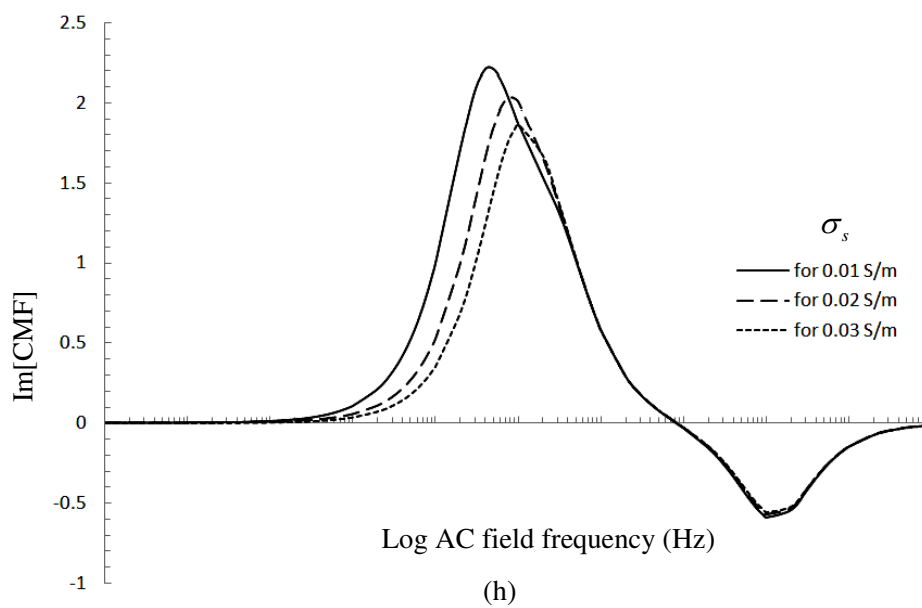
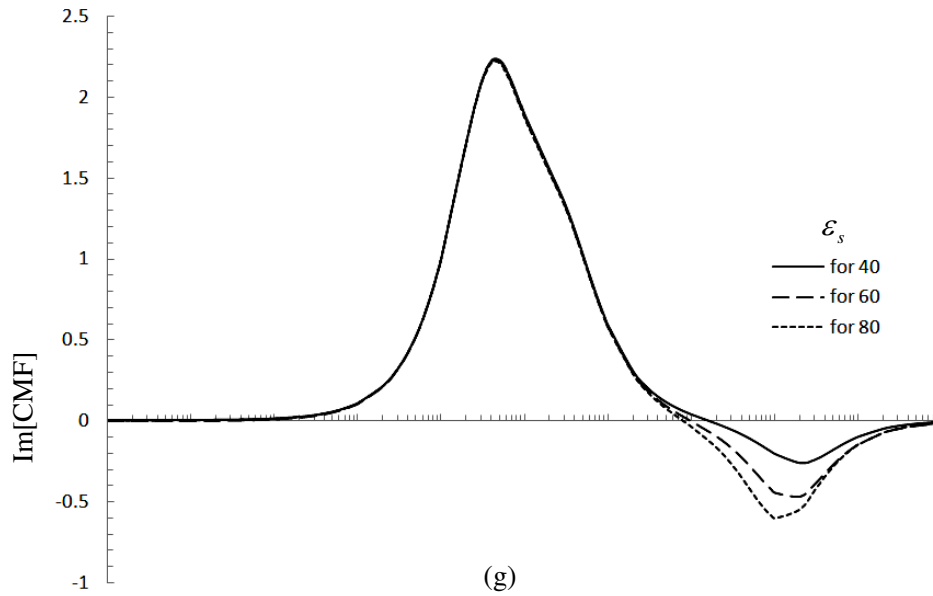


Fig.2.7 The spectra of the imaginary part of the Clausius-Mossotti factor [CMF] are affected by changing electrical parameters as described in the model. The solid lines were plotted using the parameters as shown in Fig. 2.5.

2.2.5 Two Critical Frequencies

Fig. 2.5 shows two critical frequencies where there is a transition from positive to the negative DEP. To obtain an express for these frequencies via Eq. (2.48) is quite complex. The lower (f_λ) and the higher (f_h) critical frequencies of the model can, however, be separately derived from the condition $\text{Re}[\text{CMF}]=0$ as follows.

According to dielectric dispersion as suggested by Schwan (1988), the dielectric properties of the membrane are prominent in the lower frequencies range (α, β dispersions). The complex relative permittivity for each compartment of the model (see Eqs. (2.42-2.44)) becomes

$$\varepsilon_c^* \approx -j \frac{\sigma_c}{\omega \varepsilon_o} \quad \text{and} \quad \sigma_c^* \approx \sigma_c, \quad (2.50)$$

$$\varepsilon_m^* = \varepsilon_m - j \frac{\sigma_m}{\omega \varepsilon_o} \quad \text{and} \quad \sigma_m^* = \sigma_m + j \omega \varepsilon_m \varepsilon_o, \quad (2.51)$$

$$\varepsilon_s^* \approx -j \frac{\sigma_s}{\omega \varepsilon_o} \quad \text{and} \quad \sigma_s^* \approx \sigma_s. \quad (2.52)$$

On the other hand, those of the cytoplasm are dominant in the higher frequency range providing

$$\varepsilon_c^* = \varepsilon_c - j \frac{\sigma_c}{\omega \varepsilon_o} \quad \text{and} \quad \sigma_c^* = \sigma_c + j \omega \varepsilon_c \varepsilon_o, \quad (2.53)$$

$$\varepsilon_m^* \approx \varepsilon_m \quad \text{and} \quad \sigma_m^* = 0, \quad (2.54)$$

$$\varepsilon_s^* = \varepsilon_s - j \frac{\sigma_s}{\omega \varepsilon_o} \quad \text{and} \quad \sigma_s^* = \sigma_s + j \omega \varepsilon_s \varepsilon_o. \quad (2.55)$$

Substituting Eqs. (2.50-2.52) and (2.53-2.55) to Eqs. (2.34) and (2.47) yield the angular frequency (ω) dependence of the Re[CMF] for the lower and the higher frequencies, respectively. For the lower case, the Re[CMF] is expressed as

$$\text{Re[CMF]}_{\lambda\omega} = \frac{\omega^2 Z'_1 Z'_3 + (\omega Z'_2 + \sigma_s)(\omega Z'_4 + Z'_5)}{\omega^2 Z_3'^2 + (\omega Z'_4 + Z'_5)^2}, \quad (2.56)$$

where

$$\begin{aligned} Z'_1 &= \varepsilon_0 \text{Re}[\varepsilon_{eff}^*(\lambda\omega)], \\ Z_2^* &= \varepsilon_0 \text{Im}[\varepsilon_{eff}^*(\lambda\omega)], \\ Z_3^* &= \varepsilon_0 L_k \text{Re}[\varepsilon_{eff}^*(\lambda\omega)], \\ Z_4^* &= \varepsilon_0 L_k \text{Im}[\varepsilon_{eff}^*(\lambda\omega)], \\ Z_5^* &= L_k(\sigma_s - 1), \end{aligned}$$

and

$$\text{Re}[\varepsilon_{eff}^*(\lambda\omega)] = \frac{\omega^2 Z'_6 Z'_7 + Z'_8 Z'_9}{\omega^2 Z_7'^2 + Z_9'^2}, \quad (2.57)$$

$$\text{Im}[\varepsilon_{eff}^*(\lambda\omega)] = \frac{\omega(Z'_6 Z'_9 - Z'_7 Z'_8)}{\omega^2 Z_7'^2 + Z_9'^2}, \quad (2.58)$$

where

$$\begin{aligned} Z'_6 &= \varepsilon_0[\varepsilon_m^2 + a'\varepsilon_m(\varepsilon_c - \varepsilon_m)], \\ Z_7^* &= \varepsilon_0[\varepsilon_m + b'(\varepsilon_c - \varepsilon_m)], \\ Z_8^* &= a'\varepsilon_m \sigma_c, \\ Z_9^* &= b'\sigma_c, \end{aligned}$$

$$\text{with } a' = L_k + v(1 - L_k), \quad b' = L_k(1 - v), \quad v = \left(1 - \frac{\delta}{a}\right)\left(1 - \frac{\delta}{b}\right)^2.$$

Setting Eq. (2.56) = 0 and then solving for ω , yields the functions

$$\omega_{\lambda\omega} = \frac{1}{2\varepsilon_0 Z'_6} \sqrt{-\frac{1}{L_k} (\alpha_1 - 2\sqrt{\alpha_2 + \alpha_3})}, \quad (2.59)$$

since $\omega_{\lambda\omega} = 2\pi f_\lambda$, then

$$f_\lambda = \frac{1}{4\pi\varepsilon_0 Z'_6} \sqrt{-\frac{1}{L_k} (\alpha_1 - 2\sqrt{\alpha_2 + \alpha_3})}, \quad (2.60)$$

where

$$\begin{aligned} \alpha_1 &= 2\varepsilon_0 \sigma_s Z'_7 Z'_8 (1 - 2L_k) - 2Z_7'^2 \sigma_s^2 (1 - L_k) - 2\varepsilon_0 \sigma_s Z'_6 Z'_9 (1 - 2L_k) - 2\varepsilon_0^2 L_k, \\ \alpha_2 &= \varepsilon_0^2 \sigma_s^2 (Z_7'^2 (6L_k - 1) - 2Z_6' Z_7' Z_8' Z_9') + 2\varepsilon_0^3 \sigma_s L_k Z'_6 Z'_9 (1 - 2L_k) + \\ &\quad Z_7'^4 \sigma_s^4 L_k (L_k - 2) - 2\varepsilon_0 \sigma_s^3 Z_7'^3 Z_8' (2L_k^2 + 1) + 4\varepsilon_0^3 \sigma_s Z_7' Z_8' L_k^2, \\ \alpha_3 &= 6\varepsilon_0 \sigma_s^2 L_k Z_7'^2 (Z_7' Z_8' \sigma_s - \varepsilon_0 L_k) + 8\sigma_s^2 \varepsilon_0^2 L_k Z'_6 Z_7' Z_8' Z_9' (1 - L_k) + \\ &\quad 2\varepsilon_0 \sigma_s Z_7' (Z_6' Z_7' Z_9' \sigma_s^2 - \varepsilon_0 Z_8' L_k) + 2\varepsilon_0 Z_7'^2 \sigma_s^3 Z_6' Z_9' L_k (2L_k - 3) + \\ &\quad \varepsilon_0^2 \sigma_s^2 (Z_6' Z_9')^2 L_k^2 + Z_7'^2 \sigma_s^4 + \varepsilon_0^4 L_k^2. \end{aligned}$$

A similar procedure was applied for the higher critical frequency, yielding

$$f_h = \frac{1}{4\pi\varepsilon_0 Z'_6} \sqrt{\frac{1}{L_k} (\alpha_1 + 2\sqrt{\alpha_2 + \alpha_3})}, \quad (2.61)$$

Theoretical plots of the lower and the higher critical frequencies were shown in Fig. 2.8.

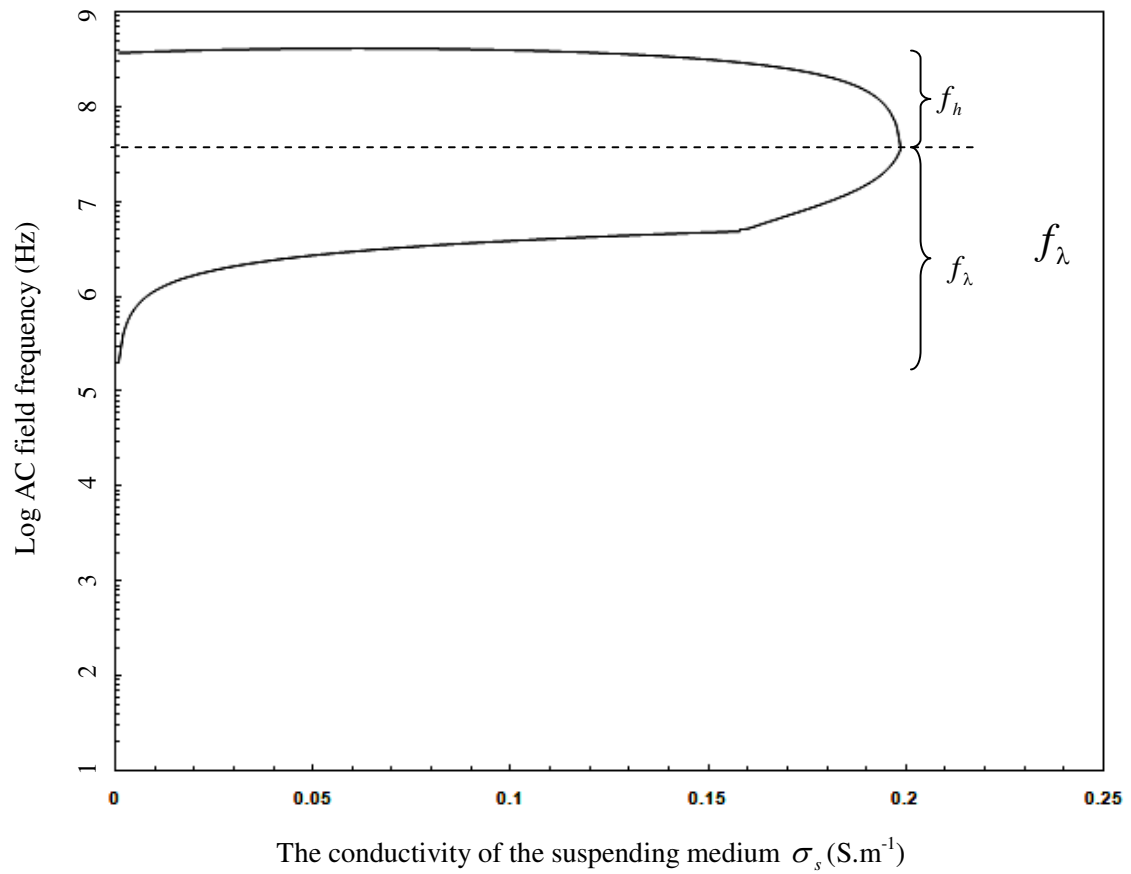


Fig. 2.8 Theoretical plot of two critical frequencies, predicted from the Laplace approach. The f_λ and f_h were plotted by using the parameters as shown in Fig. 2.5.

2.3 An Impedance Approach (RC model)

2.3.1 The Clausius-Mossotti Factor [CMF]

Gimsa and Wachner (1998) proposed a spheroidal model through an equivalent RC-circuit, using resistors (R) and capacitors (C) to represent the conductive and the capacitive properties instead of conductivities (σ) and dielectric constants (ε), respectively. Based on the model, the [CMF] was expressed in term of the specific complex impedance (Z_i^*).

An illustration of the RC-model is shown in Fig. 2.9. The conductive and capacitive properties of each compartment of the spheroid are given as:

$$\sigma_i^* = \sigma_i + j\omega\varepsilon_i\varepsilon_o \quad \text{and} \quad (2.62)$$

$$C_i^* = \varepsilon_i\varepsilon_o A / \delta. \quad (2.63)$$

Here subscripts i were used for c , m and s , henceforth for the sake of simplicity, and A denotes a specific area. The relation of σ_i^* and a specific complex impedance (Z_i^*) is given by

$$Z_i^* = (\sigma_i + j\omega\varepsilon_0\varepsilon_i)^{-1}. \quad (2.64)$$

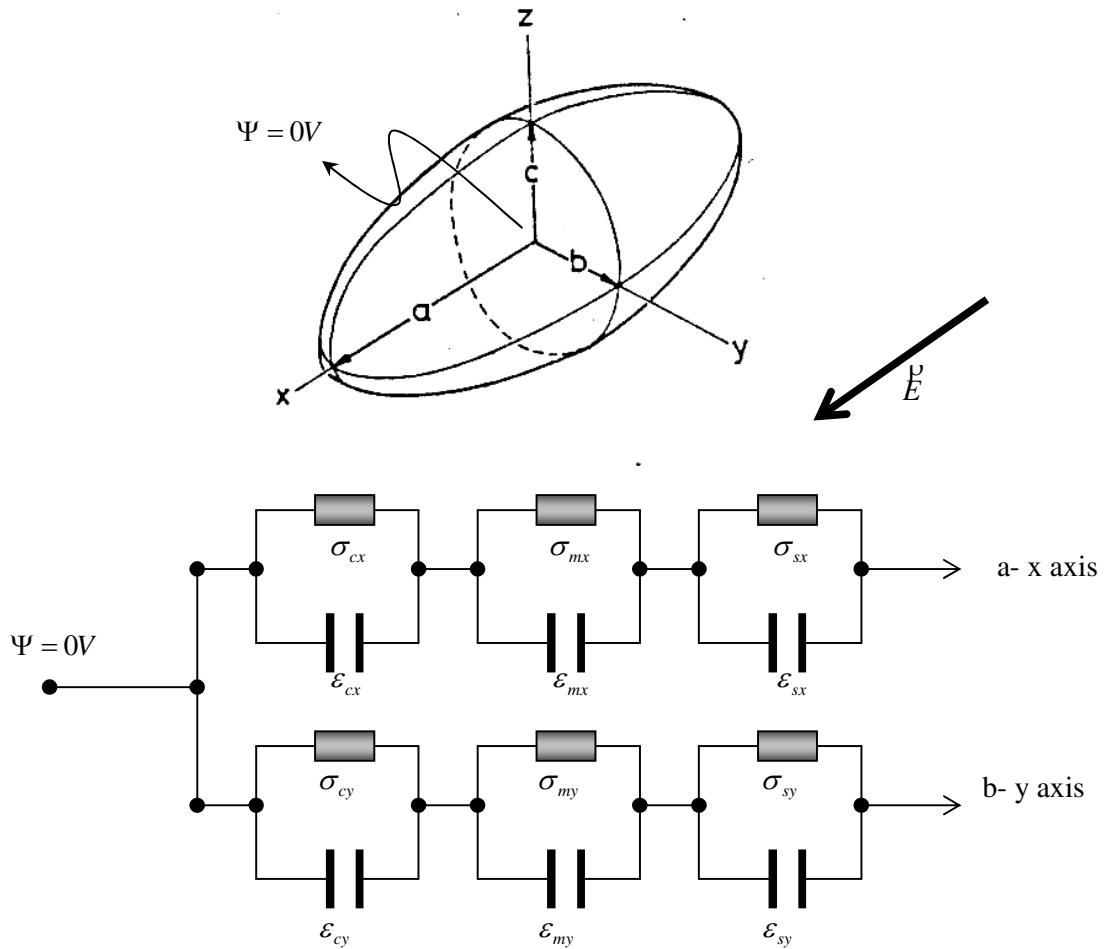


Fig. 2.9 The equivalent RC-model consists of 2 branches of the parallel of resistor-capacitor pairs.

According to Gimsa and Wachner (1998), the induced dipole moment of a homogeneous ellipsoid then could be written in form

$$\vec{\mu} = \frac{\epsilon_o \epsilon_s^* V}{L_k} \left(\frac{\psi_s^* - \psi_f^*}{\psi_s^*} \right) \vec{E}, \quad (2.65)$$

where ψ_s^* and ψ_f^* represent electrical potentials of the medium and of the cell/medium interface, respectively. Later, Gimsa and Wachner (1999) proposed the [CMF] as

$$[\text{CMF}] = \frac{1}{L_k} \left(\frac{\psi_s^* - \psi_f^*}{\psi_s^*} \right). \quad (2.66)$$

The relations between ψ_s^* and ψ_f^* with the specific complex impedance (Z_i^*) were defined as

$$\psi_s^* = \frac{Z_c^* + Z_m^*}{Z_c^* + Z_m^* + Z_s^*} \text{ and } \psi_f^* = \left[\frac{Z_c^* + Z_m^*}{(Z_c^* + Z_m^* + Z_s^*)} \right] \frac{\rho \rho}{E.f.}_{\text{inf}}, \quad (2.67)$$

where $r_{\text{inf}} = \frac{r}{1 - L_k}$ and r is the radius measured from the center of the spheroid.

Substituting Eq.(2.66) into Eq. (2.66), [CMF] along k axis can be obtained as

$$[\text{CMF}] = \frac{1}{L_k} \left[1 - \frac{Z_c^* + Z_m^*}{(Z_c^* + Z_m^* + Z_s^*)(1 - L_k)} \right], \quad (2.68)$$

Since Eq. (2.68) can be resolved along three orthogonal axes, it can be written in a matrix form as

$$[\text{CMF}] = \begin{pmatrix} \text{CMF}_x & 0 & 0 \\ 0 & \text{CMF}_y & 0 \\ 0 & 0 & \text{CMF}_z \end{pmatrix} \text{ which related with } L_k = \begin{pmatrix} L_x & 0 & 0 \\ 0 & L_y & 0 \\ 0 & 0 & L_z \end{pmatrix}. \quad (2.69)$$

Similarly, Eq. (2.64) can be resolved into three components as

$$Z_i^* = \begin{pmatrix} Z_c^* \\ Z_m^* \\ Z_s^* \end{pmatrix} = \begin{pmatrix} (\sigma_c^*)^{-1} \\ (\sigma_m^*)^{-1} \\ (\sigma_s^*)^{-1} \end{pmatrix} = \begin{pmatrix} (\sigma_c + j\omega\epsilon_o\epsilon_c)^{-1} \\ (\sigma_m + j\omega\epsilon_o\epsilon_m)^{-1} \\ (\sigma_s + j\omega\epsilon_o\epsilon_s)^{-1} \end{pmatrix}. \quad (2.70)$$

The [CMF] (Eq. 2.68) was written in matrix form and all-off diagonal terms are zero. However, in practical, the exact value of [CMF] of the remainder can not be calculated (Gimsa, 2001). Hence, only one axis should be examined. From Jones (1995), a spheroid always responds to an external electric field by aligning its longest axis i.e. x -direction (see Figs. 2.1 and 2.9) parallel to the vector field \vec{E} . Hence, only [CMF_x] was examined for the present study. For simplicity, it is reasonable to set [CMF_x]]=[CMF] for the current study presented in this thesis. This is true only if the longest axis of the spheroid is parallel to the vector field. Substituting Eqs. (2.67) and (2.70) into Eq. (2.68), it follows that

$$[\text{CMF}] = \left(\frac{(\sigma_m^* \sigma_s^* + \sigma_c^* \sigma_s^* + \sigma_c^* \sigma_m^*) L_x - \sigma_c^* \sigma_m^*}{\sigma_m^* \sigma_s^* + \sigma_c^* \sigma_s^* + \sigma_c^* \sigma_m^*} (L_x^2 - L_x) \right). \quad (2.71)$$

The RC-circuit equivalent to Eq. (2.71) is presented in Fig. 2.9. Again, solving Eq. (2.71) for the critical frequencies is not a simple task since it is complicated function. To manipulate it, the dielectric properties of the spheroid relevant at the lower frequencies must be simplified. By using the principle of dielectric dispersion proposed by Schwan (1988), the capacitive and conductive properties of the membrane are usually dominant at lower electric field frequency while that of the cytoplasm, only the capacitive properties are dominant at the higher frequency. This means that if one considers the capacitive and conductive properties from the value of Z_i^* , the capacitive term of the cytoplasm and suspending medium at the lower frequency can be neglected i.e.

$$Z_m^* = (\sigma_m + j\omega\varepsilon_0\varepsilon_m)^{-1}, \quad (2.72)$$

$$Z_c^* = (\sigma_c)^{-1}, \quad (2.73)$$

$$Z_s^* = (\sigma_s)^{-1}. \quad (2.74)$$

Substituting Eqs. (2.72), (2.73) and (2.74) into (2.71) yields the [CMF] at the lower frequencies $[\text{CMF}]_{\text{RC-Model}}^{\text{low}}$, i.e.

$$[\text{CMF}]_{\text{RC-Model}}^{\text{low}} = \frac{(\sigma_s + \sigma_c + Z_m^* \sigma_s \sigma_c - \sigma_s \alpha - \sigma_s \sigma_c \alpha Z_m^*)}{(\sigma_s + \sigma_c + Z_m^* \sigma_s \sigma_c) L_k}, \quad (2.75)$$

where $\alpha = \left(\frac{1}{1 - L_k} \right)$. Similarly, for the higher frequencies, the capacitive and conductive terms of the membrane can be neglected i.e.

$$Z_m^* = 0, \quad (2.76)$$

$$Z_c^* = (\sigma_c + j\omega\varepsilon_0\varepsilon_c)^{-1}, \quad (2.77)$$

$$Z_s^* = (\sigma_s + j\omega\varepsilon_0\varepsilon_s)^{-1}. \quad (2.78)$$

Substituting equations (2.76), (2.77) and (2.78) into equation (2.71) yields the [CMF] at the higher frequencies $[\text{CMF}]_{\text{RC-Model}}^{\text{high}}$, i.e.

$$[\text{CMF}]_{\text{RC-Model}}^{\text{high}} = \frac{(1 - \alpha)Z_c^* + Z_s^*}{(Z_c^* + Z_s^*) L_k}, \quad (2.79)$$

With these simplifications, the RC-circuit relevant for the lower and the higher frequencies are shown in Fig. 2.10a and 2.10b, respectively.

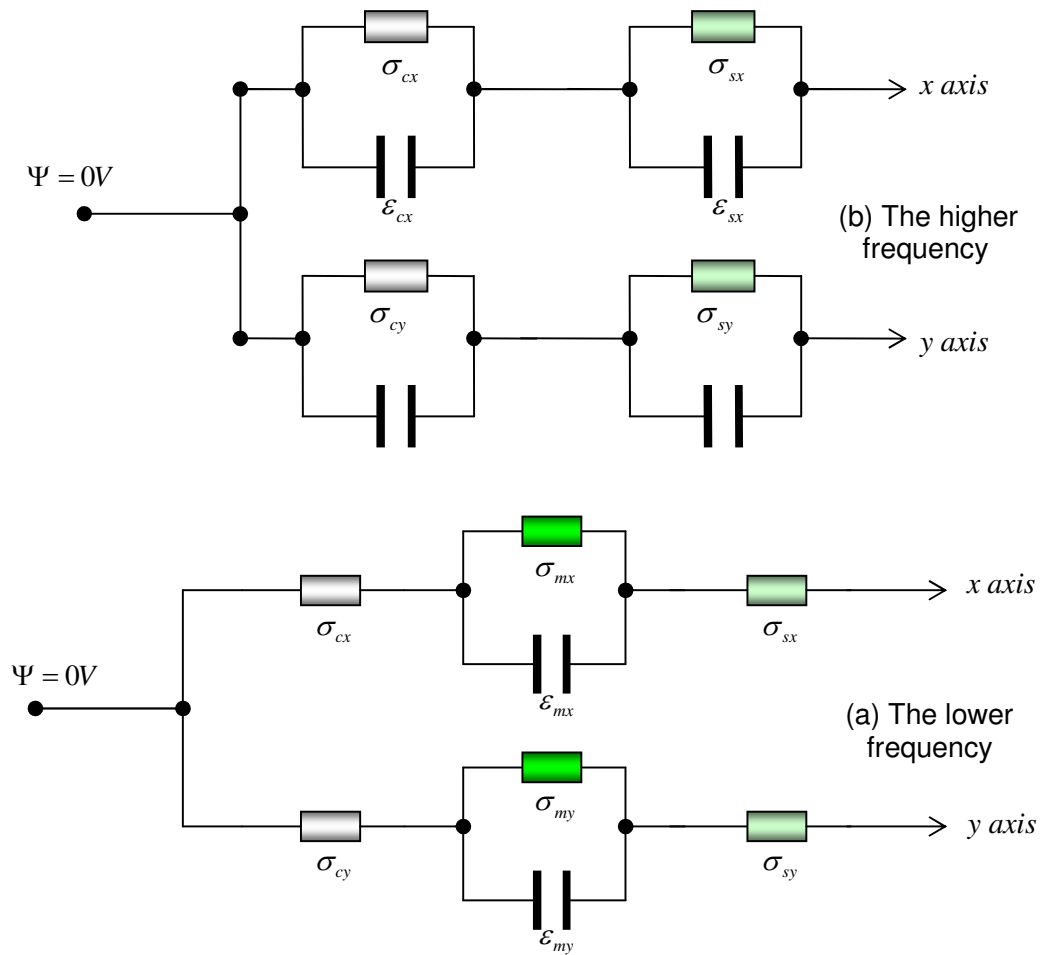


Fig. 2.10 Simplifications of two critical frequencies of the spheroidal model. Schemes for (a) a lower and (b) higher frequencies.

2.3.2 Two Critical Frequencies

To determine the lower (f_λ) and the higher (f_h) critical frequencies from the RC approach, the real parts of Eqs. (2.75) and (2.79) are set to zero. By extracting the ω from $\text{Re}[\text{CMF}]$ yields two expressions of the critical frequency that are

$$f_\lambda = -\frac{\varepsilon_o \sqrt{-E(F+G)}}{2\pi D}, \quad (2.80)$$

$$f_h = \frac{\varepsilon_o \sqrt{-AB}}{2\pi C}, \quad (2.81)$$

where

$$A = -\varepsilon_c^2 - 2\varepsilon_c \varepsilon_s + \varepsilon_c \varepsilon_s \beta + \varepsilon_s^2 \beta - \varepsilon_s^2,$$

$$B = -\sigma_c^2 + \beta \sigma_s^2 + \sigma_c \sigma_s \beta - \sigma_s^2 - 2\sigma_c \sigma_s,$$

$$C = \varepsilon_o^2 A,$$

$$D = \varepsilon_m \varepsilon_o^2 E,$$

$$E = \beta \sigma_s \sigma_c - \sigma_c^2 + \beta \sigma_s^2 - 2\sigma_c \sigma_s - \sigma_s^2,$$

$$F = 2\beta \sigma_m \sigma_c \sigma_s^2 + \sigma_c^2 \sigma_s \sigma_m \beta - 2\sigma_c \sigma_s \sigma_m^2 - \sigma_c^2 \sigma_s^2 - 2\sigma_c \sigma_m \sigma_s^2 - \sigma_m^2 \sigma_s^2),$$

$$G = \beta(\sigma_m^2 \sigma_s^2 + \sigma_c^2 \sigma_s^2 + \sigma_c \sigma_s \sigma_m^2) - \sigma_c^2 \sigma_m^2 - 2\sigma_s \sigma_m \sigma_c^2.$$

Theoretical plots of two theoretical critical frequencies are shown in Fig. 2.11. The effects of dielectric parameters on both f_λ and f_h are shown in Fig. 2.12. Variations of dielectric properties of the cytoplasm (σ_c and ε_c) and membrane (σ_m and ε_m) are based on dielectric values shown in Fig. 2.5. As is seen in Fig. 2.12a, increasing σ_c leads to the-

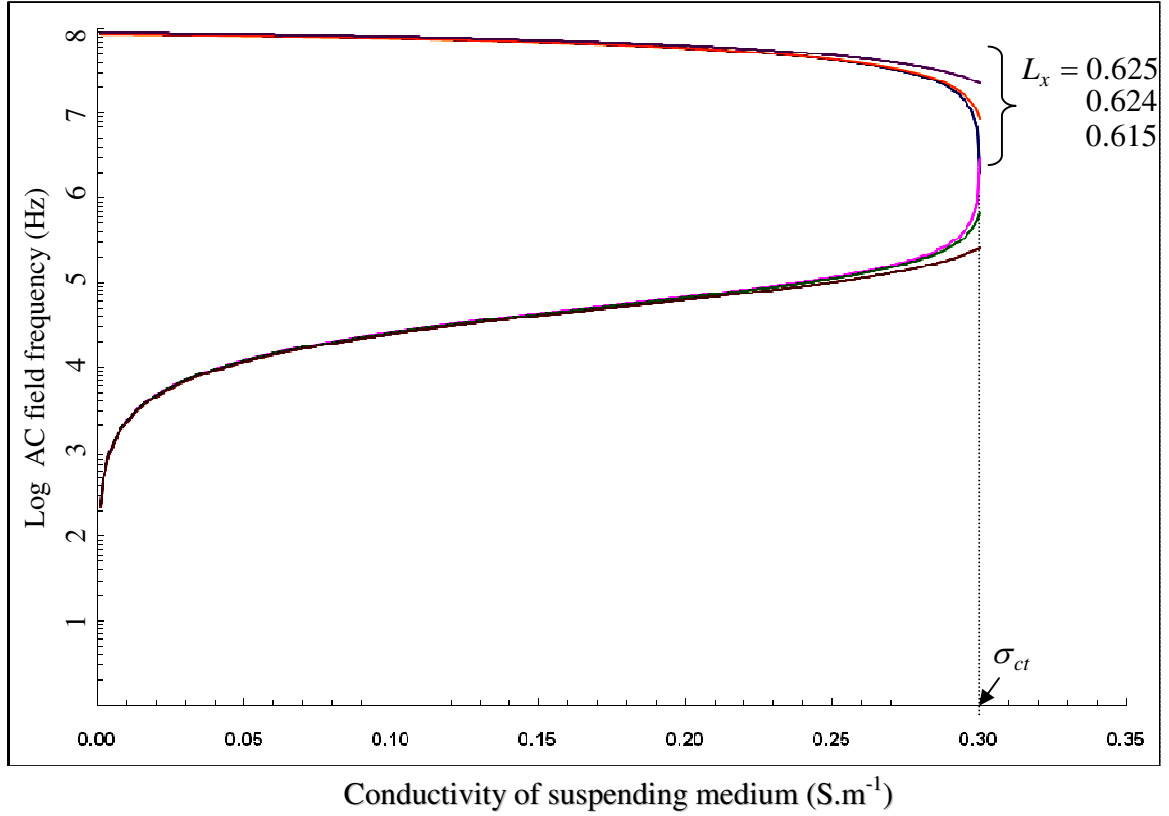


Fig. 2.11. Theoretical plots of two critical frequencies for the lower (f_λ) and the higher (f_h) as a function of depolarizations factor (L_k). After adjusting the L_k value properly, the tips of two curves are jointed together. The following parameters were employed for these

$$\text{plots: } \sigma_c = 0.5 \text{ S.m}^{-1}, \sigma_m = 0.1 \mu\text{S.m}^{-1}, \sigma_s = 0.01 \text{ S.m}^{-1}$$

$$, \varepsilon_c = 60, \varepsilon_m = 10, \varepsilon_s = 78 \text{ and } \delta = 15 \text{ nm} .$$

convergence of f_λ and f_h to join at the critical conductivity of the medium (σ_{ct}). From Fig. 2.12b, variation of σ_m in range of $10^{-7} - 10^{-4} \text{ S.m}^{-1}$ affects f_λ particularly at lower σ_s . When ε_c is decreased as shown in Fig. 2.12c, f_h is shifted to lower frequencies. Change of ε_m affects only f_λ as shown in Fig. 2.12d.

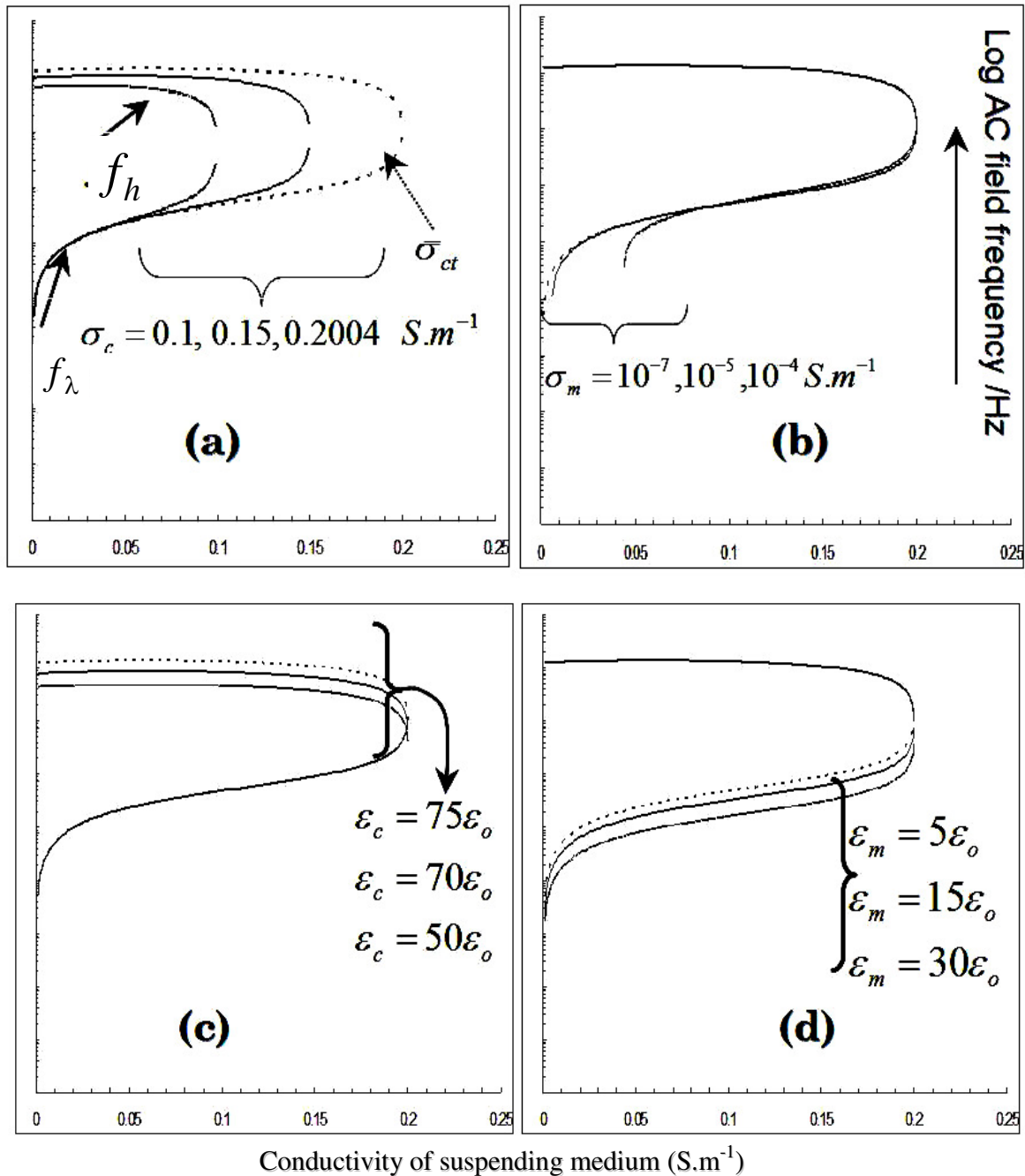


Fig. 2.12. Theoretical plots show the lower (f_λ) and the higher (f_h) critical frequency as a function of medium conductivity (σ_s). Effects of changes in σ_c , σ_m , ϵ_c and ϵ_m is shown in (a) (b) (c) and (d), respectively.

2.3.3 The Critical Conductivity

The critical conductivity is the value at which $f_\lambda = f_h$. Equating Eqs. (2.80) and (2.81) then

$$\sigma_{ct} = \frac{\sigma_c(2-\beta)}{2(\beta-1)}, \quad (2.82)$$

where $\beta = \frac{1}{(1-L_k)}$.

Equations (2.80) to (2.82) allow one to vary σ_s at arbitrary low values so that f_λ and f_h can be obtained. When the σ_s reaches σ_{ct} , the two frequencies merge at the zero DEP force. Note that the derived σ_{ct} is a constant function and solely depends on σ_c and L_k . At the critical value, $\sigma_{ct} = \sigma_c$ and $\beta = \frac{4}{3}$.

2.4 Discussions and Conclusions

The present study shows that the spectrum of $\text{Re}[\text{CMF}]$ of the spheroid possessing the single peak is different from that of the sphere, viz. there is no-peak for $\text{Re}[\text{CMF}]$ of the spherical model (Pohl, 1978; Mahaworasilpa *et al.*, 1994; Jones, 1995). The single peak may be the identity of the single shelled spheroidal model. As seen from Laplace approach, it is difficult to derive the two critical frequencies because of the complex nature of the effective permittivity of the spheroid ($\varepsilon_{eff}^*(k)$) and the fact that the $\text{Re}[\text{CMF}]$ is a complicated function of many parameters. For the impedance approach, it

was easier to obtain an expression for the two critical frequencies since [CMF] can be defined in term of the effective complex impedance which can be written in a compact form. For experimental studies in which the two critical frequencies are determined, a computer program such as Excel (Microsoft Office 2007) and Maple software (version 9.01) were employed to relate the numerical value of two critical frequencies as a function of the conductivity of the suspending medium (σ_s). The values of σ_s used for the present study were directly obtained from measurements. The key equations for the computations on microcomputer are summarized in Table 2.1.

References

1. Asami K. and Irimajiri A. 1984. Dielectric analysis of mitochondria isolated from rat liver II. Intact mitochondria as simulated by a double shell model. *Biochim Biophys Acta* **778**: 570-578.
2. Asami K., Hanai T. and Koizumi N. 1980. Dielectric approach to suspensions of ellipsoidal particles covered with a shell in particular reference to biological cells. *Jpn. J. Appl Phys* **19**: 359-365.
3. Asami K. 2002. Characterization of biological cells by dielectric spectroscopy. *Non-Crystal Solids* **305**: 268-277.
4. Cheng D. K. 1991. Field and wave electromagnetics. Addison-Wesley publishing company, 341-343.
5. Coster H. G. L. and Chilcott T. 2002. Electric field effects in proteins in membranes. *Bioelectrochemistry* **56**: 141-146.

6. Gimsa J., Marszalek P., Loewe U. and Tsong T. 1991. Dielectrophoresis and electrorotation of neurospora slime and murine myeloma cells. *Biophys J* **60**:749-760.
7. Gimsa J. and Wachner D. 1998. A unified resistor-capacitor model for impedance, dielectrophoresis, electrorotation and induced transmembrane potential. *Biophysical J* **75**: 1107-1116.
8. Gimsa J. and Wachner D. 1999. A polarization model overcoming the geometric restrictions of the Laplace solution for spheroidal cells: Obtaining new equations for field-induced forces and transmembrane potential. *Biophysical J* **77**: 1316-1326.
9. Gimsa J. 2001. A comprehensive approach to electro-orientation, electrodeformation, dielectrophoresis, and electrorotation of ellipsoidal particles and biological cells. *Bioelectrochemistry J.* 54: 23-31.
10. Irimajiri A., Hanai T. and Inouye A. 1979. *J.Theor.Biol.* 78: 251-269.
11. Jones T. B. 1995. *Electromechanics of Particles*. Cambridge University Press, Cambridge, pp 2.
12. Jones T. B. 2003. Basic theory of dielectrophoresis and electrorotation, *IEEE Engineering in medicine and biology magazine*, Nov/Dec 2003: 33-42.
13. Lippert S. and Gimsa J. 2002. High resolution measurements of dielectric cell properties by a combination of AC-electrokinetic effects. In: *2nd International Workshop on Biological effects of EMFs at Rhodes Greece*. 7-11 October, pp 830-836.

14. Mahaworasilpa T., Coster H. G. L. and George E. P. 1994. Force on biological cells due to applied (AC) electric fields. I. Dielectrophoresis. *Biochim Biophys Acta* **1193**: 118-126.
15. Pohl H. A. 1978. Dielectrophoresis: The Behaviour of Neutral Matter in Non-Uniform Electric Fields. Cambridge University Press, Cambridge, pp 6.
16. Schwan H. P. 1988. Dielectric spectroscopy and electro-rotation of biological cells. *J Ferroelectrics* **86**: 205-223.
17. Scher L. D. 1968. Dielectrophoresis in lossy dielectric media. *Nature* **220**: 695-696.
18. Watanabe M., Toshinobu S. and Irimajiri A. 1991. Dielectric behavior of the frog lens in the 100Hz to 500 MHz range: Simulation with an allocated ellipsoidal-shells model. *Biophys J* **59**:139-149.

TABLE 2.1
Summary of the key equations derived in the present study for the computations.

Laplace Approach	Impedance Approach
<p>The Clausius-Mossotti factor :</p> $[\text{CMF}] = \frac{(\varepsilon_{eff}^*(k) - \varepsilon_s^*)}{\varepsilon_s^* + (\varepsilon_{eff}^*(k) - \varepsilon_s^*)L_k} \quad k=x, y, z$	<p>The Clausius-Mossotti factor :</p> $\text{CMF}_k = \frac{1}{L_k} \left[1 - \frac{Z_c^* + Z_m^*}{(Z_c^* + Z_m^* + Z_s^*)(1 - L_k)} \right], \quad k=x, y, z$
<p>The effective complex relative permittivity:</p> $\varepsilon_{eff}^*(k) = \varepsilon_m^* \left[\frac{\varepsilon_m^* + (\varepsilon_c^* - \varepsilon_m^*)L_k + v(\varepsilon_c^* - \varepsilon_m^*)(1 - L_k)}{\varepsilon_m^* + (\varepsilon_c^* - \varepsilon_m^*)L_k - v(\varepsilon_c^* - \varepsilon_m^*)L_k} \right], \quad k=x, y, z$	<p>The effective complex impedance:</p> $Z_i^* = \begin{pmatrix} Z_c^* \\ Z_m^* \\ Z_s^* \end{pmatrix} = \begin{pmatrix} (\sigma_c^*)^{-1} \\ (\sigma_m^*)^{-1} \\ (\sigma_s^*)^{-1} \end{pmatrix} = \begin{pmatrix} (\sigma_c + j\omega\varepsilon_o\varepsilon_c)^{-1} \\ (\sigma_m + j\omega\varepsilon_o\varepsilon_m)^{-1} \\ (\sigma_s + j\omega\varepsilon_o\varepsilon_s)^{-1} \end{pmatrix}$
<p>Depolarization factor L_k (In case of the spheroid is prolate, i.e. $a > b = c$):</p> $L_x = \left(\frac{-1}{q^2 - 1} \right) + \left(\frac{q}{(q^2 - 1)^{3/2}} \right) \ln(q + (q^2 - 1)^{1/2}),$ $L_y = L_z = \frac{1 - L_x}{2}, \quad q = \frac{a}{b} > 1 .$ <p style="text-align: right;">To be continued</p>	<p>Depolarization factor L_k (In case of the spheroid is prolate, i.e. $a > b = c$):</p> $L_x = \left(\frac{-1}{q^2 - 1} \right) + \left(\frac{q}{(q^2 - 1)^{3/2}} \right) \ln(q + (q^2 - 1)^{1/2}),$ $L_y = L_z = \frac{1 - L_x}{2}, \quad q = \frac{a}{b} > 1 .$ <p style="text-align: right;">To be continued</p>

Complex permittivity:

$$\varepsilon_c^* = \varepsilon_c - j \frac{\sigma_c}{\omega \varepsilon_o} \quad \text{and} \quad \sigma_c^* = \sigma_c + j \omega \varepsilon_c \varepsilon_o,$$

$$\varepsilon_m^* = \varepsilon_m - j \frac{\sigma_m}{\omega \varepsilon_o} \quad \text{and} \quad \sigma_m^* = \sigma_m + j \omega \varepsilon_m \varepsilon_o,$$

$$\varepsilon_s^* = \varepsilon_s - j \frac{\sigma_s}{\omega \varepsilon_o} \quad \text{and} \quad \sigma_s^* = \sigma_s + j \omega \varepsilon_s \varepsilon_o.$$

where $j = \sqrt{-1}$ and $\varepsilon_o = 8.85 \times 10^{-12} \text{ F.m}^{-1}$.

Two Critical Frequencies:

$$f_\lambda = \frac{1}{4\pi \varepsilon_o Z'_6} \sqrt{-\frac{1}{L_k} (\alpha_1 - 2\sqrt{\alpha_2 + \alpha_3})} \quad \text{and}$$

$$f_h = \frac{1}{4\pi \varepsilon_o Z'_6} \sqrt{\frac{1}{L_k} (\alpha_1 + 2\sqrt{\alpha_2 + \alpha_3})}, \quad \text{where}$$

$$\alpha_1 = 2\varepsilon_o \sigma_s Z'_7 Z'_8 (1 - 2L_k) - 2Z_7'^2 \sigma_s^2 (1 - L_k) - 2\varepsilon_o \sigma_s Z'_6 Z'_9 (1 - 2L_k) - 2\varepsilon_o^2 L_k$$

$$\alpha_2 = \varepsilon_o^2 \sigma_s^2 (Z_7'^2 (6L_k - 1) - 2Z_6' Z_7' Z_8' Z_9') + 2\varepsilon_o^3 \sigma_s L_k Z_6' Z_9' (1 - 2L_k) + Z_7'^4 \sigma_s^4 L_k (L_k - 2) - 2\varepsilon_o \sigma_s^3 Z_7'^3 Z_8' (2L_k^2 + 1) + 4\varepsilon_o^3 \sigma_s Z_7' Z_8' L_k^2,$$

$$\alpha_3 = 6\varepsilon_o \sigma_s^2 L_k Z_7'^2 (Z_7' Z_8' \sigma_s - \varepsilon_o L_k) + 8\sigma_s^2 \varepsilon_o^2 L_k Z_6' Z_7' Z_8' Z_9' (1 - L_k) + 2\varepsilon_o \sigma_s Z_7' (Z_6' Z_7' Z_9' \sigma_s^2 - \varepsilon_o Z_8' L_k) + 2\varepsilon_o Z_7'^2 \sigma_s^3 Z_6' Z_9' L_k (2L_k - 3) + \varepsilon_o^2 \sigma_s^2 (Z_6' Z_9')^2 L_k^2 + Z_7'^2 \sigma_s^4 + \varepsilon_o^4 L_k^2$$

To be continued

Complex impedance:

$$Z_c^* = (\sigma_c + j \omega \varepsilon_o \varepsilon_c)^{-1},$$

$$Z_m^* = (\sigma_m + j \omega \varepsilon_o \varepsilon_m)^{-1},$$

$$Z_s^* = (\sigma_s + j \omega \varepsilon_o \varepsilon_s)^{-1}.$$

where $j = \sqrt{-1}$ and $\varepsilon_o = 8.85 \times 10^{-12} \text{ F.m}^{-1}$.

Two Critical Frequencies:

$$f_\lambda = -\frac{\varepsilon_o \sqrt{-E(F+G)}}{2\pi D} \quad \text{and} \quad f_h = \frac{\varepsilon_o \sqrt{-AB}}{2\pi C}, \quad \text{where}$$

$$A = -\varepsilon_c^2 - 2\varepsilon_c \varepsilon_s + \varepsilon_c \varepsilon_s \beta + \varepsilon_s^2 \beta - \varepsilon_s^2,$$

$$B = -\sigma_c^2 + \beta \sigma_s^2 + \sigma_c \sigma_s \beta - \sigma_s^2 - 2\sigma_c \sigma_s,$$

$$C = \varepsilon_o^2 A,$$

$$D = \varepsilon_m \varepsilon_o^2 E,$$

$$E = \beta \sigma_s \sigma_c - \sigma_c^2 + \beta \sigma_s^2 - 2\sigma_c \sigma_s - \sigma_s^2,$$

$$F = 2\beta \sigma_m \sigma_c \sigma_s^2 + \sigma_c^2 \sigma_s \sigma_m \beta - 2\sigma_c \sigma_s \sigma_m^2 - \sigma_c^2 \sigma_s^2 - 2\sigma_c \sigma_m \sigma_s^2 - \sigma_m^2 \sigma_s^2,$$

$$G = \beta (\sigma_m^2 \sigma_s^2 + \sigma_c^2 \sigma_s^2 + \sigma_c \sigma_s \sigma_m^2) - \sigma_c^2 \sigma_m^2 - 2\sigma_s \sigma_m \sigma_c^2.$$

To be continued

with

$$Z'_1 = \varepsilon_0 \operatorname{Re}[\varepsilon_{eff}^*(\lambda\omega)],$$

$$Z_2^* = \varepsilon_0 \operatorname{Im}[\varepsilon_{eff}^*(\lambda\omega)],$$

$$Z_3^* = \varepsilon_0 L_k \operatorname{Re}[\varepsilon_{eff}^*(\lambda\omega)],$$

$$Z_4^* = \varepsilon_0 L_k \operatorname{Im}[\varepsilon_{eff}^*(\lambda\omega)],$$

$$Z_5^* = L_k (\sigma_s - 1),$$

and

$$\operatorname{Re}[\varepsilon_{eff}^*(\lambda\omega)] = \frac{\omega^2 Z'_6 Z'_7 + Z'_8 Z'_9}{\omega^2 Z_7'^2 + Z_9'^2},$$

$$\operatorname{Im}[\varepsilon_{eff}^*(\lambda\omega)] = \frac{\omega(Z'_6 Z'_9 - Z'_7 Z'_8)}{\omega^2 Z_7'^2 + Z_9'^2},$$

where

$$Z'_6 = \varepsilon_0 [\varepsilon_m^2 + a' \varepsilon_m (\varepsilon_c - \varepsilon_m)],$$

$$Z_7^* = \varepsilon_0 [\varepsilon_m + b' (\varepsilon_c - \varepsilon_m)],$$

$$Z_8^* = a' \varepsilon_m \sigma_c,$$

$$Z_9^* = b' \sigma_c,$$

$$\text{with } a' = L_k + v(1 - L_k), \quad b' = L_k(1 - v), \quad v = \left(1 - \frac{\delta}{a}\right) \left(1 - \frac{\delta}{b}\right)^2.$$

The Critical Conductivity:

$$\sigma_{ct} = \frac{\sigma_c(2 - \beta)}{2(\beta - 1)},$$

$$\text{where } \beta = \frac{1}{(1 - L_k)}.$$

CHAPTER 3

THEORETICAL APPROACH FOR DIELECTROPHORETIC VELOCITY AND FORCES RELATION

3.1 Introduction

Last chapter, the sensitivity of each dielectric parameter of a single shell spheroidal model has been pointed out, and it affects the spectrum of $\text{Re}[\text{CMF}]$. Since the spheroid in travelling electric field is the first time presented in this study, this chapter will relate the $\text{Re}[\text{CMF}]$ and $\text{Im}[\text{CMF}]$ to forces acting on the spheroid.

Previously, Wang *et al.* (1995) proposed that an induced spherical cell in travelling electric field could be translated either toward the tips of the electrode or along the electrode track of a parallel array of an interdigitated electrode. This results from two orthogonal forces of the conventional dielectrophoretic force ($\overset{\text{P}}{F}_{cDEP}$) and travelling wave dielectrophoretic force ($\overset{\text{P}}{F}_{twDEP}$) which are a function of the real ($\text{Re}[\text{CMF}]$) and the imaginary part ($\text{Im}[\text{CMF}]$) of the Clausius-Mossotti factor [CMF]. This principle is applied for an analysis of translations of a spheroidal cell in traveling electric field (Fig. 3.1). When appropriate signals are applied to the electrodes as the sequence as shown in the figure, the direction of the two force indicates the direction of cell movements, whether the forces are positive, negative or zero. For the present study, this is the first time to analyze the function of both forces acting on a spheroid. Theoretical analysis of a relation between $\overset{\text{P}}{F}_{cDEP}$ and $\overset{\text{P}}{F}_{twDEP}$ was provided to obtain cell velocities.

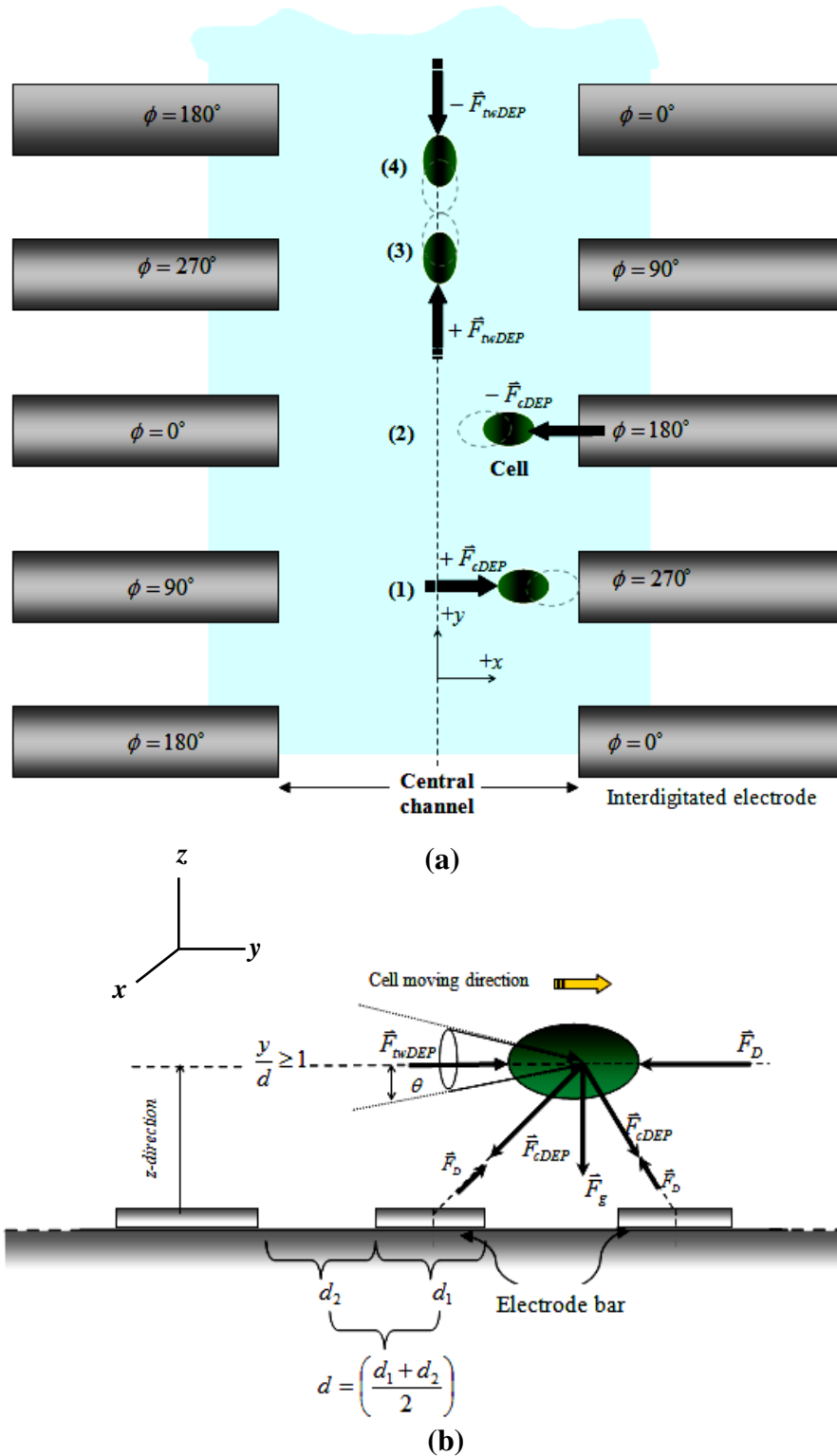


Fig. 3.1 Two orthogonal forces acting on the cells are presented in (a) top view (x - y plane) and (b) side view. The \vec{F}_{cDEP} directs the cell toward the tip of the electrode (1) or repelled from the tip (2) where the electric field strengths are larger or smaller, respectively. The travelling wave dielectrophoretic force (\vec{F}_{twDEP}) directs the cell toward the regions where the electrical phase is smaller (3) or larger (4). Noted that, the shape factor $K' = 1.05$ and $\eta = 1.20 \times 10^{-5} (\text{N.s.m}^{-2})$ was used for the calculation.

3.2 Co-Relation between the Conventional DEP and twDEP Forces

As was seen in Eq. 1.1, the time-average dielectrophoretic force (\overline{F}_t) acting on a dielectric particle in a non-uniform sinusoidal electric field $\underline{E}_k(t)$ can be written in form

$$\overline{F}_t = \sum_{k=x,y,z} \left(\mu_{eff(x)}(t) \frac{\partial E_k(t)}{\partial x} + \mu_{eff(y)}(t) \frac{\partial E_k(t)}{\partial y} + \mu_{eff(z)}(t) \frac{\partial E_k(t)}{\partial z} \right) \hat{a}_k \quad (3.1)$$

where \hat{a}_k ($k = x, y, z$) are unit vectors in Cartesian co-ordinate frame, $\underline{E}_k(t) = \sum_{k=x,y,z} E_k \cos(\omega t + \phi_k) \hat{a}_k$ and the effective dipole moment ($\mu_{eff(k)}$). The value of an electrical phase of the electric field (ϕ_k) was taken into account corresponding with k axis. For a spheroid of volume $\frac{4}{3} \pi ab^2$, the dipole moment in vector form can be written as:

$$\mu_{eff(k)}(t) = \sum_{k=x,y,z} \frac{4}{3} \pi ab^2 \varepsilon_0 \varepsilon_s E_k(t) \begin{pmatrix} \cos(\omega t + \phi_k) \text{Re[CMF]} \\ -\sin(\omega t + \phi_k) \text{Im[CMF]} \end{pmatrix} \hat{a}_k. \quad (3.2)$$

Substituting Eq. (3.2) into (3.1) gives

$$\overline{F}_t = \sum_{k=x,y,z} \frac{4}{3} \pi ab^2 \varepsilon_0 \varepsilon_s \left(\begin{array}{l} \text{Re[CMF]} \frac{\partial (E_x^2 + E_y^2 + E_z^2)}{2 \partial k} + \\ \text{Im[CMF]} \left(E_x^2 \frac{\partial \phi_x}{\partial k} + E_y^2 \frac{\partial \phi_y}{\partial k} + E_z^2 \frac{\partial \phi_z}{\partial k} \right) \end{array} \right) \hat{a}_k, \quad (3.3)$$

which can be re-arranged as

$$\bar{F}_t = \frac{2}{3} \pi a b^2 \varepsilon_0 \varepsilon_s \left[\text{Re}[\text{CMF}] \bar{\nabla} E^2 + \text{Im}[\text{CMF}] \begin{pmatrix} E_x^2 \bar{\nabla} \phi_x + \\ E_y^2 \bar{\nabla} \phi_y + \\ E_z^2 \bar{\nabla} \phi_z \end{pmatrix} \right] = \bar{F}_{cDEP} + \bar{F}_{twDEP}, \quad (3.4)$$

where $\text{Re}[\text{CMF}]$ and $\text{Im}[\text{CMF}]$ were presented in Eqs. (2.48) and (2.49), respectively, and E^2 represents of the square of electric field strength (in root mean square value). Three orthogonal components of E^2 are presented by E_x^2 , E_y^2 and E_z^2 (see Figs. 3.2). The factor $\bar{\nabla} \phi_x$, $\bar{\nabla} \phi_y$ and $\bar{\nabla} \phi_z$ are electrical phases along x , y and z components, respectively. To compute the electric field gradient ($\bar{\nabla} E^2$), the electric field strength (E) and its three components (E_x, E_y, E_z) were simulated through the finite elements analysis computer software, *Quick Field*TM version 5.5. Simulation with the software in the AC conduction mode was used with the phase sequence as shown in Figs. 3.2. Numerical values of the field strengths between two close positions are computed in sequence to obtain the exact value of the electric field gradient ($\bar{\nabla} E^2$).

As is seen from Eq. (3.4), the time-average dielectrophoretic force (\bar{F}_t) of the spheroid is the summation of the conventional dielectrophoretic force (\bar{F}_{cDEP}) (the first term in the bracket) and travelling wave dielectrophoretic force (\bar{F}_{twDEP}) (the second term). The \bar{F}_{cDEP} attracts the spheroid to the tip of the electrode while the \bar{F}_{twDEP} pushes spheroids along the track. The magnitude of the \bar{F}_{cDEP} depends on both $\text{Re}[\text{CMF}]$ and ∇E^2 while the force direction depends on whether $\text{Re}[\text{CMF}] > 0$ or $\text{Re}[\text{CMF}] < 0$. For travelling wave dielectrophoresis, the $\text{Im}[\text{CMF}]$ and $\bar{\nabla} \phi_k$ influence the magnitude and direction of the \bar{F}_{twDEP} , respectively. It should be noted that \bar{F}_{twDEP} force directs the spheroid towards the regions where the phase of the field component are larger (for $\text{Im}[\text{CMF}] > 0$) or smaller (for $\text{Im}[\text{CMF}] < 0$). Both forces are not synchronized as shown in Fig. 3.3.

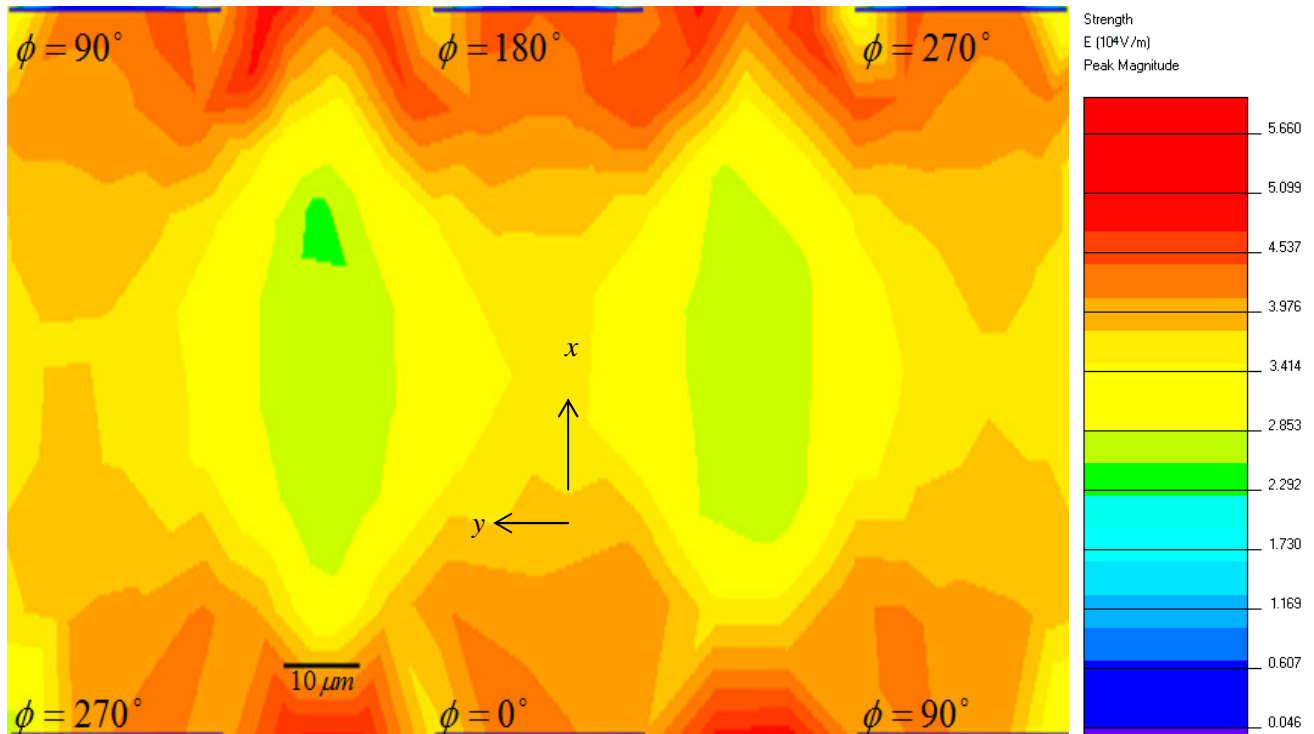


Fig.3.2 Electric field strengths generated from the interdigitated electrode were calculated from the *Quick Field*TM program. The contour was plotted using the signal amplitude of 2.83 V (rms), the electric field frequency $f = 1\text{MHz}$, the conductivity of the suspending medium $\sigma_s = 0.01\text{S.m}^{-1}$. The maximum value of electric field gradient $\nabla E^2 = 3.3 \times 10^9 \text{V}^2.\text{m}^{-3}$ locates near the tip of the electrode.

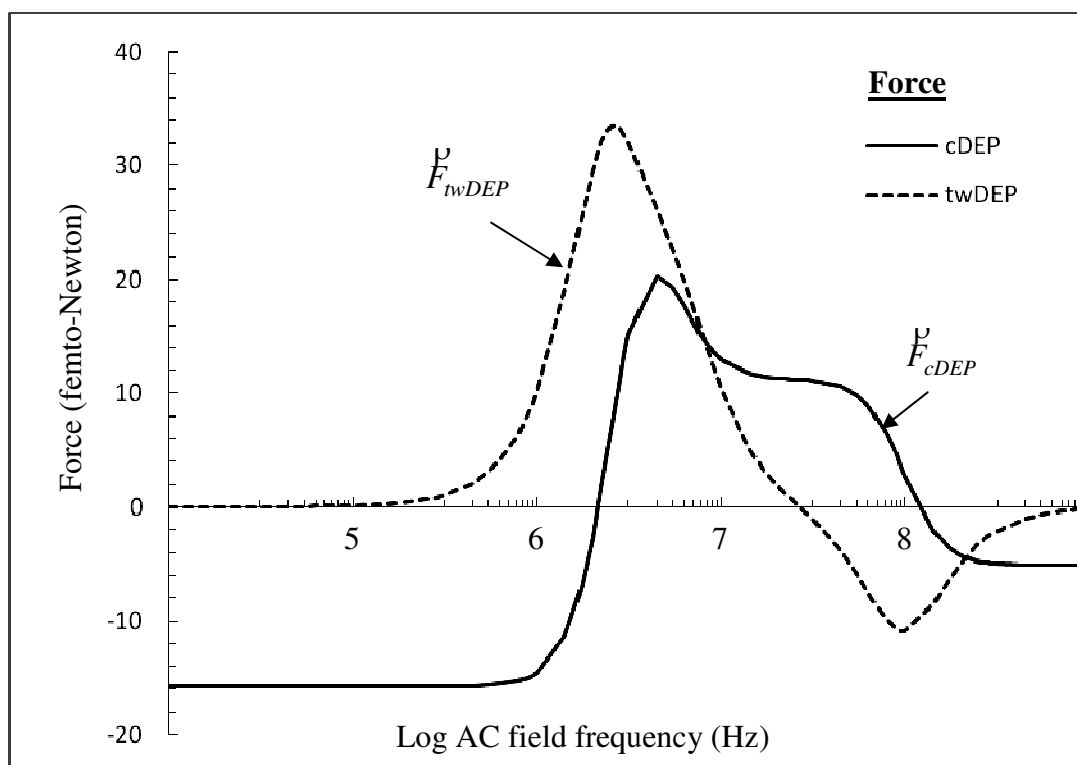


Fig. 3.3 Plots of dielectrophoretic and travelling wave dielectrophoretic forces acting on a spheroid. The following parameters were employed for these plots:

$$\sigma_c = 0.37 \text{ S.m}^{-1}, \sigma_m = 0.17 \mu\text{S.m}^{-1}, \sigma_s = 0.01 \text{ S.m}^{-1}, \varepsilon_c = 480, \varepsilon_m = 8, \varepsilon_s = 78$$

$$\delta = 13 \text{ nm and } L_x = 0.276.$$

3.3 Dielectrophoretic Velocity

As mentioned in section 3.2, two orthogonal forces of the conventional dielectrophoretic force (\vec{F}_{cDEP}) and travelling wave dielectrophoretic force (\vec{F}_{twDEP}) direct a spheroid to the tip of the electrode and along the central channel, respectively. A forces diagram acting on the spheroid being levitated above the electrode in the viscous medium with a viscosity η is shown in Fig. 3.1b. Evaluation of the translational speed of the spheroid was made through the Newton's first law of motion. Since the thickness of the electrode is too small compared to cell size, to simplify the mathematical analysis, cell translations were restricted only in xy -plane (see Fig. 3.1b) where the gravitational force (\vec{F}_g) acting on the spheroid can be neglected. The drag force for the spheroid (Happel and Brenner, 1983) is now given by

$$\vec{F}_D = 6\pi\eta\vec{v}aK'\hat{a}_k \quad (3.5)$$

where η is a viscosity of the suspending medium and K' is a shape factor as

$$K' = \frac{\frac{4}{3}(\gamma^2 - 1)}{\frac{(2\gamma^2 - 1)}{(\gamma^2 - 1)^{1/2}} \ln[\gamma + (\gamma^2 - 1)^{1/2}] - \gamma}, \quad \gamma = \frac{b}{a}. \quad (3.6)$$

In case of a constant velocity, $\text{Im}[\text{CMF}] = 0$ and $\text{Re}[\text{CMF}] \neq 0$, Eq. (3.4) becomes

$$\vec{F}_{cDEP} = -\vec{F}_D, \quad (3.7)$$

and if $\text{Re}[\text{CMF}] = 0$ and $\text{Im}[\text{CMF}] \neq 0$, then

$$\vec{F}_{twDEP} = -\vec{F}_D. \quad (3.8)$$

Substituting the first and the second terms of Eq. (3.4) into Eqs. (3.7) and (3.8), respectively, yields the translational speeds for dielectrophoresis and travelling wave dielectrophoresis as the following

$$\mathbf{v}_{cDEP}^p = \frac{\varepsilon_0 \varepsilon_s b^2 \operatorname{Re}[\operatorname{CMF}] \nabla E^2}{9\eta K'} \hat{a}_{\pm x}, \quad (3.9)$$

and

$$\mathbf{v}_{twDEP}^p = \frac{\varepsilon_0 \varepsilon_s b^2 \operatorname{Im}[\operatorname{CMF}] \sum_{i=x,y,z} (E_i^2 \nabla \phi_i)}{9\eta K'} \hat{a}_{\pm z}, \quad (3.10)$$

where $\hat{a}_{\pm x}$ and $\hat{a}_{\pm y}$ are the unit vector along x and y directions, respectively (see the coordinate in Fig. 3.1). It is clear that the direction of \mathbf{v}_{cDEP}^p and \mathbf{v}_{twDEP}^p depend on a sign of the $\operatorname{Re}[\operatorname{CMF}]$ and $\operatorname{Im}[\operatorname{CMF}]$, respectively. Both velocities are functions of the dielectric properties and they are frequency dependent. The values of $\operatorname{Re}[\operatorname{CMF}]$ and $\operatorname{Im}[\operatorname{CMF}]$ can be directly calculated from Eqs.(2.48) and (2.49), respectively. In the case of the spheroid undergoes positive dielectrophoresis, two critical frequencies (f_λ and f_h) can be determined (see also section 2.3.2 in chapter 2). Theoretical plots of dielectrophoretic velocity (\mathbf{v}_{cDEP}^p) as a function of electric field frequency is shown in Fig. 3.4. Comparison of \mathbf{v}_{cDEP}^p as simulated from the spheroidal to the spherical model is presented in Fig. 3.5. Since the frequency dependence of \mathbf{v}_{cDEP}^p is solely depended on the $\operatorname{Re}[\operatorname{CMF}]$, the effects of the dielectric parameters on \mathbf{v}_{cDEP}^p are thus similar to that of $\operatorname{Re}[\operatorname{CMF}]$ presented in Fig. 2.6 (Figs. 2.6).

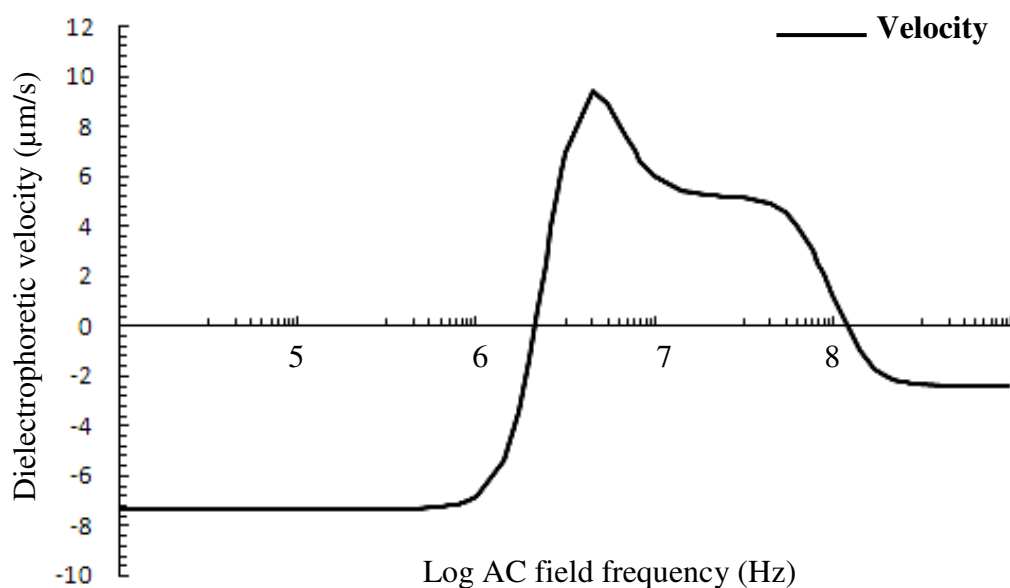


Fig. 3.4 Theoretical plots of the dielectrophoretic velocity of spheroid as a function of electric field frequencies during dielectrophoresis (solid line). The parameters used for these plots are the same as for Fig. 3.2.

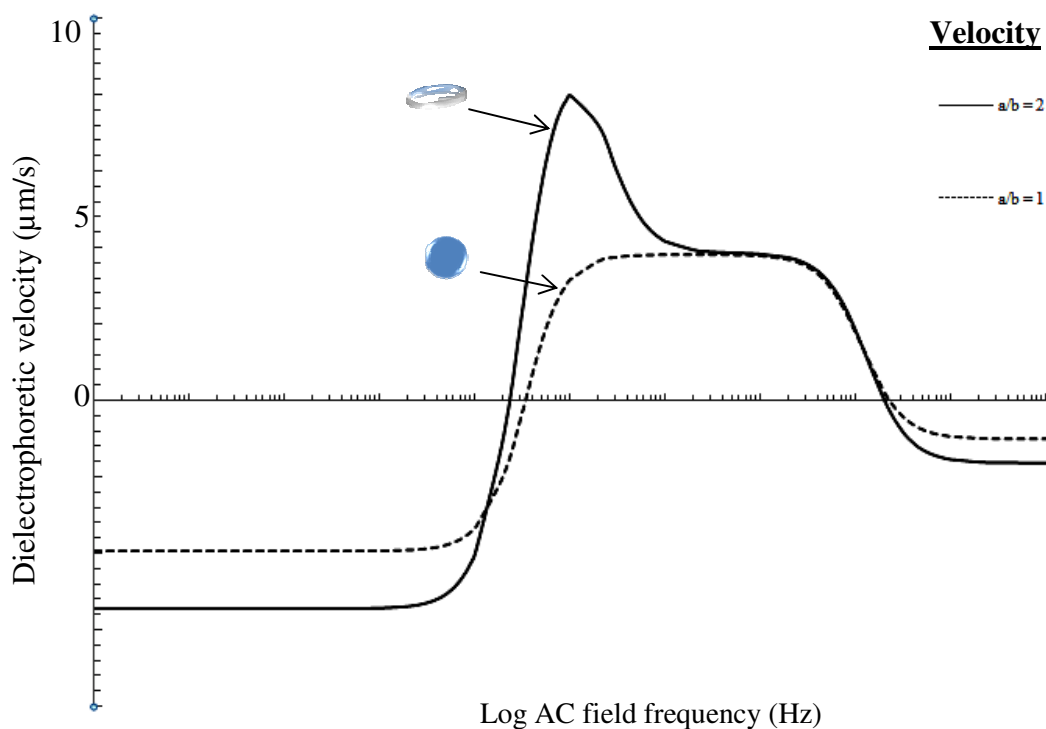


Fig. 3.5 Theoretical plots of dielectrophoretic velocity as transformed from the spheroidal model (Eq. 3.9) to a sphere by choosing three equal semi-axes ($a = b = c$) (see Fig. 2.1a also). The parameters used for these plots are the same as for Fig. 3.2.

3.4 Discussions and Conclusions

Although Eqs. (3.7) and (3.8) describe the balance force between F_D^{ν} , F_{cDEP}^{ν} and F_{twDEP}^{ν} , it is possible that the direction of F_{cDEP}^{ν} and F_{twDEP}^{ν} in Fig. 3.1b might inclines from the horizontal line with an angle θ due to the nonuniformity of the imposed field E^{ν} . The F_{cDEP}^{ν} and F_{twDEP}^{ν} may be expressed with an additional function of $\cos\theta$. Nevertheless, $F_{twDEP}^{\nu} \cos\theta \approx F_{twDEP}^{\nu}$ when $\frac{y}{d} \geq 1$ and $\cos\theta = 1$ as assumed in theoretical approach of electromagnetic wave (Morgan *et al.* 2001). In addition, the thickness of the electrode is very small (0.2 μm) compared with cell sizes (4 μm of *S.cervisiata* and 10 μm of *Tetraselmis*). This leads to the assumption of small nonuniformity of the field. The approximation is only reliable in particular case of $d_1 = d_2 = d$.

To compute term of travelling electric field strength (E) and its gradient (∇E^2) generated from the electrode, some approximations was made during operating the *Quick Field*TM program, viz. the thickness of the electrode was neglected compared with the electrode width and length. In case of a thick electrode, a numerical method might be taken into account, as suggested by Morgan *et al.* (2001), to calculate the exact value of E . According to his work, a Fourier series wave was solved for the E and followed with the finite element method as conducted by Green *et al.* (2002). Analyses of numerical method for solving the solutions of travelling electric field were given in details elsewhere (Chang *et al.*, 2003; Feng *et al.*; Fu *et al.*, 2004).

References

1. Castellanos A., Ramos A., Gonzalez A. 2003. Green N.G. and Morgan H., "Electrohydrodynamics and dielectrophoresis in Microsystems: scaling laws," *J.Phys.D:Appl.Phys.*, 36: 2584-2597.
2. Chang D.E., Loire S. and Mezic I. 2003. Closed-form solutions in the electrical field analysis for dielectrophoretic and travelling wave inter-digitated electrode arrays. *J.Phys.D:Appl.Phys.*, 36: 3073-3078.
3. Feng J.J., Krishnamoorthy S., Chen Z.J. and Makhijami V.B., Numerical and analytical studies of AC Electric field in dielectrophoretic electrode arrays. *Private documents*.
4. Fu L.M., Lee G.B., Lin Y.H. and Yang R.J. 2004. Manipulation of microparticles using new modes of traveling wave dielectrophoretic Force: Numerical simulation and experimentants. *J.IEEE/ASME Trans.Mechatronics*, 9(2): 377-383.
5. Green N.G., Ramos A. and Morgan H. 2002. Numerical solution of the dielectrophoretic and travelling wave forces for interdigitated electrode array using the finite element method . *J.Electrostatics*, 56: 235-254.
6. Hagedorn R., Fuhr G., Muller T. and Gimsa J. 1992. Trveling-wave dielectrophoresis of microparticles. *Electrophoresis*, 13: 49-54.
7. Happel J. and Brenner H. 1983. *Low Reynolds Number Hydrodynamics*, Martinus Nijhoff.
8. Hughes M. P. 2000. AC electrokinetic: applications for nanotechnology. *Nanotechnology* , 11: 124-132.

9. Jones T.B. 2003. Basic Theory of dielectrophoresis and electrorotation. *IEEE Engineering in medicine and biology magazine*, November/December, pp. 33-42.
10. Li W.H., Du H., Chen D.F. and Chu C. 2004. Analysis of dielectrophoretic electrode arrays for nanoparticles manipulation. *J.Comp.Materials.Sci.*, 30: 320-325.
11. Mahaworasilpa T., Coster H. G. L. and George E. P. 1994. Force on biological cells due to Applied (AC) electric fields. I. Dielectrophoresis. *Biochim Biophys Acta*. **1193**: 118-126.
12. Morgan H., Izquierdo A.G., Bakewell D., Green N.G. and Ramos A. 2001. The dielectrophoretic and traveling wave forces generated by interdigitated electrode arrays: analytical solution using Fourier series," *J.Phys.D:Appl.Phys.*, 34: 1553-1561.
13. Pohl H.A. 1978. Dielectrophoresis: the behaviour of neutral matter in non-uniform electric fields, Cambridge, U.K., Cambridge Press.
14. Wang X. B., Hughes M. P., Huang Y., Becker F. F. and Gascoyne P. R. C. 1995. Non-uniform spatial distributions of both the magnitude and phase of AC electric fields determine dielectrophoretic forces," *Biochimica et Biophysica Acta*, 1243: 185-194.

CHAPTER 4

MATERIALS AND METHODS

4.1 Cell Preparations

Cell suspensions in a low conducting medium were employed for the present study. Cells were electrically induced in traveling electric field with in an appropriate conductivity of the medium. Cell velocity and two critical frequencies during dielectrophoresis were observed through experiments. Interactions among the dipole moment of neighbor cells might affect each cell velocity. Measurements of the cell velocity might be disturbed, leading to pearl chain formation (Pohl, 1978). To avoid this problem, dilute cell density was used. Cell densities to be used for experiments were thus considered as two values for a comparison study.

Saccharomyces cervisiata (TISTR 5088) (Fig. 4.1) and *Tetraselmis* sp. (marine phytoplankton) (Fig. 4.2) were prepared as a model for this study. The former was supplied by Department of Biotechnology, Faculty of Agro-Industry, Prince of Songkhla University and the latter from the National Institute for Coastal Aquaculture (NICA). Suspensions of both cells were prepared as a control (living) and heated cells as well as arsenic pre-treated cells for experimentations. Details of the cells preparations are described below. Experiments of these cells were carried out for comparisons with the theoretical analysis. This analysis was deduced to the dielectric properties of the cells.

4.1.1 Yeast Cells

S. cervisiata (Fig. 4.1) were grown in 70 g.l⁻¹ of Peptone Yeast Extract Agar (PDA, Criterion) at 27 °C in an incubator-shaker (Jecons Scientific, model JS201) at 200 rpm (Raicu *et al.* 1996).

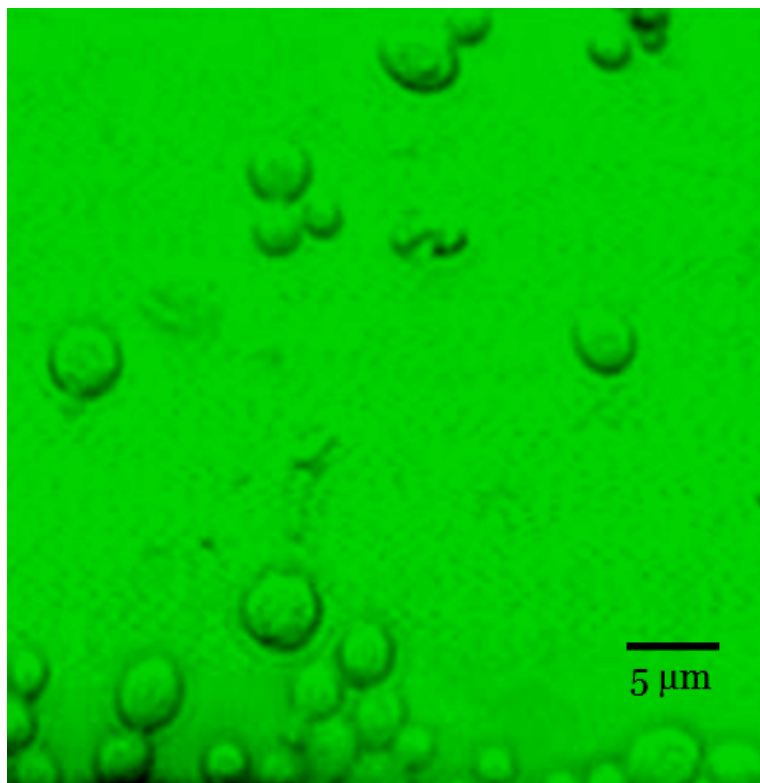


Fig. 4.1 *S. cervisiolate* (TISTR 5088) were suspended in 0.5 M sorbitol.



Fig. 4.2 *Tetraselmis* sp. suspended in the 0.5 M sorbitol medium.

The cells were harvested in the stationary phase after 24 hr and washed twice with deionized water, then centrifuged (Denver Instrument, M0009861, USA) at 1,000 rpm for 2 min and re-suspended twice in a 0.5 M sorbitol (Fluka Biochemika Assay > 98%) of 0.01 S.m⁻¹. The solution conductivity (σ_s) was measured using a conductivity meter (Tetracon 325, LF318, Germany) and the conductivity was adjusted from 0.01 to 0.40 S.m⁻¹ by adding 0.1M KCl solution, with a micropipette (Nichipet, model 5000DG, Japan).

To induce cell translation in a traveling electric field, the cell densities were diluted and fixed as 1.15 x 10⁵ and 5.75 x 10⁴ cell/ml. Cell suspensions were dropped onto the glass slide between the electrodes. To assure that all the TPI electrode tips were submerged in the suspension drop, a volume (V) of the cell suspension was estimated from $V = \frac{4}{3}\pi r^3$, where $r \geq 4(d_1 + d_2)$ (see Fig. 4.3). The estimated value of r was about 2-2.5 mm and the volume was about 100 μ l.

In the case of heated cells, the method described by Wanichapichart *et al.*, (2007) was employed. They were heated at 75 °C for 10 min., cooled down at room temperature 25 °C then centrifuged as described for viable cells.

4.1.2 *Tetraselmis* sp.

Tetraselmis cells are spheroids (10.0 ± 0.7 μ m × 8.0 ± 0.5 μ m) (Fig. 4.2). The cells were cultured in an artificial sea-water (ACW), Sato and Serikawa's medium (Sato and Serikawa, 1978). To change the solution conductivity, the cells were centrifuged using 7,000 rpm for 2 min. They were then re-suspended twice in the 0.5 M sorbitol of 0.01 S.m⁻¹ conductivity, using the same rotation speed. The conductivity of the solution (σ_s) was later adjusted using 0.1 M KCl solution.

The cell density of *Tetraselmis* to be used for each experiment was fixed at 9.2×10^6 and 4.0×10^5 cell/ μl for a comparison study. It was determined using a hemocytometer (BOECO, Germany). Cell samples of about $100 \mu\text{l}$ were dropped in the middle of the TPI electrode by using a micropipette (see Fig. 4.3b).

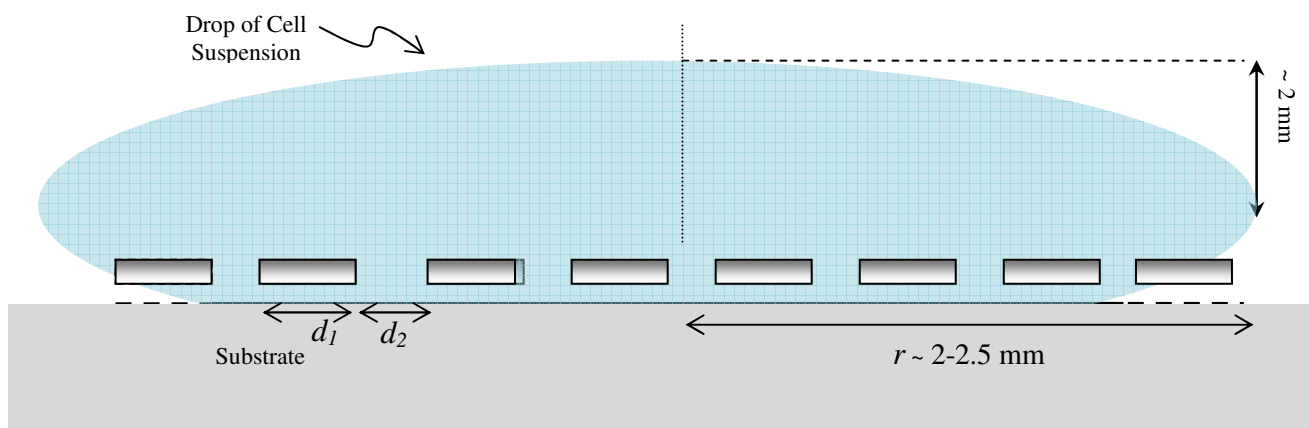
As reported by Wanichapichart *et al.* (2007), dead cells were prepared by heating at 80°C for 10 min, cooling down to room temperature and then centrifugation. Arsenic pretreated cells were prepared by adding an arsenic solution (NaAsO_2 , Sigma- Aldrich 99%) to the cell culture at concentration varying from 1 to 150 ppm and left at room temperature for 24 hrs. Then, the cells were centrifuged and washed as described for the control.

4.2 Electrode Fabrications

4.2.1 Preliminary Micro-channel TPI Electrode

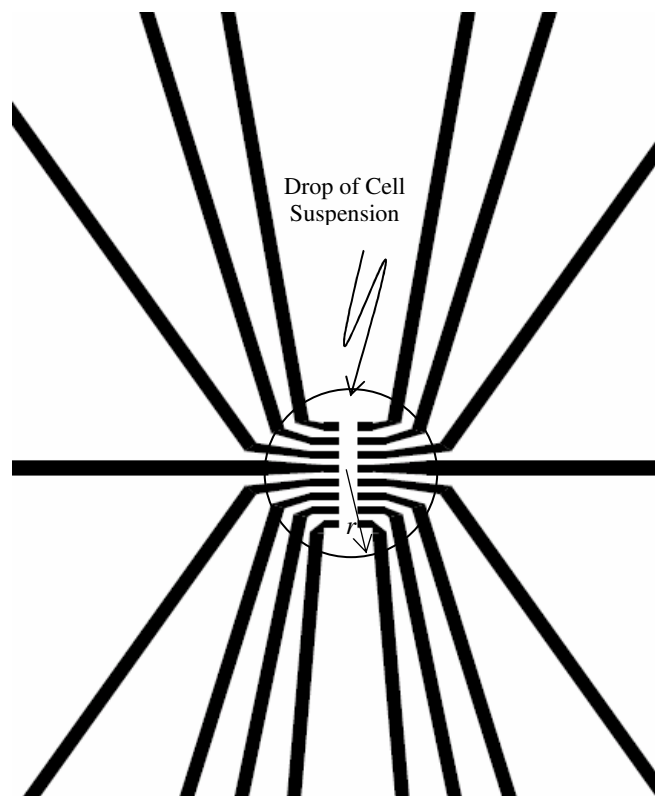
In a preliminary study, cell induction in travelling electric field was performed by using a peristaltic pump (MP-3N, Japan) to feed cell suspensions through the microchannel (Fig. 4.4a) of the interdigitated electrode (Fig. 4.4b). The cell suspension was fed via the microtube (1 mm in diameter) with a constant minimum flow rate of $10 \mu\text{l} \cdot \text{min}^{-1}$.

With the lowest flow rate, it was found that the pressure damaged the gold tips as an example shown in Fig. 4.5. To circumvent this problem, all flow was replaced by a drop on to the TPI electrode and the plastic wall (Fig. 4.4a) was removed.



(Not to scale)

(a)



(b)

Fig. 4.3 Drop of cells suspension on the electrode was illustrated in (a) Side view and

(b) Top view. The volume (V) of hemisphere of radius (r) was estimated from $\frac{4}{6}\pi r^3$

to be sure that $r \geq 4(d_1 + d_2)$.

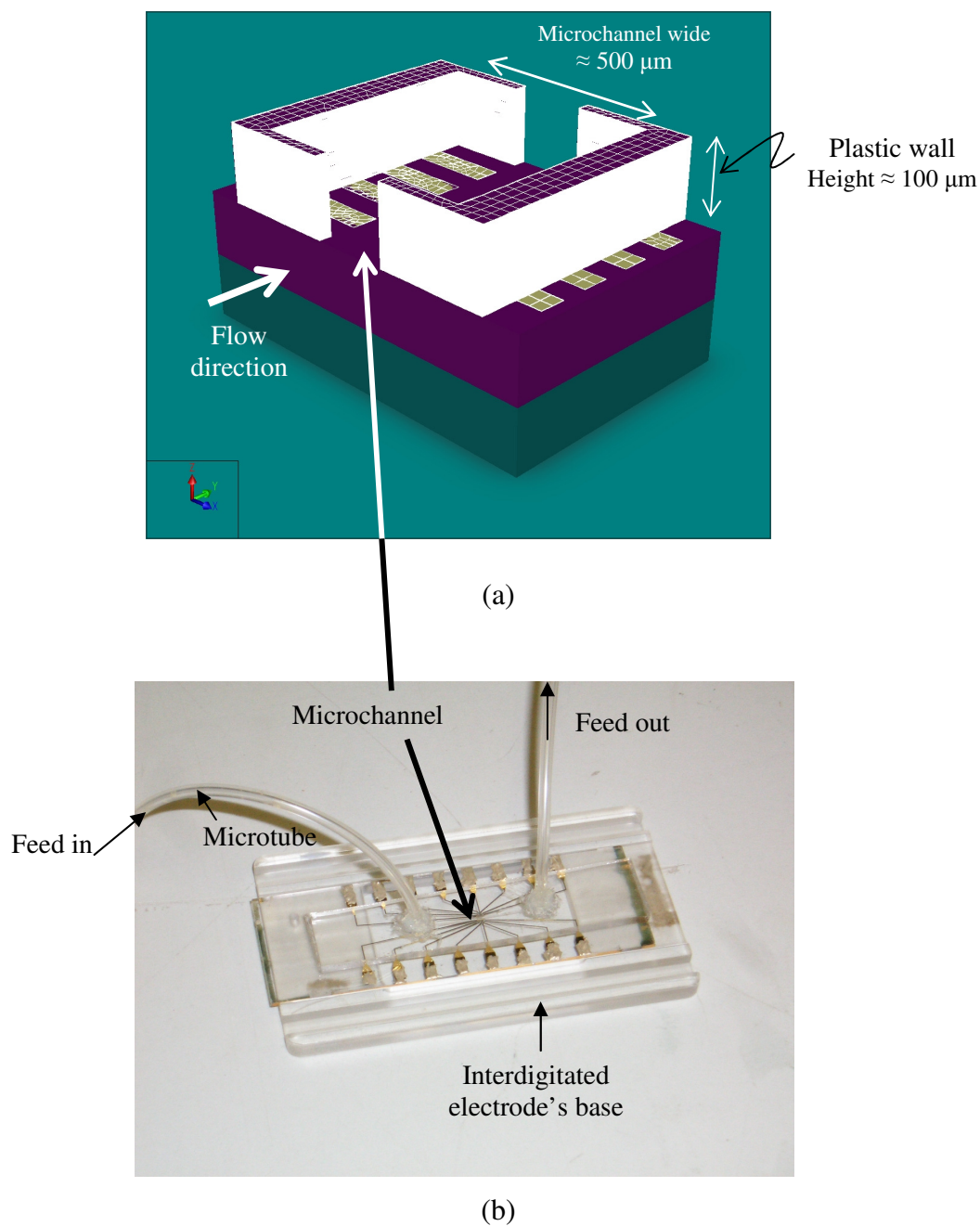


Fig. 4.4 The previous microchannel-TPI electrode. (a) Simulation of the microchannel of the electrode by using Coventor WareTM and (b) the electrode connecting with microtube was mounted on the electrode's base.

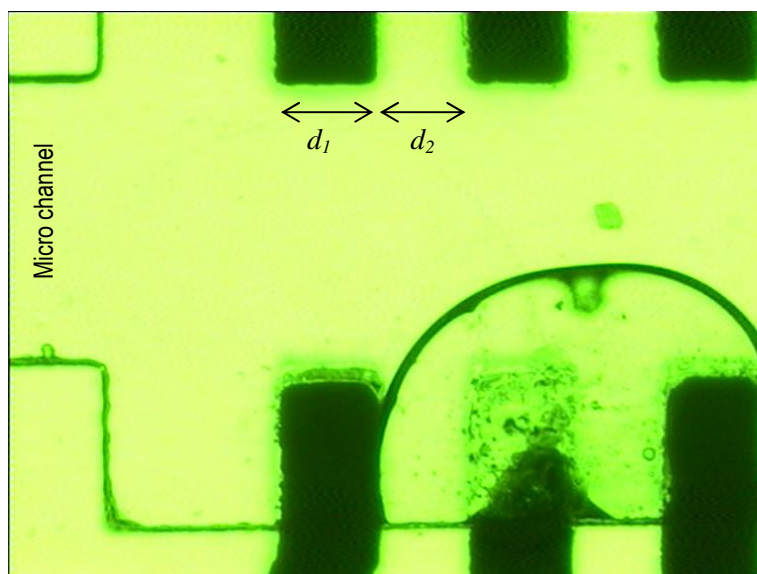
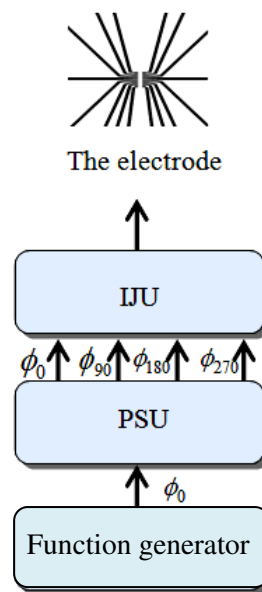
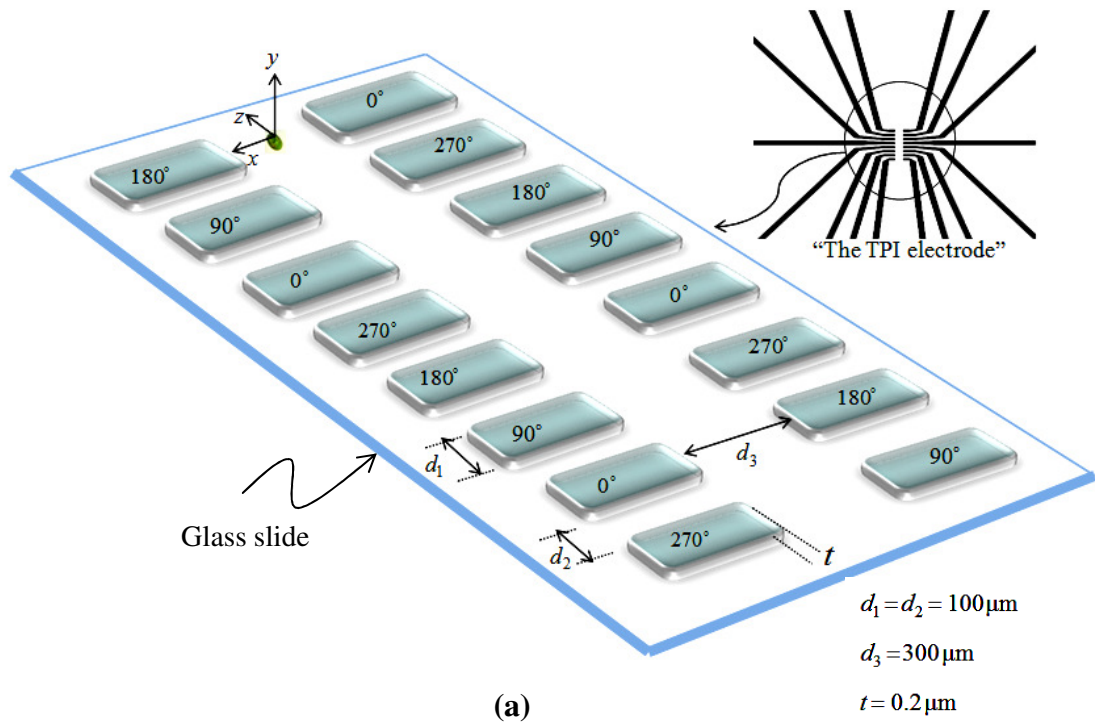


Fig. 4.5 One tip of the TPI electrode was damaged while the suspension was being feed through the microchannel.

4.2.2 Micro Electrode Array

The electrode used throughout experimentations for the present study was fabricated by National Electronics and Computer Technology Center (NECTEC) on a microscope glass slide of dimension $80 \times 30 \times 1$ mm (Marienfeld, Germany) (Fig. 4.6a). The slide was first annealed at $400 \text{ }^\circ\text{C}$ for 4 hr to relieve internal residual stress. Photomasks defining the bar shaped electrode “interdigitated electrode” were generated using a layout software (AutoCAD) and were then printed on a transparent film using a high-resolution laser printer (10 000 dpi).

Electrodes fabrication commenced with the standard wafer-cleaning process. Process solutions were prepared using deionized (DI) water. The glass substrates were immersed in a Piranha solution at $120 \text{ }^\circ\text{C}$ for 10 min and then rinsed in DI water and blown-dry with nitrogen gas. Using an E-beam evaporation process, an adhesion layer



(b)

Fig. 4.6 A configuration of the TPI electrode and the quadrature phase sequence as shown in (a) three dimensional view (not to scale) and (b) diagram of electrical set up with an adjustable phase shift unit (PSU) connecting with an interjunction unit (IJU).

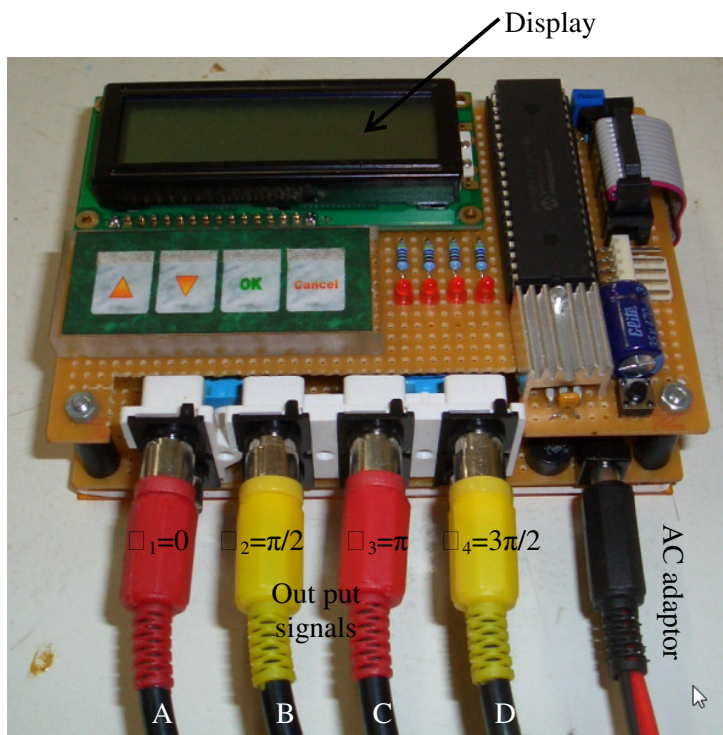
-of 0.02 μm chromium (Cr) was deposited onto the glass substrate, followed by deposition of a 0.2 μm layer of gold. The bar-shaped array of microelectrodes was then patterned using a standard photolithography and metal etching process. Finally, the photoresist layer was striped by a KOH solution at 50 $^{\circ}\text{C}$. An upper polydimethylsiloxane “PDMS” plate with a microchannel (60 μm in width and 100 μm in depth) was used to cover the cell chamber. Detailed information relating to all process was provided by Fu *et al.* (2004). The PDMS plate was oxygen-plasma-treated with gold (99%) and then bonded with the glass substrate. All processes were taken place in a clean room of class 100 (TIDI, MEMS-NECTEC).

The gold electrodes so formed on the slide were 200 μm long, 100 μm wide (d_1), and 0.2 μm thick (t). The separation of the adjacent bars on the same array (d_2) was 100 μm and that for the central channel (d_3) is 300 μm (see Fig. 4.6a).

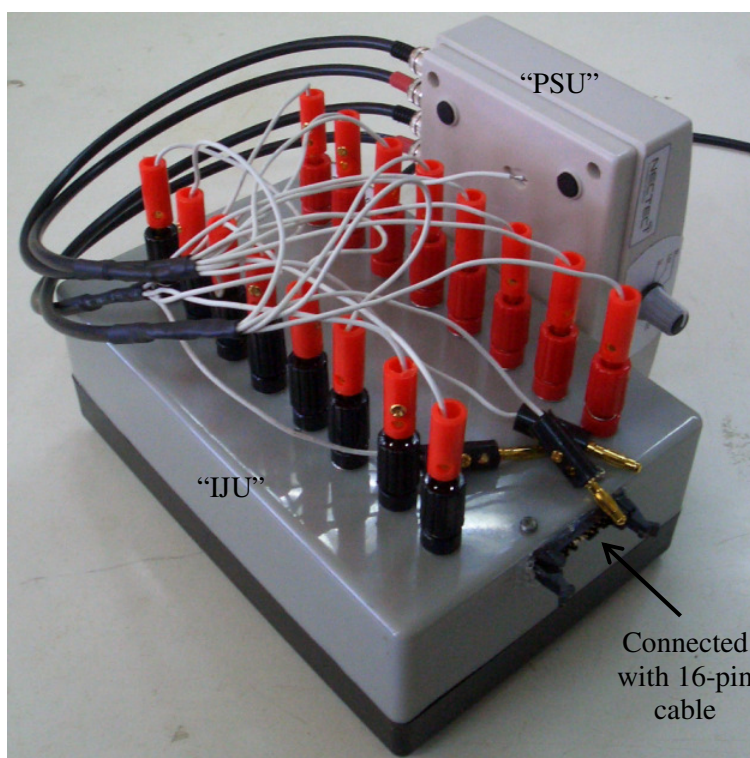
4.3 Electrical Set-Up and Data Collection

To induce cell suspensions in travelling electric field, the electrode array was energized with four sinusoidal signals (a quadrature phase) varied from 1 to 10 Vpp in amplitude, in a phase sequence as described by Wang *et al.* (1995). This was achieved by setting electrical set-up as shown in Fig. 4.6b.

A synthesized function generator (Stanford Research Systems, 30 MHz Model DS345, and California) was connected to the adjustable phase shift unit (PSU) (Fig. 4.7a) to split an AC signal into a quadrature phase with the same frequency. The quadrature phase was $\phi_1=0$, $\phi_2=\pi/2$, $\phi_3=\pi$ and $\phi_4=3\pi/2$. These phases were connected to the sixteen bars of the electrode array via a home-made interjunction unit (IJU) (Fig. 4.7b). An example of output signals for the quadrature phase with zero time-delay is shown in Fig. 4.8. Figure 4.9 shows the instantaneous signals with 200 ms time-delay, due to appropriate chosen signal phases.



(a)



(b)

Fig. 4.7 Pictures of (a) the adjustable Phase Shifted Unit (PSU) connected with (b) the Inter-Junction Unit (IJU).

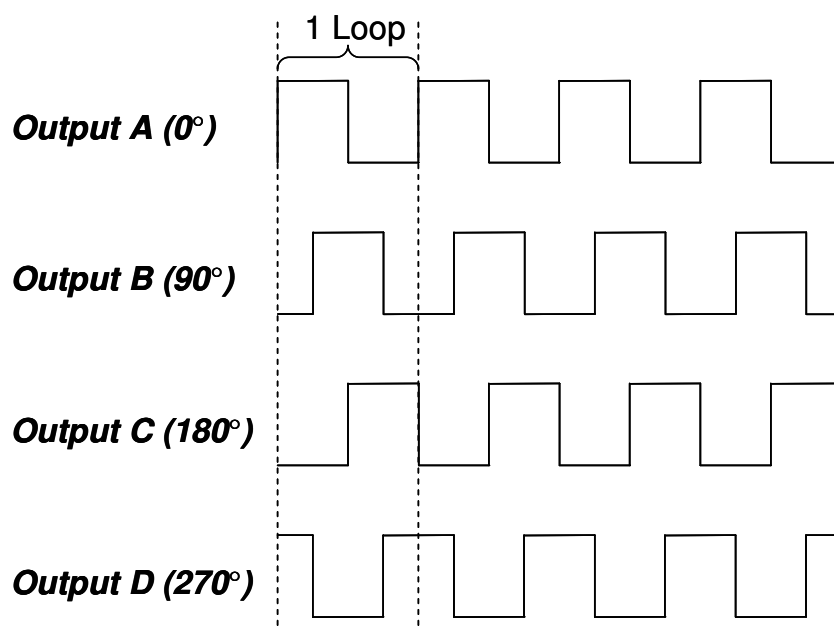
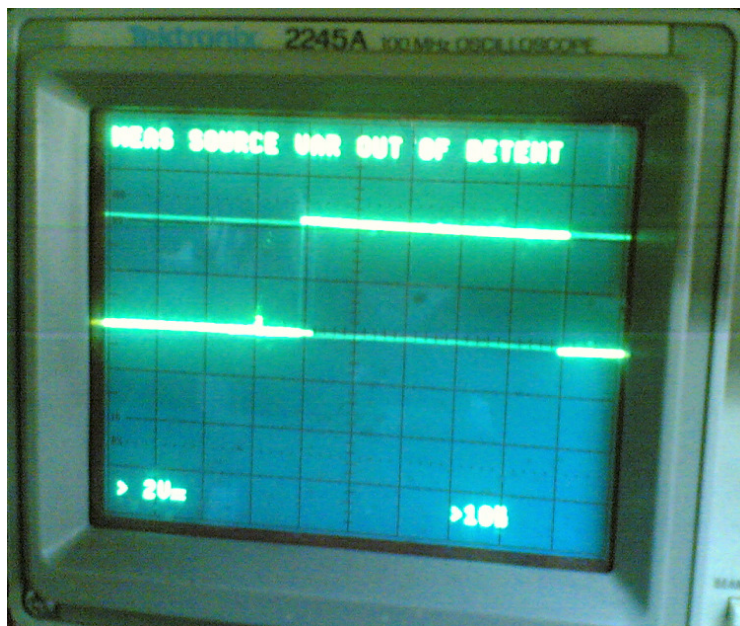
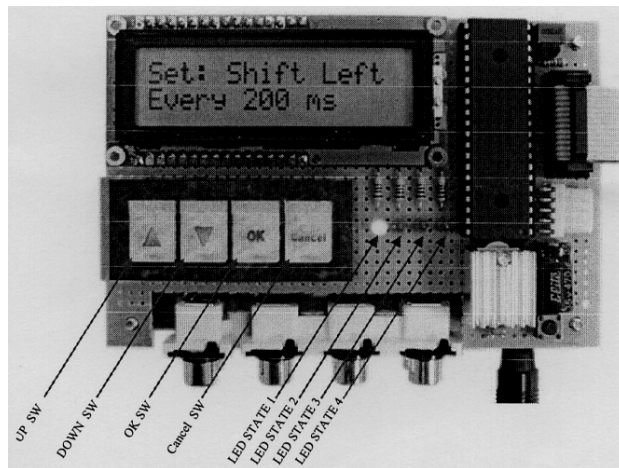
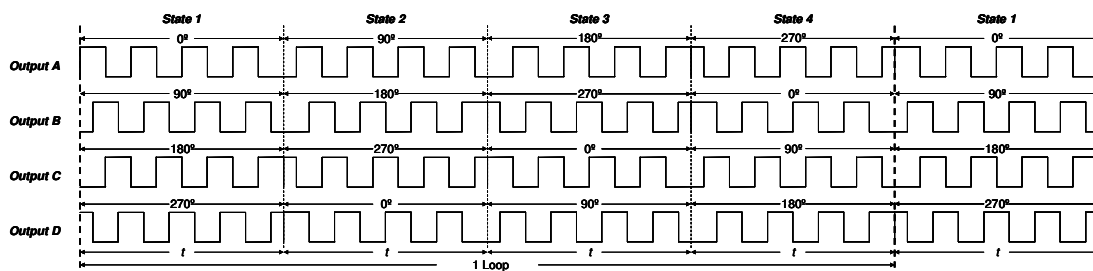


Fig. 4.8 Four output AC signals with zero time-delay measured from oscilloscope (100 MHz oscilloscope 2245A).

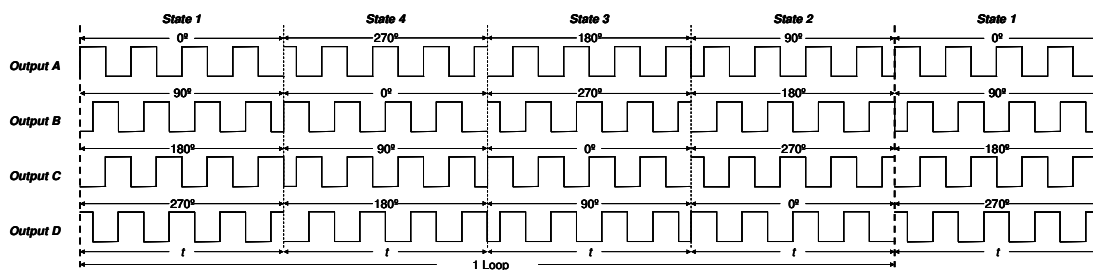


IN \ O	State1				State2				State3				State4			
	A	B	C	D	A	B	C	D	A	B	C	D	A	B	C	D
0°	X					X					X					X
90°		X					X					X	X			
180°			X					X	X					X		
270°				X	X					X					X	

(a)



(b)



(c)

Fig. 4.9 The “PSU” generated the quadrature phases with time-delay of 200 ms. When instantaneous states of four signals driven through cable A, B, C and D changed from state 1 to state 4 (a), the signals shifted to the right (b), or to the left (c) depending on operating knobs.

Images of cell translational motion were recorded using a CCD camera (Sony SLV-Japan), which was connected to a microcomputer (Acer, Aspire 4310 Vista) via the *Winfast PVR™* program. Computations of v_{cDEP}^p were made through the *Winfast PVR™* program with a time-accuracy of 0.01 sec. Three separate measurements were made to obtain the velocity data and two critical frequencies (f_λ, f_h) were investigated. To determine f_λ and f_h , the frequency of the applied signals was gradually decreased from the upper (30 MHz limit) to the lower values. Each experiment took place within 5 min.

4.4 Calculations of Electric field Strengths

Electric field intensities were calculated using the *Quick Field™* program version 5.5 and the finite element analysis in the AC conduction mode (Tera Analysis Ltd., freeware from www.quickfield.com). The simulation of electric field profile in two-dimension has been shown in Fig. 3.3 (in chapter 3). The accuracy for the electric field simulations depended on RAM capacity in the microcomputer employed (Acer Aspire 4310, 1.0 GB).

To operate the *Quick Field™* program in the AC conduction mode, field sources (electrode type and geometry) and boundary conditions were taken into account. The electrode geometry was fixed as d_1 , d_2 and d_3 shown in Fig. 4.6a. For the present study the phase sequence was shifted to $\pi/2$ with time delay chosen.

References

1. Fu, L. M., Lee, G. B., Lin, Y. H. and Yang, R.J. 2004. Manipulation of micro - particles using new modes of traveling-wave-Dielectrophoretic Force: Numerical simulation and experimants. *J.IEEE/ASME Trans.Mechatronics.*, 9(2):377-383.
2. Pohl H. A. 1978. Dielectrophoresis: The behaviour of neutral matter in non-uniform electric fields, Cambridge, U.K.,Cambridge Press,
3. Raicu V., Raicu G. and Turcu G. 1996. Dielectric properties of yeast cells as simulated by the two-shell model. *Biochim. Biophys.Acta*, 1274:143-148.
- 4.Sato T. and Sarikawa M. 1978. Massculture of a marine diatom, *Nitzchia closterium*. *Bull.Plankt. Soc.* 15(1):13-16.
5. Wang X. B., Hughes M. P., Huang Y., Becker F. F. and Gascoyne P. R. C. 1995. Non-uniform spatial distributions of both the magnitude and phase of AC electric fields determine dielectrophoretic forces. *Biochimica et Biophysica Acta*, 1243: 185-194,
6. Wanichapichart P., Wongluksanapan T., and Khooburat L., 2007, Proceeding of the 2nd IEEE International Conference on Nano/Micro Engineering and Molecular Systems, pp. 1115-1120.

CHAPTER 5

CELL DIELECTRIC USING LAPLACE APPROACH

5.1 Introduction

In chapter 3, theoretical analysis of dielectrophoretic velocity (v_{cDEP}^p) of a spheroid in travelling electric field was presented in Eq. (3.9) (page 75). The amplitude of v_{cDEP}^p is dependent on the gradient of electric field (∇E^2), which is equivalent to changes of the amplitude (V_0) of the applied signal described in section 4.4. The v_{cDEP}^p is also a function of the real part of the Clausius-Mossotti factor (Re[CMF]), which reflects the cell dielectric properties. Hence, determinations of the cell dielectric parameters can be made through a comparison of the experimental and theoretical v_{cDEP}^p values.

To verify the theoretical predictions for a spheroidal model used in the present study, experimental v_{cDEP}^p values for living *S. cervisiata* and *Tetraselmis* undergoing dielectrophoresis were measured over a AC field frequency range of 10 kHz to 30 MHz. Data fittings were carried out on the effect of the conductivity of the suspending medium (σ_s), electric field (E) strengths as described in chapter 4. In addition the cell densities were also varied.

To investigate how cell stages under environmental changes can be meaningful explained with the theory developed, experiments were also carried out with non-living (dead) cells of *S. cervisiata* and arsenic pretreated *Tetraselmis*. These will be presented in chapter 7.

5.2 Materials and Methods

For the travelling electric field dielectrophoresis experiments, *S.cervisiata* and *Tetraselmis* were prepared as described in chapter 4, section 4.1.1 and 4.1.2, respectively. Investigations of experimental values of V_{cDEP}^p for both cells were made over AC field frequency range from 10 kHz to 30 MHz. The frequency of the applied signals was initially set to the highest frequency and then gradually reduced to the lower frequencies so that “Joule-heating” was minimized. It should be noted that Joule-heating problem can be significant at the lower frequencies because the current is then largely an ionic current whilst at high frequencies this is less of a problem because the current is then largely a non-dissipative displacement current. The highest frequency was 30 MHz, the limitation of the function generator used for the present study. The conductivity of the suspending medium (σ_s) was varied from 0.01 to 0.30 S.m⁻¹. It should be noted that the lowest value of σ_s of 0.5 M sorbitol solution employed for the present study was about 0.010 ± 0.003 S.m⁻¹. The higher values of σ_s were attained by addition of 0.1M KC λ solution.

Cells were exposed to electric field strengths of various values, by increasing the voltage across the electrodes V_0 from 1 to 10 Vpp, the maximum voltage of the function generator used for the present study. However, to compare experimental data with the theory (Eq. 3.9), the electric field were adjusted by varying the amplitude of the applied signal, V_0 to values of 1, 2, 4, and 10 Vpp, which corresponded to field strengths of 14, 28, 57, and 143 kV.m⁻¹, respectively. Calculations of electric field strengths were made using the *Quick Field*TM program (see explanations in section 4.4, chapter 4).

The dielectric properties obtained for *S.cervisiata* were compared with those in the literatures and extensions of the model were made with *Tetraselmis*.

5.3 Dielectrophoretic velocity

5.3.1 *S.cervisiata*

5.3.1.1 Effect of cell densities

Experimental results show that cells exhibited both positive and negative dielectrophoresis where only the cross over frequency to the negative dielectrophoresis region, that is the lower critical frequency (f_{λ}) was found. Plots of cell velocity v_{cDEP}^{μ} as a function of AC electric field frequency are shown in Figs. 5.1 and 5.2. Experimental results show no differences in v_{cDEP}^{μ} spectra for the two cell densities used. In Fig. 5.1, the v_{cDEP}^{μ} spectra of 1.15×10^5 and 5.75×10^4 cell/m λ are compared when σ_s was fixed as 0.01 S.m^{-1} and electric field strengths (E) are changed from 28 to 143 kV.m $^{-1}$ (Figs. 5.1a to 5.1c). Increasing E enhances the v_{cDEP}^{μ} magnitude and vice versa. The same results were found with the case of $\sigma_s = 0.03 \text{ S.m}^{-1}$ which is shown in Fig. 5.2. It should be noted that the value of both E and σ_s affect the magnitude of v_{cDEP}^{μ} as the following reports.

5.3.1.2 Effect of electric field strengths (E)

Effects of electric field strength (E) on the v_{cDEP}^{μ} spectra are also found in Figs. 5.1 and 5.2. In case of $\sigma_s = 0.01 \text{ S.m}^{-1}$ as shown in Figs. 5.1a, b and c; increasing E from 28 to 143 kV.m $^{-1}$ enhance the peak of the v_{cDEP}^{μ} spectra from 1.25 ± 0.12 to $3.38 \pm 0.4 \mu\text{m.s}^{-1}$. It should be note that changes in E only affect the

magnitudes of the v_{cDEP}^p spectra. Again, the f_λ is not affected by the change of E . The maximum value of the v_{cDEP}^p spectrum of experiments with a cell density of 1.15×10^5 cells/ $m\lambda$ was $3.38 \pm 0.4 \mu\text{m.s}^{-1}$ at 3.5 kHz when $E=143 \text{ kV.m}^{-1}$ (Fig. 5.3a). Similar results were obtained in experiments with 5.75×10^4 cells. ml^{-1} density (Fig. 5.3b). These results agreed well with the above finding.

5.3.1.3 Effect of the Conductivity of the Suspending Medium (σ_s)

When the values of σ_s were increased in steps to 0.03, 0.06 and 0.10 S.m^{-1} , the magnitudes of v_{cDEP}^p spectra were decreased dramatically as shown in Figs. 5.4, 5.5 and 5.6, respectively. As seen from Fig. 5.4a and b, for $\sigma_s = 0.03 \text{ S.m}^{-1}$, $E=143 \text{ kV.m}^{-1}$, the maximum value of the v_{cDEP}^p spectrum was $2.23 \pm 0.26 \mu\text{m.s}^{-1}$ at 14 kHz, the same for both cell densities. The same experiment was carried in Figs. 5.5 and 5.6, only σ_s was increased. The increased σ_s shifted the f_λ towards higher frequency in all cases, while the maximum v_{cDEP}^p value was reduced. As found in 5.3.1.2, the maximum E used in the present study ($E=143 \text{ kV.m}^{-1}$) gave a maximum value of the v_{cDEP}^p spectrum, reaching $1.65 \pm 0.21 \mu\text{m.s}^{-1}$ at 19 kHz. This study was also found that if σ_s was larger than $0.25 \pm 0.04 \text{ S.m}^{-1}$, dielectrophoresis of yeast cells in travelling wave could be induced.

5.3.2 *Tetraselmis*

The experimental conditions used to measure the v_{cDEP}^p spectra for *Tetraselmis* were the same as described for yeast cells. The following are each effect.

5.3.2.1 Effect of cell densities

Figures 5.7 and 5.8 showed no differences in v_{cDEP}^p spectra for the two cell densities of *Tetraselmis* used and this was the case for each σ_s used. Similar to what was observed in yeasts, the value of both σ_s and E did not affect the cross over frequency to the negative dielectrophoresis region. Hence the lower critical frequency f_λ was not dependent on either σ_s or E .

5.3.2.2 Effect of electric field strengths (E)

Figure 5.9 shows the results for $\sigma_s = 0.01 \text{ S.m}^{-1}$ when E was varied. It was found that increasing the values of E result in increasing the magnitude of v_{cDEP}^p . For cells densities of $9.2 \times 10^6 \text{ cells.ml}^{-1}$ and $E=143 \text{ kV.m}^{-1}$ (Fig. 5.9a), the maximum value of the v_{cDEP}^p was $29.5 \pm 0.3 \text{ }\mu\text{m.s}^{-1}$ at 50 kHz.

5.3.2.3 Effect of the Conductivity of the Suspending Medium (σ_s)

When the values of σ_s were increased in steps to 0.03, 0.06 and 0.10 S.m^{-1} , the magnitudes of v_{cDEP}^p spectra were decreased dramatically as shown in Figs. 5.10, 5.11 and 5.12, respectively. For $\sigma_s = 0.03 \text{ S.m}^{-1}$ and cells density of $1.15 \times 10^5 \text{ cells.ml}^{-1}$, the maximum value of the v_{cDEP}^p was $2.23 \pm 0.26 \text{ }\mu\text{m.s}^{-1}$ at 14 kHz when $E=143 \text{ kV.m}^{-1}$. Similar results were also obtained in experiments using cell densities. It was clear that there were no differences in v_{cDEP}^p spectra between two cases of cell

densities for each σ_s used for the present study, even through the values of E and σ_s were changed.

The maximum values of σ_s at which travelling wave dielectrophoresis could be induced with *Tetraselmis* was $0.37 \pm 0.03 \text{ S.m}^{-1}$.

5.4 Data Fittings

From Eq. 3.9 (chapter 3), the dielectrophoretic velocities are solely dependent on the dielectric and conduction properties of the cytoplasm (ε_c, σ_c), the membrane (ε_m, σ_m), and the suspending medium (ε_s, σ_s), respectively. These parameters generally affect different characteristic features of dielectrophoresis spectrum. It is clear from Figs. 2.6c and d, the conductivity and permittivity of the cytoplasm has a more pronounced affect on the magnitude of the positive velocity part of the spectra and the value of the higher critical frequency. As seen from Figs. 2.6e and f, the dielectric properties of the membrane dominate the spectrum at lower frequencies and determine the magnitude of the negative velocity spectra. The cell size and the membrane thickness also play a role in determining the spectra.

In order to fit the experimental data to the theoretical expressions, it is necessary to take into account experimental errors. This allows one to deduce the values of the parameters with a quantitative estimate of the best fit. For the v_{cDEP} spectra, the error χ in fitting the data to the theoretical expression can be defined as:

$$\chi = \frac{\sum_{i=1}^N \left(\frac{\sqrt{(v_{\text{exp.}(i)} - v_{\text{theory}(i)})^2}}{\sqrt{(v_{\text{exp.}(i)})^2}} \right)}{N} \times 100 \quad (5.1)$$

where $v_{\text{exp.}(i)}$ and $v_{\text{theory}(i)}$ are the magnitudes of the experimental and the theoretical dielectrophoretic velocity and N is the number of data points (frequencies).

To obtain the best fit it is necessary to minimize Eq. (5.1) by adjusting the parameters in the theoretical expressions. However, there are at least 4 parameters (conductivities and dielectric constants) that cannot be independently measured. In addition the cell membrane thickness is not precisely known.

The method to fit the theoretical curve with that of the experiments to obtain cell dielectric parameters were made based on the knowledge of sensitivities of dielectric parameters shown in Fig. 2.6. Theoretical plots in Figs. 5.13 and 5.14 showed the fitting results for the dielectrophoretic velocity spectrum of *S. cerevisiae* and *Tetraselmis*, respectively, which gave a value of Chi (Eq. 5.1) of less than 10%.

5.5 Discussions and Conclusions

The experimental results show that for both cells, electric field strengths (E) and the conductivity of the suspending medium (σ_s) affected the magnitudes of the v_{cDEP}^p spectra. Decreasing the values of E reduced the magnitudes of the v_{cDEP}^p spectra. In contrast, decreasing the values of σ_s enhanced the magnitudes of the v_{cDEP}^p spectra. The two cell densities used for the present study had no effect on the v_{cDEP}^p spectra.

In this chapter the dielectric properties of the membrane and the cytoplasm of *S. cerevisiae* and *Tetraselmis* were determined by curve-fitting the dielectrophoretic velocity (v_{cDEP}^p) to the theoretical expressions for dielectrophoresis. The estimated dielectric parameters were shown in Table 5.1. The parameters obtained for yeast cells agree well with control experiments reported in the literatures (Zhou *et al.*, 1996; Raicu *et al.*, 1996), when electrorotation technique and two-shell model were studied under the effect of contamination. However, the value of the relative

permittivity of the membrane (ϵ_m) estimated from the present study was greater than that of the literatures about two times. In case of *Tetraselmis*, the parameters obtained are slightly different from the control experiments reported in Wanichapichart *et al.* (2002) and (2007) when a single cell dielectrophoresis and electrorotation techniques were employed, respectively. As seen from the later works the specific capacitance of the membrane (C_m) estimated from the present study is greater than that of the literatures, while the specific conductance of the membrane (G_m) reported by the literature is much greater than that of the present study (see Table 5.2).

In the present study, the v_{cDEP}^p spectra were obtained directly from cell suspensions instead and each cell was selected for the measurement, whereas only one cell was induced in previous report by Mahaworasilpa *et al.* (1994). It should be noted that the characteristic spectra of v_{cDEP}^p , especially the peak value, can be more readily determined when the conductivity of the suspending medium σ_s is low. For higher values of σ_s , the peak of the $\text{Re}[\text{CMF}]$ was diminished. Note that this form of spectra is the same as appearing in a spherical model occurs only if σ_s reaches 0.04 S.m^{-1} in *S. cervisiata* and 0.06 S.m^{-1} in *Tetraselmis*.

It was found that the v_{cDEP}^p spectra of both cells were not dependent on the two cell densities used for the present study. This implies that any cell-to-cell interaction among neighbor cells in the suspension was very small. To verify this, a calculation was made of the total work (U) to bring two polarized cells to a center-to-center separation. The calculation for the total work was carried out as a function of a radial distance r . As seen from Fig. 5.15, for values of $r/R \geq 6$, the work U becomes negligibly small. This means that two spheroids which are separated about six times the cell radius (R) interact negligibly with each other. As observed from experiments through the microscope, a value of the ratio of $r/R = 6$ is relevant to cell densities which are less than $9.2 \times 10^6 \text{ cells/m}\lambda$. Thus in the all the present experiments the average value for $r/R \geq 6$.

References

1. Mahaworasilpa T. L., Coster H. G. L. and George E. P. 1994. Force on biological cells due to Applied (AC) electric fields. I. Dielectrophoresis. *Biochim Biophys Acta* **1193**: 118-126.
2. Pethig R. and Markx M. H. 1997. Applications of dielectrophoresis in biotechnology. *Trends and Biotechnol* **15**: 426-432.
3. Raicu V., Raicu G. and Turcu G. 1996. Dielectric properties of yeast cells as simulated by the two-shell model. *Biochim. Biophys. Acta*, 1274:143-148.
4. Wanichapichart P., Boontawin, S., Kaewpiboon, A., and Kanchanapoom, K. 2002. Determination of dielectric properties of single cells by dielectrophoretic method. *Science Asia* 28(2): 113-119.
5. Wanichapichart P., Wongluksanapan, T., and Khooburat, L. 2007. Electrorotation: Diagnostic tool for abnormality of marine phytoplankton cells. The 2nd IEEE International Conference on Nano/Micro Engineering and Molecular Systems. 1115-1120.
6. Zhou X. F., Markx G.H., and Pethig R. 1996. Effect of biocide concentration on electrorotation spectra of yeasts cells, *Biochim. Biophys. Acta.*, 1218: 60-64.

CHAPTER 6

CELL DIELECTRIC PROPERTIES USING THE IMPEDANCE, RC-MODEL, APPROACH

6.1 Introduction

In the previous chapter it was shown that determinations of cell dielectric properties could be made from measurement of the dielectrophoretic velocity (v_{cDEP}^p) by curve fitting to a theoretical model. However, zero value of v_{cDEP}^p at higher frequencies was not found. This led to the absence of the negative v_{cDEP}^p in chapter 5. This brought about the ambiguity of the dielectric value of the cytoplasm obtained by v_{cDEP}^p curve-fitting.

As seen in chapter 2, two critical frequencies (f_λ, f_h) could be identified by both Laplace and RC approaches. The Laplace approach, however, involves very complicated mathematical functions (see section 2.2.5, chapter 2). In contrast, based on the impedance approach, the values $\text{Re}[\text{CMF}]$ could be written in a compact form in terms of the effective complex impedance (Z_{eff}^*) (Eq. 2.67), in which the $\text{Re}[\text{CMF}]$ was easily solved for two critical frequencies where $\text{Re}[\text{CMF}]=0$ (Eqs. 2.79 and 2.80).

This chapter deals with the impedance approach to determine cell dielectric properties using the knowledge of f_λ alone. Experiments were carried out under changes in σ_s . *Tetraselmis* and *S. cervisiata* were so used as models. This is also to verify Eq. (2.29) after adequate experimental data is obvious. The relationships between $f_\lambda, f_h, v_{cDEP}^p$ and F_{cDEP}^p will be discussed in chapter 7.

6.2 Cell Preparation and Density

Observations of the critical frequencies of *S. cervisiata* and *Tetraselmis* were the same as described before in chapter 4. Data of f_λ and σ_s from chapter 5 was re-plotted in this chapter. Since the plotting is essential for the determination of all parameters, the σ_s was finely adjusted. As reported previously, the lowest σ_s value of 0.5 M sorbitol solution was about $0.010 \pm 0.003 \text{ S.m}^{-1}$, and the higher values used in this chapter was $0.35 \pm 0.01 \text{ S.m}^{-1}$.

6.3 Critical Frequencies

6.3.1 *S. cervisiata*

6.3.1.1 Effect of electric field strengths and cell densities

Only the lower critical frequency f_λ was obtained and shown in Figure 6.1 against σ_s . Changes in electric field strengths (E) from 28 kV.m^{-1} , 57 kV.m^{-1} and 143 kV.m^{-1} (Fig. 6.1a, b and c), did not affect the f_λ . As reported in section 5.3.1.1 to 5.3.1.2, the f_λ on both cell density is independent on the σ_s and E used, but it increases with σ_s . Again, Fig. 6.2 shows that f_λ is independent of E .

6.3.2 *Tetraselmis* sp.

6.3.2.1 Effect of electric field strengths and cell densities

Plot of f_λ against σ_s for both cell densities are shown in Figure 6.3. Again, only f_λ was observed. Changes in E from 28 kV.m⁻¹ to 143 kV.m⁻¹ (Figs. 6.3a to b) did not affect the f_λ . Again, Fig. 6.4 shows that f_λ is independent of E .

6.4 Data Fittings

The method of curve fitting was made based on the basis of the procedure as described before (see Eq. 5.1 in section 5.4). Figures 6.5 and 6.6 show that the curves seem to fit well with the experimental data. The error as computed from Eq. 5.1, using 3 replicates and the value of 7.34 ± 0.28 % was obtained. Deviation from each curve-fitting (Figs. 6.1 to 6.4) was then calculated to sum up the average error. Numerical calculations of standard deviation were given in details elsewhere (Hoffman, 1993).

6.5 Discussions and Conclusions

This chapter described how the relative permittivity and the conductivity of the membrane and the cytoplasm of *S. cervisiata* and *Tetraselmis* were obtained by using f_λ curve-fitting and the impedance approach. It was found that f_h of both cells could not be detected in the experiments; this was also the case for the work reported by other researchers (Gimsa and Wachner, 1998 and 1999). One possibility explaining this is that the induced dipole cannot follow the rapid changes in the electric field, or other dissipative effects limit the magnitude of the induced dipole moment. Although the lack of data on the higher critical frequency effects the estimations of dielectric properties of the cytoplasm (see Fig. 2.12a), the latter could be

estimated from dielectrophoretic velocity spectra. The estimation of dielectric parameters from the critical frequency provides a simpler technique to use.

By increasing the solution conductivity (σ_s), f_λ increases and when σ_s reaches a critical value (σ_{ct}) where $f_\lambda = f_h$, the cell experiences a zero force. Hence, there is no F_{cDEP} on the cell. To find this σ_{ct} , one can simply increase the σ_s until no dielectrophoresis can be observed. In this work, the “banana” shape as called by Gimsa and Wachner (1999) can be plotted from Eq. 2.79, and the σ_{ct} can be theoretically obtained as 0.24 and 0.37 for *S. cervisiata* and *Tetraselmis*, respectively.

Dielectric values in Table 6.1 agree well with the range reported by the literatures (Radu *et al.*, 1996; Zhou *et al.*, 1996; Raicu *et al.*, 1996; Wanichapichart *et al.*, 2007). As mentioned in chapter 1 (section 1.3) and 5 (section 5.5), determinations of the parameters could be made through an electrorotation technique (Raicu *et al.*, 1996; Zhou *et al.* 1996). By this method, only a , b and σ_s (see Fig. 2.1) were measured directly. The comparison between the dielectric properties obtained from the present work and that in the literatures are shown in Table 6.1.

It should be noted that the rather high value for ε_m and δ of *S. cervisiata* in Table 6.1 implies a special attribute of TISTR 5088 yeast cells directly or it indicates that the double-shelled spheroid should be used to derive the dielectric parameters (Zhou *et al.*, 1996).

References

1. Asami K., Hanai T. and Koizumi N. 1980. Dielectric approach to suspensions of ellipsoidal particles covered with a shell in particular reference to biological cells, *Japanese Journal of Applied Physics*, vol. 19(No.2): 359-365.
2. Gimsa J. and Wachner D. 1998. A unified resistor-capacitor model for impedance, dielectrophoresis, electrorotation and induced transmembrane potential. *Biophysical J* **75**: 1107-1116.

3. Gimsa J. and Wachner D. 1999. A polarization model overcoming the geometric restrictions of the Laplace solution for spheroidal cells: Obtaining new equations for field-induced forces and transmembrane potential. *Biophysical J* **77**: 1316-1326.
4. Hoffman, J. D., 1993. Numerical methods for engineers and scientists, McGraw-HILL, Singapore.
5. Jones T. B., 1995. *Electromechanics of Particles*. Cambridge University Press, Cambridge.
6. Pethig R. and Markx M. H. 1997. Applications of dielectrophoresis in biotechnology. *Trends and Biotechnol* **15**: 426-432.
7. Pohl H. A., 1978. Dielectrophoresis: The Behaviour of Neutral Matter in Non-Uniform Electric Fields. Cambridge University Press, Cambridge.
8. Radu M., Petcu I., Sommer A. and Avram D. 1996. Change in membrane electrical parameters of yeast following chemical treatment for protoplast isolation. *J Bioelectrochem Bioenerg* **40**: 159-166.
9. Raicu V., Raicu G. and Turcu G. 1996. Dielectric properties of yeast cells as simulated by the two-shell model. *Biochim. Biophys. Acta*, 1274:143-148.
10. Zhou X. F., Markx G.H., and Pethig R. 1996. Effect of biocide concentration on electrorotation spectra of yeasts cells. *Biochim. Biophys. Acta.*, 1218: 60-64.

CHAPTER 7

CHARACTERIZATION OF DEAD AND ARSENIC PRETREATED CELLS

7.1 Introduction

Heated cells and arsenic contaminated cells were determined for dielectric properties before by Wanichapichart and her colleague (2007) using electrorotation technique. A cell was induced in a rotating electric field in a four-electrode system. They showed that the rotation of heated *Tetraselmis* cells diminished at the lower frequency range, while that of the arsenic pretreated cells was smaller than that of the control. Curve-fitting of rotation speeds were employed to estimate the dielectric properties of the cells. It was found that the specific membrane conductance was increased from $0.5 \text{ kS}\cdot\text{m}^{-1}$ for the control to $90 \text{ kS}\cdot\text{m}^{-1}$ for the heated cells. Cells pretreated with arsenic solution from 10 to 100 ppm levels increased in the membrane conductance to $8.8 \text{ kS}\cdot\text{m}^{-1}$; a much smaller effect compared to heated cells. In addition, for arsenic pretreated cells, it was found that the membrane and the cytoplasmic permittivity were reduced from $39\epsilon_0$ to about $13\epsilon_0$, at all levels of arsenic used in that study. The study also found that it was possible to distinguish the viable from the non-viable cells at certain selected conditions for electric field, frequency range and solution conductivity. The method of cell rotation in a rotating electric field requires measurements of the cell spin speed using one cell at a time.

In chapters 5 and 6 the dielectric properties of the living *S.cervisiata* and *Tetraselmis* were obtained from dielectrophoretic measurements by fitting the DEP data to twDEP theory and utilizing a spheroidal cell model. Each of the dielectric parameters was estimated from two techniques i.e. dielectrophoretic velocity (in chapter 5) and the critical frequencies (in chapter 6). For further verification of the model developed, experiments will be carried out with heated and arsenic pretreated

cells in this chapter. The present study will repeat the above experiments with the TPI electrode.

7.2 Cell Preparations

S.cervisiata and *Tetraselmis* were prepared as described in section 4.1 (chapter 4). The method of cell induction was the same as in section 4.3.

7.3 Dielectrophoretic velocity and Critical frequency

7.3.1 *S. cervisiata*

Figure 7.1 shows dielectrophoretic velocity (v_{cDEP}^p) of the control and heated *S. cervisiata* under two solution conductivities. It reveals that the control cells translate to electrode tips with a much higher speed than the heated cells. In Fig. 7.1a, for $\sigma_s = 0.01 \text{ S.m}^{-1}$ and $E=28 \text{ kV.m}^{-1}$, the maximum v_{cDEP}^p of the control and heated $1.15 \times 10^5 \text{ cells.ml}^{-1}$ cells were $1.20 \pm 0.81 \text{ }\mu\text{m.s}^{-1}$ at 200 kHz and $0.25 \pm 0.08 \text{ }\mu\text{m.s}^{-1}$ at 1 MHz, respectively. It is interesting to point out that this is the first time to observe the higher critical frequency (f_h) of v_{cDEP}^p measurement for heated cell at 8 MHz, while f_h of the control could not be observed. In contrast, at the lower frequency, f_λ of heated cell could not be found while that of the control cell was 50 kHz. Below 50 kHz (f_λ), the control cell exhibited negative v_{cDEP}^p started from zero to $-0.80 \pm 0.07 \text{ }\mu\text{m.s}^{-1}$. At 30 MHz limit, v_{cDEP}^p of the control was $0.6 \pm 0.05 \text{ }\mu\text{m.s}^{-1}$ where the negative value of heated cell could not be found.

In Fig. 7.1b, when σ_s was increased to 0.04 S.m^{-1} , v_{cDEP}^p of both control and heated cells were dramatically reduced with a much less speed than that of cells in Fig. 7.1a. The maximum v_{cDEP}^p of the control and heated cells were $0.23 \pm 0.02 \text{ }\mu\text{m.s}^{-1}$ at 8 MHz and $0.05 \pm 0.01 \text{ }\mu\text{m.s}^{-1}$ at 1 MHz, respectively. It is surprising that both f_λ and f_h of heated cell could be observed viz. at 0.5 MHz and 3 MHz, respectively. As seen from the figure, the frequency range between f_λ and f_h is narrow. For the control, f_λ was 2 MHz and f_h could not be observed beyond 30 MHz limit. At that limit, v_{cDEP}^p of the control was $0.06 \pm 0.01 \text{ }\mu\text{m.s}^{-1}$. It was found that dielectrophoresis could not be observed for heated cell when σ_s was higher than 0.04 S.m^{-1} .

Figure 7.2 shows f_λ of the control and heated $1.15 \times 10^5 \text{ cells.ml}^{-1}$ cells when $E=28 \text{ kV.m}^{-1}$. It reveals that the value of f_λ shifts to higher frequencies when σ_s was ranged from 0.01 to 0.30 S.m^{-1} . As seen in Fig. 7.2a, for the control, f_λ starts from 50 kHz at $\sigma_s = 0.01 \text{ S.m}^{-1}$ to 30 MHz at 0.25 S.m^{-1} . For heated cell, f_λ starts from 100 kHz at $\sigma_s = 0.03 \text{ S.m}^{-1}$ to 0.5 MHz at 0.04 S.m^{-1} .

7.3.2 Tetraselmis

Figure 7.3 shows v_{cDEP}^p spectra of the control and arsenic pretreated cells. When increasing arsenic concentrations from of 1 to 150 ppm as step shown in the figure, the maximum v_{cDEP}^p of the control and pretreated $1.15 \times 10^5 \text{ cells.ml}^{-1}$ cells were fixed at $9.4 \pm 0.3 \text{ }\mu\text{m.s}^{-1}$ while the peak shifts to lower frequencies. The value of f_λ decreased from 35 kHz to 15 kHz when the arsenic concentration was increased under σ_s used as 0.01 S.m^{-1} . As seen in Fig. 7.4, f_λ curves were shifted when σ_s was ranged between 0.10 to 0.35 S.m^{-1} . At the lower σ_s , increasing arsenic concentration

from 1 to 150 ppm, f_λ shifts from 40 kHz to 10 kHz, respectively. At the higher σ_s , f_λ shifts from 7 MHz to 2 MHz. It should be noted that f_h could not be observed in all cases.

Figure 7.5 shows v_{cDEP}^p of the control and heated cells under $0.01 \text{ S.m}^{-1} \sigma_s$. It reveals that the control cells translate to electrode tips with a higher speed than the heated cells. The maximum v_{cDEP}^p of the control and heated $1.15 \times 10^5 \text{ cells.ml}^{-1}$ cells were $9.0 \pm 0.4 \text{ }\mu\text{m.s}^{-1}$ at 200 kHz and $4.4 \pm 0.2 \text{ }\mu\text{m.s}^{-1}$ at 600 kHz, respectively. It is interesting that there are no f_λ and f_h of v_{cDEP}^p measurement for heated cell, while f_λ was found only for the control cell.

7.4 Data Fittings

The method to fit the theoretical curve to the experimental data in order to obtain dielectric parameters of the cells were made on the basis of the known sensitivities of the dielectrophoretic velocity and critical frequencies on the dielectric parameters (shown in Fig. 2.6 and and Fig. 2.12). The error as computed from Eq. 5.1, using 3-replicates and the value of $6.87 \pm 0.29 \%$ was obtained. Dielectric parameters obtained from both approaches for both cells were reported in Table 7.1.

7.5 Discussions and Conclusions

Dielectric parameters obtained were listed in Table 7.1 and compared with the literatures (Radu *et al.*, 1996; Raicu *et al.*, 1996 and 1998; Wanichapichart *et al.*, 2007) in Table 7.2. The parameters obtained for the present study were used to investigate the Clausius-Mossotti factor [CMF] spectra of the control and heated S.

cervisiatae. As shown in Fig. 7.6, both real part (Re[CMF]) and imaginary part (Im[CMF]) of the control is higher than that of heated cells. This infers the different conductivity of the cytoplasm (σ_c) between the control and heated cells. From Table 7.1, it is interesting that the value of σ_m of heated yeast cells was much higher than that of the control and this was responsible for the absence of f_λ . These results are in good agreement with those previously shown in Fig. 2.6f (chapter 2). For higher frequencies, the control yeast cells possess a higher σ_c than that of the heated cells.

Velocity spectra of arsenic pretreated cells (Fig. 7.3) showed the correlation between changes of arsenic concentrations used in the present study and the values of f_λ while the peak velocity is not affected. It appears that the shifting of the critical frequency to lower values might be cause of changes in the dielectric property of the membrane. It is possible that the membrane proteins are affected by arsenic. This result is in consistency with the f_λ vs. σ_s plots, using our RC model (Fig. 7.4). It should be noted that on increasing σ_s , the cell velocity was reduced and became negligible a 0.37 S.m^{-1} solution was used. This implies that the critical conductivity of *Tetraselmis* is 0.37 S.m^{-1} , which provides an indication of the conductivity of cytoplasm (σ_c). The previous work done by Wanichapichart *et al.* (2007) showed that arsenic pretreatment increased the membrane conductance similar to what found in dead cells, but cell proliferation ceased only when the arsenic reached 100 ppm level. Wanichapichart and her colleagues proposed therefore, that the arsenic pretreated cells were still alive, and the cessation of cell growth could be due to some metabolic inhibition.

As is seen, the C_m of arsenic pretreated cells is increased with increasing arsenic levels. Both G_m and C_m were estimated by assuming a thickness of the membrane with the cell wall of 35 nm (for Wanichapichart *et al.*, 2007) and 13 nm (for the present study). In a previous work (Wanichapichart *et al.*, 2002) theoretical estimations made by curve fitting using dielectrophoretic data revealed possible thicknesses of the wall including, the membrane, of plankton cells to be from 20 to 50 nm. The 13 nm used in this study refers to the thickness of the membrane only.

The specific capacitance (C_m) and conductance (G_m) of the membrane in all cases were calculated and compared with the literature is shown in Table 7.2. For the present study, the results showed that C_m and G_m of the control and heated *S. cerevisiae* were 11.06 mF.m⁻², 8.33 S.m⁻² and 18.44 mF.m⁻², 33.33×10³ S.m⁻², respectively. The values of C_m and G_m of the control *Tetraselmis* were 5.45 mF.m⁻² and 13.08 S.m⁻², respectively, which were smaller than that of the arsenic pretreated cells. For arsenic levels of 1, 5, 10, 50, and 150 ppm; the C_m values of the pretreated cells were 6.81, 8.17, 10.89, 14.30 and 21.79, respectively. It was interesting that while the C_m values of the arsenic pretreated cells were increased, the value of σ_m remained constant at 23.08 S.m⁻². Following exposure to arsenic, the velocity spectrum remained similar to that of the control, except that the membrane conductivity increased.

In general conclusion, the present study also shows comparison of dielectric properties obtained from the Laplace and impedance approaches as shown in Table.

References

- 1.Radu M., Petcu I., Sommer A. and Avram D. 1996. Change in membrane electrical parameters of yeast following chemical treatment for protoplast isolation. *J Bioelectrochem Bioenerg* **40**: 159-166.
- 2.Raicu V., Raicu G. and Turcu G. 1996. Dielectric properties of yeast cells as simulated by the two-shell model. *Biochim.Biophys.Acta*, 1274:143-148.
- 3.Raicu V., Gusbeth C. Anghel D. F. and Turcu G. 1998. Effect of cetyltrimethylammonium bromide (CTAB) surfactant upon the dielectric properties of yeast cells. *Biochim.Biophys.Acta*, 1379:7-15.

4. Wanichapichart P., Boontawin, S., Kaewpiboon, A., and Kanchanapoom, K. 2002. Determination of dielectric properties of single cells by dielectrophoretic method. *Science Asia* 28(2): 113-119.
5. Wanichapichart P., Wongluksanapan, T., and Khooburat, L. 2007. Electrorotation: Diagnostic tool for abnormality of marine phytoplankton cells. The 2nd IEEE International Conference on Nano/Micro Engineering and Molecular Systems. 1115-1120.
6. Zhou X. F., Markx G. H., and Pethig R. 1996. Effect of biocide concentration on electrorotation spectra of yeasts cells, *Biochim. Biophys. Acta.*, 1218: 60-64.

CHAPTER 8

PROOF OF IMAGINARY FUNCTIONS

8.1 Introduction

As seen in chapter 5, *S. cervisiata* and *Tetraselmis* exhibited dielectrophoresis in travelling electric field by moving towards the tips of two parallel arrays inter- digitated electrode (TPI electrode) with different dielectrophoretic velocity (v_{cDEP}^p). When the values of the conductivity of the suspending medium (σ_s) and electric field strengths (E) were changed, $\text{Re}[\text{CMF}]$ (Eq. 2.48) and the cell velocity (Eq. 3.9) were affected and hence F_{cDEP}^p was estimated. Nevertheless, the value of the imaginary function ($\text{Im}[\text{CMF}]$) of the model had not been verified yet since travelling wave dielectrophoretic velocity (v_{twDEP}^p) could not be observed. Even though the electrical phase sequences (ϕ) of the TPI electrode were alternated at $\pi/2$ phase shift (see details in section 4.3, chapter 4), the twDEP velocity was not observed. This chapter thus concentrates at the particular frequencies around f_λ to find out possibility of the v_{twDEP}^p .

According to Eq. 3.4, it is possible to move a cell along the central channel (see Fig. 3.1) with velocity v_{twDEP}^p (Eq. 3.10) resulting from twDEP forces (F_{twDEP}^p). The magnitude and direction of such velocity depends on changes in complex dielectric parameters which are frequency dependence and this reflects the imaginary function ($\text{Im}[\text{CMF}]$) (Eq. 2.49). Effort of finding v_{twDEP}^p through out experimentations was focused by changing the external parameters of the cell such as electric field strengths (E) and the conductivity of the suspending medium (σ_s), as appeared in Eq. 3.10. In addition, the phase difference between consecutive electrodes could also be varied but electrode circuit for this study must be modified.

8.2 Methods to Investigate v_{twDEP}

Cells were prepared as mentioned in chapter 4, section 4.1.1 and 4.1.2. Cell inductions in travelling electric field were performed by changes in electric field strength (E) and the medium conductivity (σ_s) as mentioned in section 4.3. The frequency of the applied signals was gradually decreased from the upper (30 MHz limit) to lower values, to examine two critical frequencies (f_λ and f_h). When cell exhibited the negative v_{cDEP} and f_λ was found, the frequency of the signals was then finely adjusted as a step of 0.01 Hz, especially the frequency that closes to the value of f_λ . Under such circumstance, the translation of cell being repelled from the electrode tip was monitored through a microscope until the cell moves along the central channel of the TPI electrode.

8.3 Results

Due to small thickness of the TPI electrode (0.2 μm) compared to the cell size (4-10 μm), cell disappearance from focal plane of the microscope along the electric field lines and then escape from the field was possible. The electric force F_{twDEP} could be significant only in a small volume of field propagation. The same result was found even if E was increased to 143 $\text{kV}\cdot\text{m}^{-1}$ (the maximum limit) and σ_s was reduced to 0.01 $\text{S}\cdot\text{m}^{-1}$ (the minimum limit of the medium conductivity).

It should be noted that cell moving away from the TPI electrode was in the resultant direction between F_{cDEP} and F_{twDEP} , as shown in Fig. 8.1, where of solution covering the TPI electrode was about 100 $\mu\lambda$ (section 4.1), hence the cell escaped from the propagating field to the remaining volume ($\approx 100 \mu\lambda$). This explained why the v_{twDEP} could not be measured in this study. However, the following

section shows how σ_s and other dielectric parameters affect the disappearance of v_{twDEP}^p in this work.

8.4 Changes in Dielectric Parameters and σ_s

According to mathematical expression of travelling wave dielectrophoretic velocity v_{twDEP}^p in Eq. (3.10), the direction and magnitude of the velocity depended on only $\text{Im}[\text{CMF}]$. The value of $\text{Im}[\text{CMF}]$ can either be positive and negative resulting in positive and negative v_{twDEP}^p , respectively, since other parameters appearing in Eq. (3.10) are all positive constant. From theoretical analysis in chapter 2, it was found that the expression of $\text{Im}[\text{CMF}]$ was termed as a function of the conductive (σ) and capacitive (ε) properties of the membrane (σ_m, ε_m), the cytoplasm (σ_c, ε_c) and the suspending solution (σ_s, ε_s), as in Eq. (2.49). Plots of the Eq. (2.49) as a function of electric field frequency were shown in Fig. 2.7. As is seen, the $\text{Im}[\text{CMF}]$ is sensitive to change in these parameters. It is interesting that the magnitude of the positive peak is affected by the values of $a, \delta, \sigma_c, \varepsilon_m, \sigma_m$, and σ_s as shown in Figs. 2.7a, 2.7b, 2.7d, 2.7e, 2.7f, and 2.7h, respectively. For the negative peak at the higher frequency, its magnitude is affected by the values of ε_c, σ_c and ε_s as shown in Figs. 2.7c, 2.7d, 2.7g, respectively. The $\text{Im}[\text{CMF}]$ magnitude affected directly to F_{twDEP}^p and hence to v_{twDEP}^p . It should be noted that changes in σ_c from 0.1 to 1.0, the crossover points of the spectra were shifted from lower to higher frequencies and vice versa for ε_m . In practical, only σ_s was known from experiments since the conductivity of the suspending medium could be adjusted by using 0.1 M KC λ solution (see chapter 4 for more details).

With a focus on changes in σ_s , Figs. 8.2 and 8.3 show that the magnitude of v_{twDEP}^p of *S. cerevisiae* and *Tetraselmis* should be observed when σ_s were ranged from 0.01 to 0.25 S.m⁻¹, and 0.01 to 0.37 S.m⁻¹, respectively. This is true only if the phase difference $\nabla\phi_i \neq 0$, $\text{Im}[\text{CMF}] \neq 0$ and $\text{Re}[\text{CMF}] = 0$. Figure 8.4

shows $\text{Re}[\text{CMF}]$ and $\text{Im}[\text{CMF}]$ spectra of the control and heated yeast cells. The regions of $\pm \overset{p}{F}_{cDEP}$ and $\pm \overset{p}{F}_{twDEP}$ are shown in the figure. Therefore, $\overset{p}{F}_{twDEP}$ of heated yeast cells should exhibit near 60 kHz while at the higher region it should be at 95 MHz. This explains why the f_h was not found in this work. In Figs. 8.5a and b, the $\overset{p}{F}_{twDEP}$ of *Tetraselmis* should be found at the lower frequency region of 20 to 48 kHz. In both cases (Figs. 8.4 and 8.5), although $-\overset{p}{F}_{cDEP}$ is larger than $+\overset{p}{F}_{twDEP}$ but incompatible electrode geometry did not allow the repellent cell to be in the corresponding plane of the $\overset{p}{F}_{twDEP}$, as shown in Fig. 8.1b.

8.5 Discussion and Conclusions

This chapter deal with experiments emphasizing on the $\overset{p}{v}_{twDEP}$. Since it was overshadowed with the greater $-\overset{p}{F}_{cDEP}$, the finding of $\overset{p}{v}_{twDEP}$ was then employed using theoretical data based on changes in σ_s . The twDEP could not be observed through out the present study even through the experiments were carefully performed under predicted frequencies. Considering the forces $-\overset{p}{F}_{cDEP}$ and $+\overset{p}{F}_{twDEP}$, it is concluded that electrode geometry; such as thickness and spacing between the central channels, are not suitable to perform the $\overset{p}{v}_{twDEP}$.

References

1. Hughes M. P. 2000. AC electrokinetic: applications for nanotechnology, *Nanotechnology*, 11: 124-132.
2. Mahaworasilpa T., Coster H. G. L., and George E. P. 1996. Force on biological cells due to applied (AC) electric fields. II. Electro-rotation. *Biochim. Biophys Acta*, **1281**: 5-14.

3. Radu M., Petcu I., Sommer A., and Avram D. 1996, Change in membrane electrical parameters of yeast following chemical treatment for protoplast isolation. *J. Bioelectrochem Bioenerg* **40**: 159-166.
4. Wang X. B., Hughes M. P., Huang Y., Becker F. F. and Gascoyne P. R. C. 1995. Non-uniform spatial distributions of both the magnitude and phase of AC electric fields determine dielectrophoretic forces. *Biochimica et Biophysica Acta*, 1243: 185-194,
5. Wanichapichart P., Wongluksanapan, T., and Khooburat, L. 2007. Electrorotation: Diagnostic tool for abnormality of marine phytoplankton cells. The 2nd IEEE International Conference on Nano/Micro Engineering and Molecular Systems. 1115-1120.
6. Zhou X. F., Markx G.H., and Pethig R. 1996. Effect of biocide concentration on electrorotation spectra of yeasts cells, *Biochim. Biophys. Acta.*, 1218: 60-64.

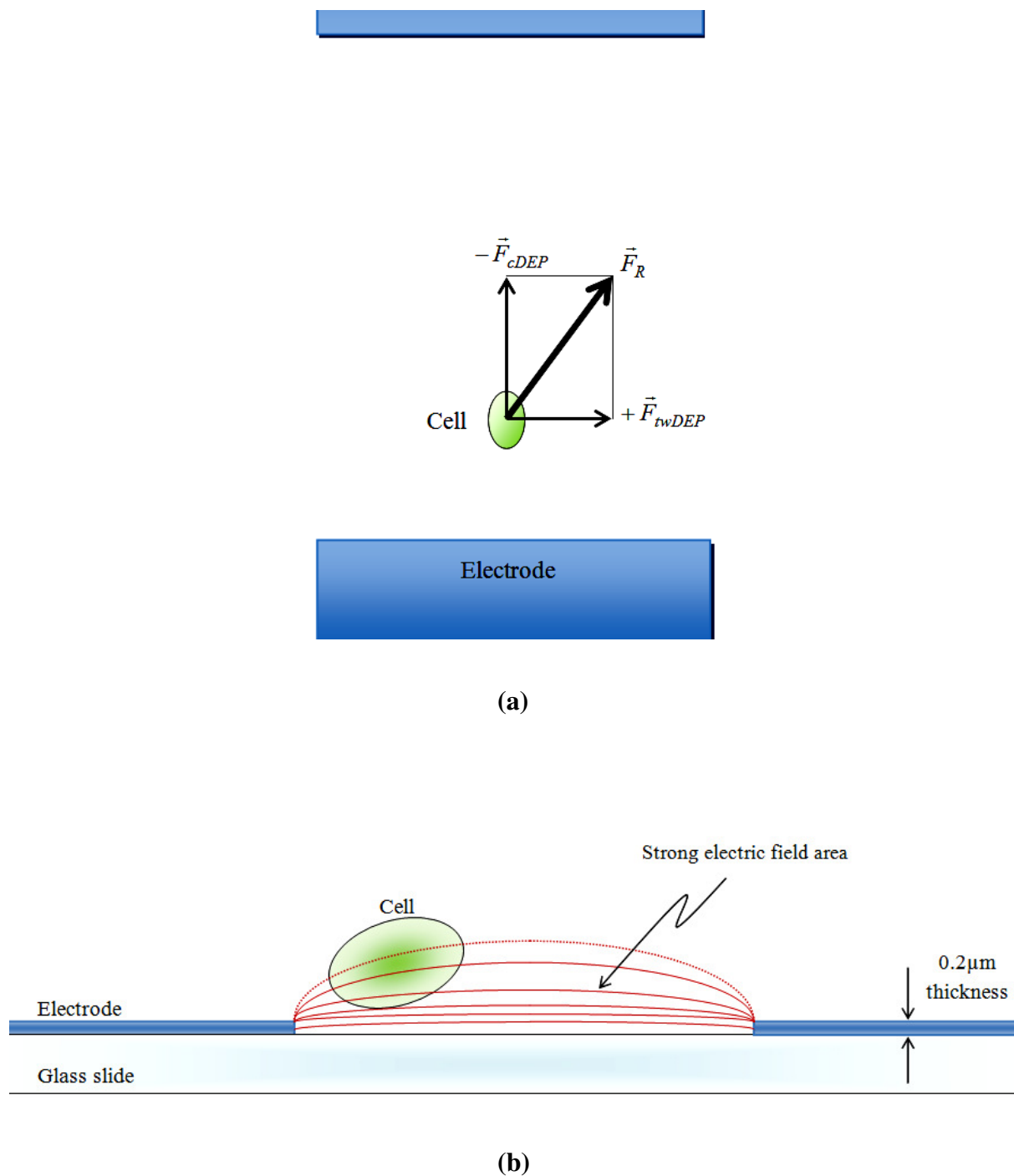


Fig. 8.1 Top view of the cell being repelled from the electrode tip showed the resultant force \vec{F}_R (a) acting on the cell where the strong propagating field area was shown in side view (b).

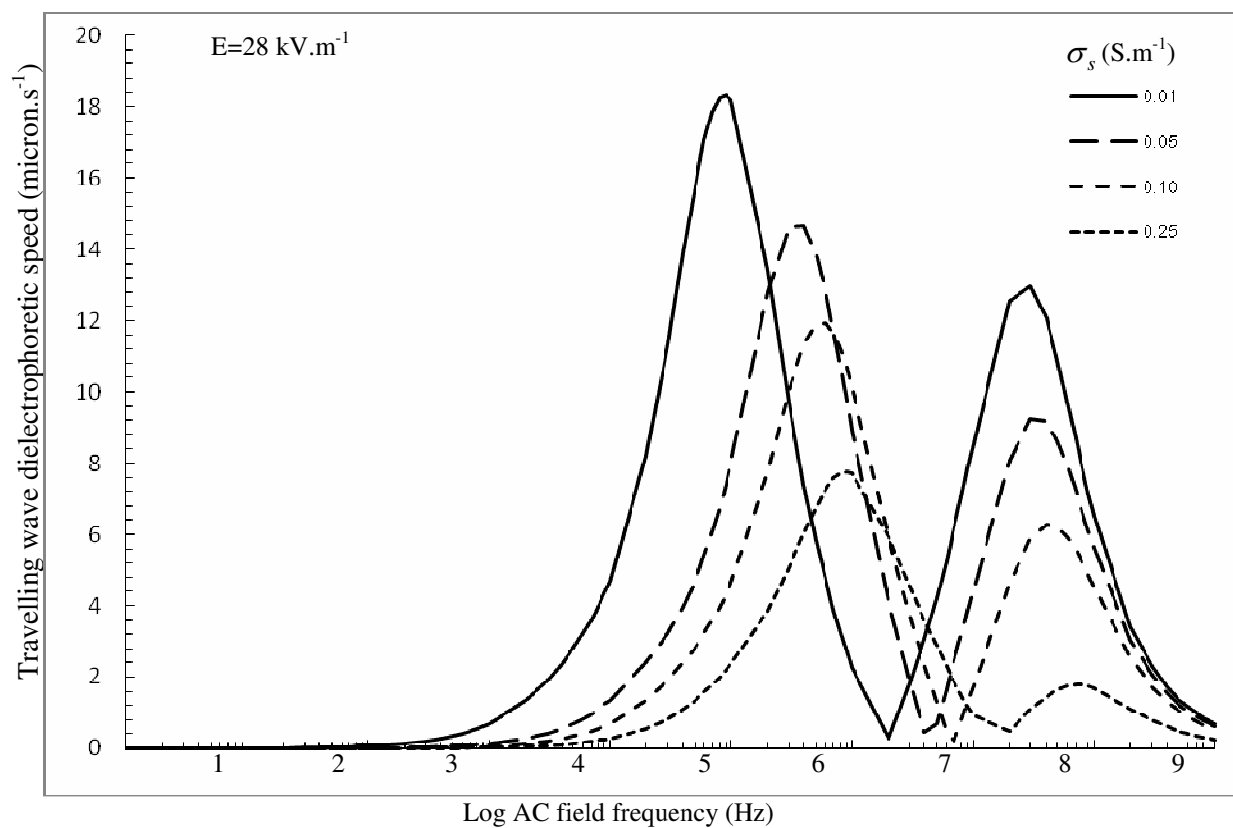


Fig. 8.2 Plot of magnitude of travelling wave dielectrophoretic velocity (v_{wDEP}) of the controlled yeast cells by using the dielectric parameters shown in Table 6.1.

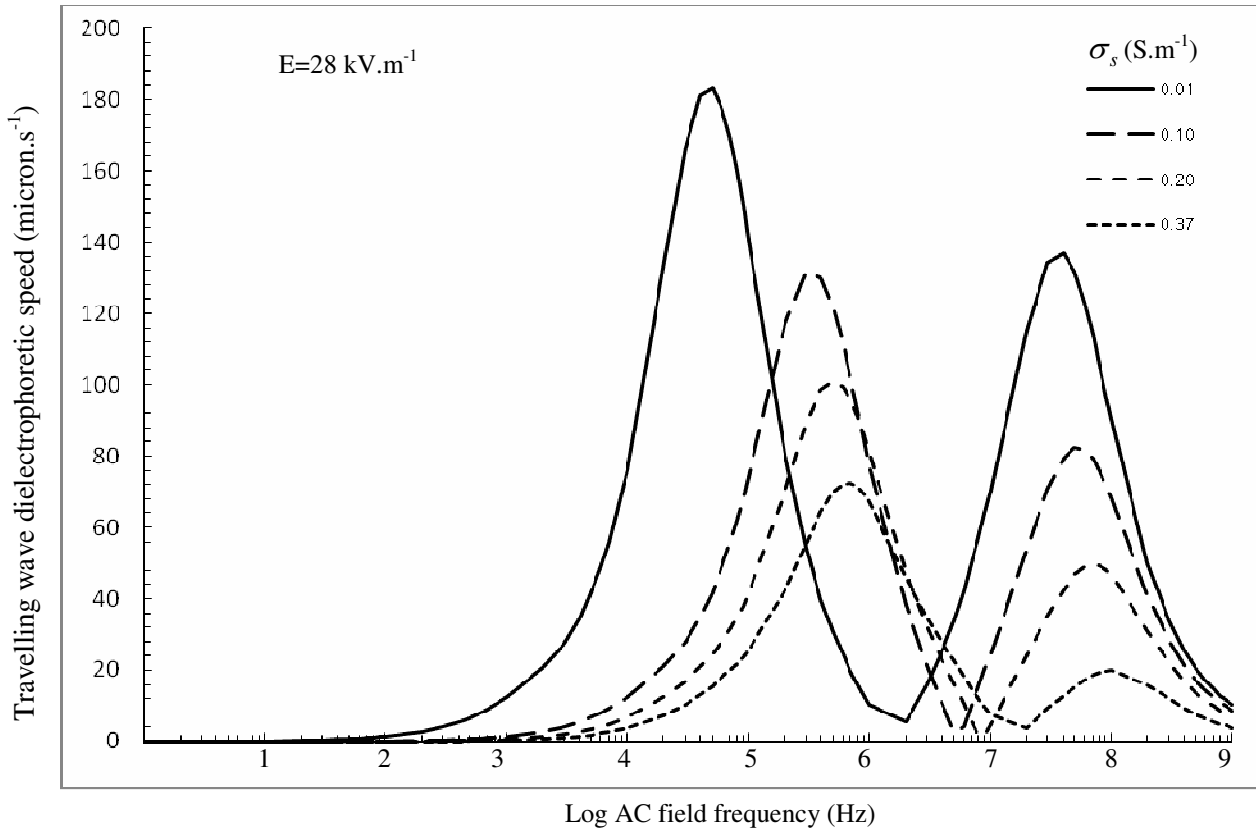


Fig. 8.3 Plot of magnitude of travelling wave dielectrophoretic velocity (v_{wDEP}^p) of the controlled *Tetraselmis* by using the dielectric parameters shown in Table 6.1.

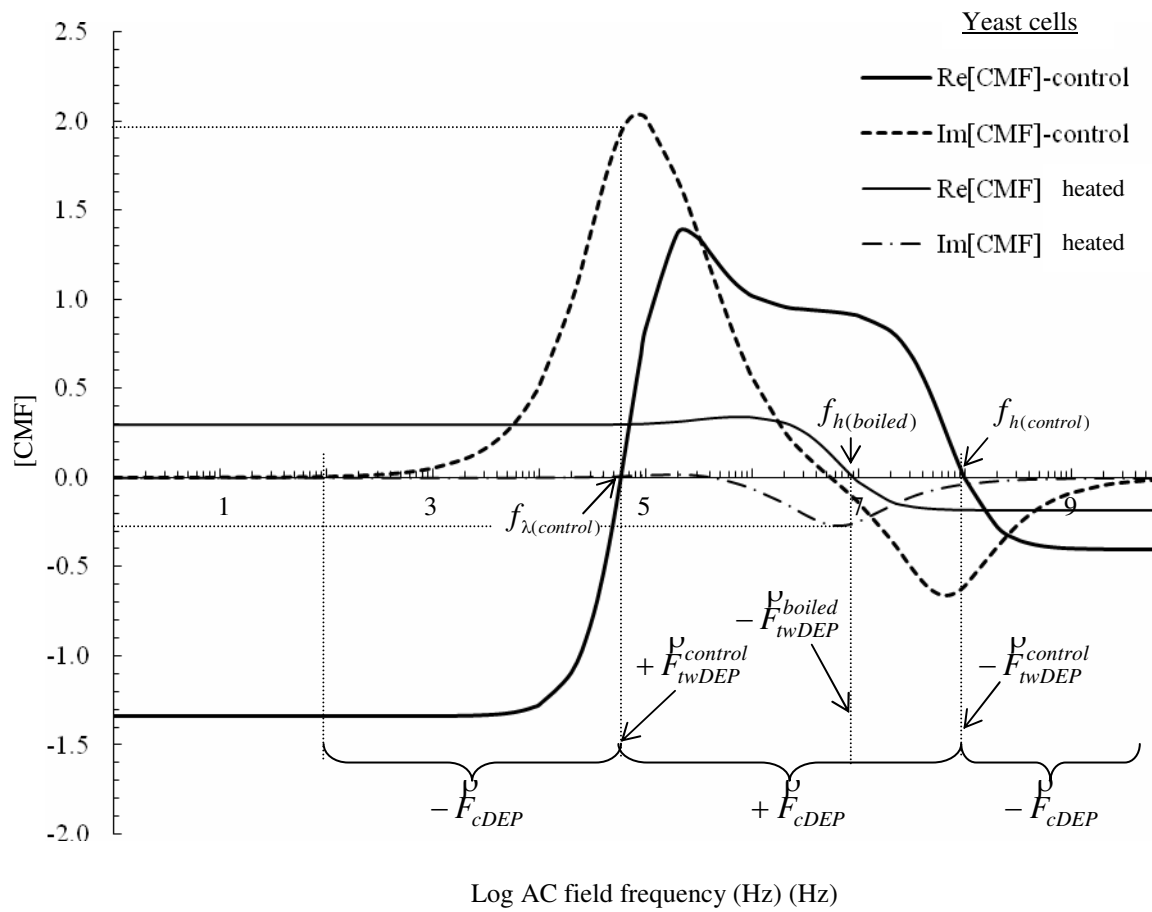
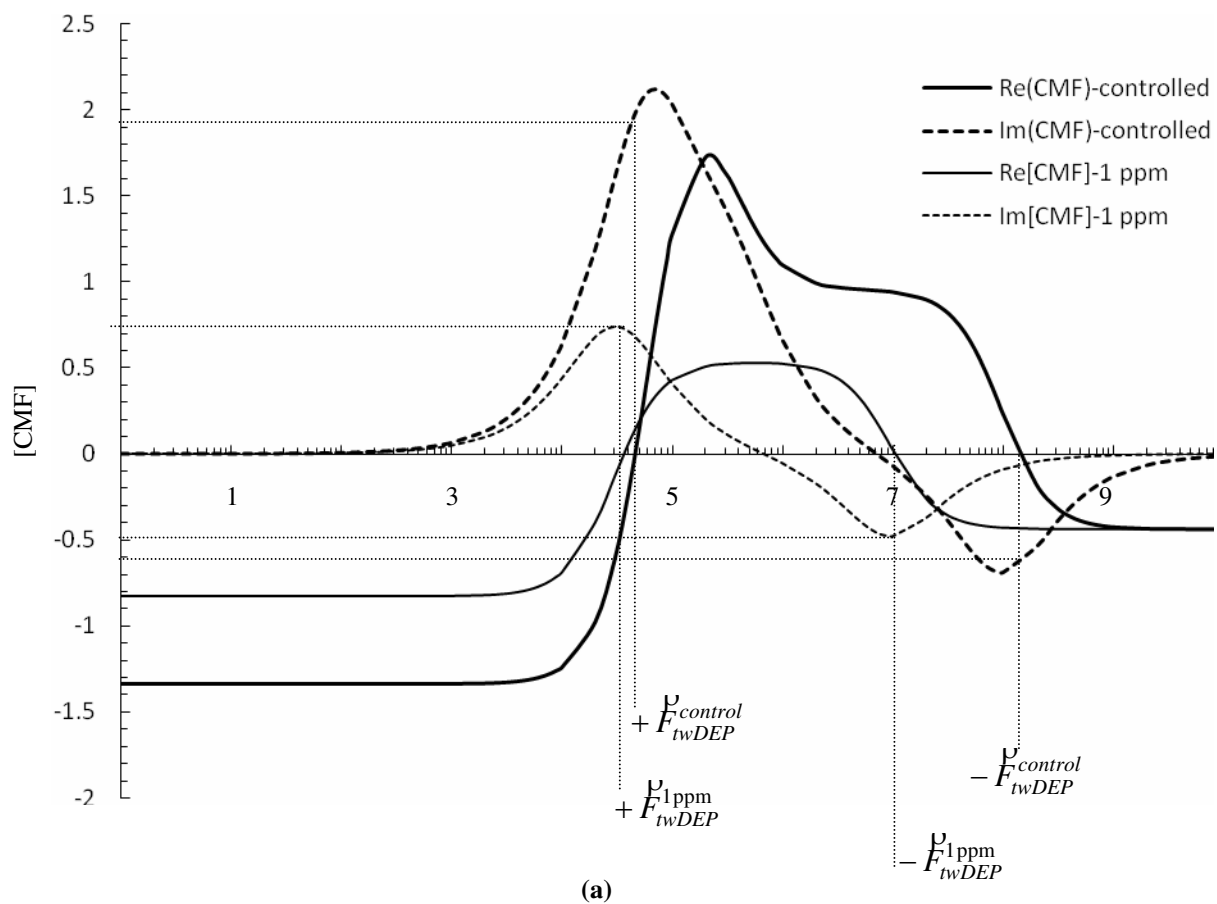
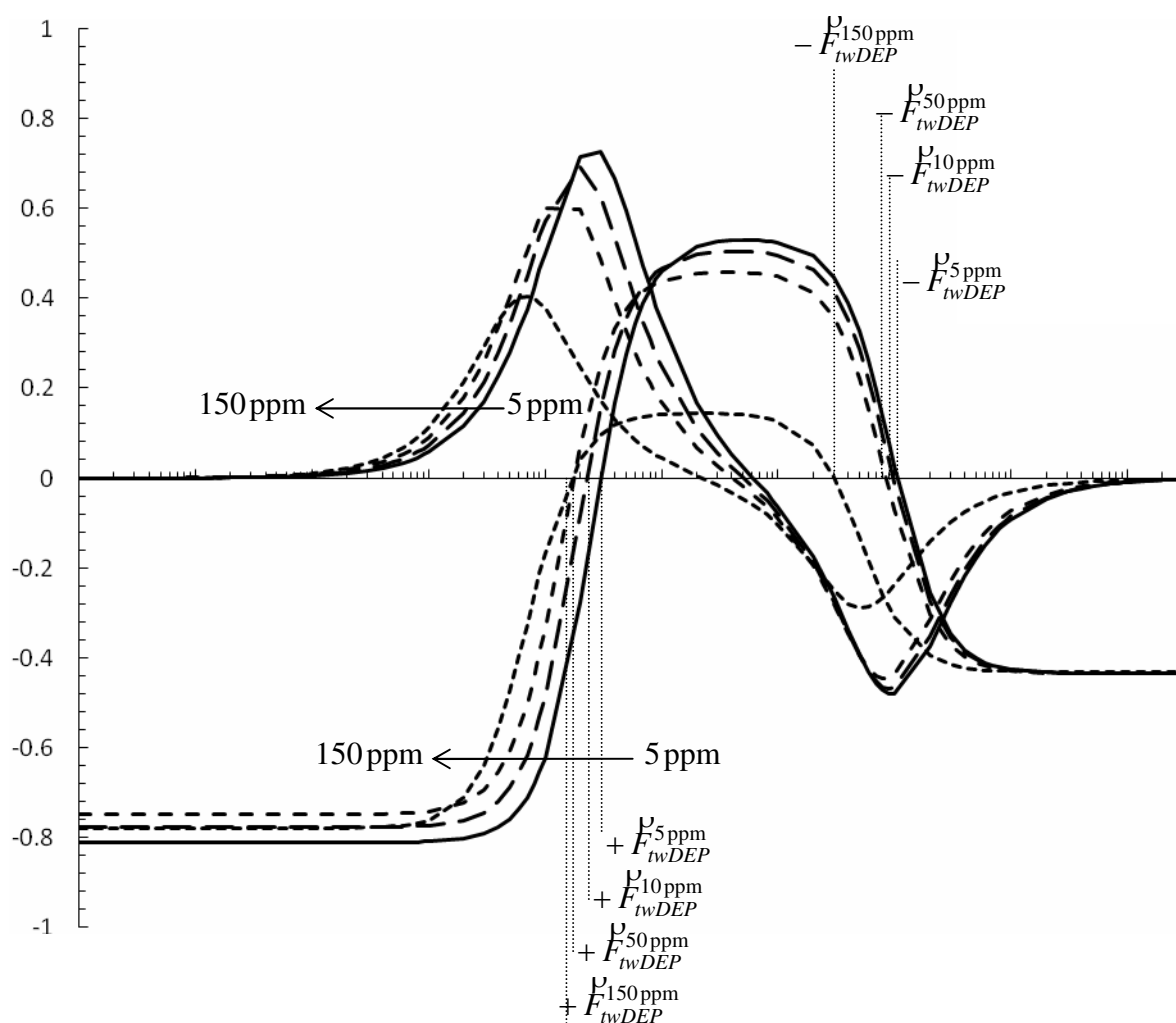


Fig. 8.4 Plots of Re[CMF] and Im[CMF] of the controlled and the boiled yeast cells by using the dielectric parameters as shown in Table 7.1. Three frequency ranges were indicated at the lower, intermediate and the higher frequency which relate with $\pm \hat{F}_{cDEP}$ and $\pm \hat{F}_{twDEP}$ at the lower and the higher, respectively.





(b)

Fig. 8.5 Comparisons of $\text{Re}[\text{CMF}]$ and $\text{Im}[\text{CMF}]$ of (a) the controlled and the 1 ppm arsenic pretreated *Tetraselmis* sp. cells and several of (b) 5, 10, 50, 150 ppm arsenic concentrations. All curves were plotted by using the dielectric parameters as shown in Table 7.1. Cross-over points of each curve indicated twDEP frequency which relate with $\pm \hat{F}_{twDEP}$ at the lower and the higher frequencies.

CHAPTER 9

SUGGESTIONS FOR FUTURE WORK

This study has shown theoretical approaches i.e. the Laplace and impedance (RC model) approaches and has proved only the first half of the Eq. 3.4. The experiments could not reveal all movements in the central electrode channel. To explain why both cells (*S. cervisiata* TISTR 5088 and *Tetraselmis* sp.) could not exhibit travelling wave dielectrophoresis (twDEP) and none of twDEP velocity (v_{twDEP}^p) data was obtained; theoretical analysis was taken into account. Drawback of the TPI electrode was mentioned here again to look overview of what should be extended from the one used for the present study.

As seen from chapter 8, travelling wave dielectrophoresis could be employed to distinguish cells with different dielectric properties which benefits cells separation work. It is possible to apply this technique with cell infection, being a carrier of foreign biological materials, for a diagnostic tool. To achieve that, a microchannel electrode with microfluidic feed should be developed. This stage should be done after the TPI electrode can be strengthened. The process of fabrication of microelectrode should be improved to be long-lasting uses. Material to be use for the electrode's base may be plastic to enhance the adhesion between electrode bar and the substrate. Also, the electrode spacing and the thickness should be minimized to be fit with the cell size (4-10 μm). Optimization of the electrode sizes should be examined for further study, at least to verify the assumptions proposed in section 8.5 (chapter 8).

To verify the model with other cells, the time-averaged force acting on a spheroid (Eq. 3.4) can be adapted for a sphere of which a , b , and c are equal and the L_k is $\frac{1}{3}$ instead. It should be noted that twDEP force on a spheroid can be calculated so that the optimization of microfluidic rate-flow in a microchannel TPI electrode can be estimated. Calculations of the complicated functions such as $\text{Re}[\text{CMF}]$, $\text{Im}[\text{CMF}]$ and twDEP forces should be computer-based approach in sequence. It is interesting that combinations of both cell velocity measurements and the lower critical frequency value can be integrated with other related techniques such as cell electro-orientation ,

as suggested by Jones (1995) and Lippert and Gimsa (2002), to improve accuracy of data obtained. Particular interest should be aimed at spheroidal cells since in reality it is not possible to choose identical cells to prove the approaches.

References

1. Jones, T. B. 1995. *Electromechanics of Particles*. Cambridge University Press, Cambridge, pp 2.
2. Lippert S. and Gimsa J. 2002. High resolution measurements of dielectric cell properties by a combination of AC-electrokinetic effects. In: *2nd International Workshop on Biological effects of EMFs at Rhodes Greece*. 7-11 October 2000, pp. 830-836.